



MINISTÉRIO DA
CIÊNCIA, TECNOLOGIA
E INOVAÇÕES



sid.inpe.br/mtc-m21c/2020/01.19.21.29-TDI

STABILITY CHARACTERISTICS OF COMPRESSIBLE BINARY PLANAR JETS

Maycol Marcondes Vargas

Doctorate Thesis of the Graduate Course in Engineering and Space Technology/Combustion and Propulsion, guided by Dr. Márcio Teixeira de Mendonça, approved in December 03, 2019.

URL of the original document:

<<http://urlib.net/8JMKD3MGP3W34R/3UQ4H4E>>

INPE
São José dos Campos
2019

PUBLISHED BY:

Instituto Nacional de Pesquisas Espaciais - INPE
Gabinete do Diretor (GBDIR)
Serviço de Informação e Documentação (SESID)
CEP 12.227-010
São José dos Campos - SP - Brasil
Tel.:(012) 3208-6923/7348
E-mail: pubtc@inpe.br

**BOARD OF PUBLISHING AND PRESERVATION OF INPE
INTELLECTUAL PRODUCTION - CEPPII (PORTARIA Nº
176/2018/SEI-INPE):****Chairperson:**

Dra. Marley Cavalcante de Lima Moscati - Centro de Previsão de Tempo e Estudos
Climáticos (CGCPT)

Members:

Dra. Carina Barros Mello - Coordenação de Laboratórios Associados (COCTE)
Dr. Alisson Dal Lago - Coordenação-Geral de Ciências Espaciais e Atmosféricas
(CGCEA)
Dr. Evandro Albiach Branco - Centro de Ciência do Sistema Terrestre (COCST)
Dr. Evandro Marconi Rocco - Coordenação-Geral de Engenharia e Tecnologia
Espacial (CGETE)
Dr. Hermann Johann Heinrich Kux - Coordenação-Geral de Observação da Terra
(CGOBT)
Dra. Ieda Del Arco Sanches - Conselho de Pós-Graduação - (CPG)
Sílvia Castro Marcelino - Serviço de Informação e Documentação (SESID)

DIGITAL LIBRARY:

Dr. Gerald Jean Francis Banon
Clayton Martins Pereira - Serviço de Informação e Documentação (SESID)

DOCUMENT REVIEW:

Simone Angélica Del Ducca Barbedo - Serviço de Informação e Documentação
(SESID)
André Luis Dias Fernandes - Serviço de Informação e Documentação (SESID)

ELECTRONIC EDITING:

Ivone Martins - Serviço de Informação e Documentação (SESID)
Cauê Silva Fróes - Serviço de Informação e Documentação (SESID)



MINISTÉRIO DA
CIÊNCIA, TECNOLOGIA
E INOVAÇÕES



sid.inpe.br/mtc-m21c/2020/01.19.21.29-TDI

STABILITY CHARACTERISTICS OF COMPRESSIBLE BINARY PLANAR JETS

Maycol Marcondes Vargas

Doctorate Thesis of the Graduate Course in Engineering and Space Technology/Combustion and Propulsion, guided by Dr. Márcio Teixeira de Mendonça, approved in December 03, 2019.

URL of the original document:

<<http://urlib.net/8JMKD3MGP3W34R/3UQ4H4E>>

INPE
São José dos Campos
2019

Cataloging in Publication Data

Vargas, Maycol Marcondes.

V426s Stability characteristics of compressible binary planar jets / Maycol Marcondes Vargas. – São José dos Campos : INPE, 2019.

xxii + 106 p. ; (sid.inpe.br/mtc-m21c/2020/01.19.21.29-TDI)

Thesis (Doctorate in Engineering and Space Technology/Combustion and Propulsion) – Instituto Nacional de Pesquisas Espaciais, São José dos Campos, 2019.

Guiding : Dr. Márcio Teixeira de Mendonça.

1. LST. 2. PSE. 3. Hidrodinamic stability. 4. Instability. 5. Jet.
I.Title.

CDU 532.51:531.36



Esta obra foi licenciada sob uma Licença [Creative Commons Atribuição-NãoComercial 3.0 Não Adaptada](https://creativecommons.org/licenses/by-nc/3.0/).

This work is licensed under a [Creative Commons Attribution-NonCommercial 3.0 Unported License](https://creativecommons.org/licenses/by-nc/3.0/).

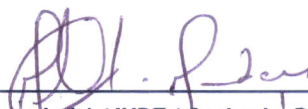
Aluno (a): **Maycol Marcondes Vargas**

Título: "STABILITY CHARACTERISTICS OF COMPRESSIBLE BINARY PLANAR JETS"

Aprovado (a) pela Banca Examinadora
em cumprimento ao requisito exigido para
obtenção do Título de **Doutor(a)** em

**Engenharia e Tecnologia
Espaciais/Combustão e Propulsão**

Dr. Márcio Teixeira de Mendonça



Presidente / Orientador(a) / INPE / Cachoeira Paulista - SP

() *Participação por Vídeo - Conferência*

Aprovado () *Reprovado*

Dr. Fernando de Souza Costa



Membro da Banca / INPE / Cachoeira Paulista - SP

() *Participação por Vídeo - Conferência*

Aprovado () *Reprovado*

Dr. Wladimir Mattos da Costa Dourado

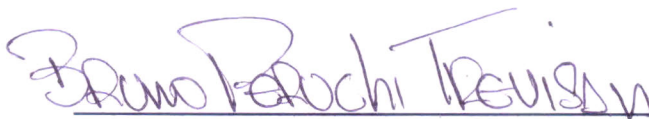


Membro da Banca / IAE/DGTA / São José dos Campos - SP

() *Participação por Vídeo - Conferência*

Aprovado () *Reprovado*

Dr. Bruno Peruchi Trevisan



Convidado(a) / IAE / São José dos Campos - SP

() *Participação por Vídeo - Conferência*

Aprovado () *Reprovado*

Este trabalho foi aprovado por:

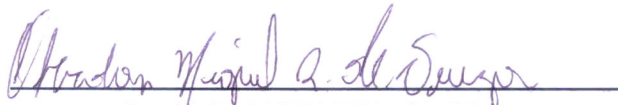
() *maioria simples*

unanimidade

Aprovado (a) pela Banca Examinadora
em cumprimento ao requisito exigido para
obtenção do Título de *Doutor(a)* em

**Engenharia e Tecnologia
Espaciais/Combustão e Propulsão**

Dr. Oberdan Miguel Rodrigues de Souza



Convidado(a) / IFRJ / Nilópolis - RJ

() *Participação por Video - Conferência*

Aprovado () *Reprovado*

Este trabalho foi aprovado por:

() *maioria simples*

unanimidade

ACKNOWLEDGEMENTS

Gostaria de agradecer primeiramente a CAPES pela concessão da minha bolsa, sem ela este trabalho teria sido inviável. Outro grande agradecimento vai ao meu orientador Dr. Márcio Teixeira de Mendonça, por todo conhecimento transmitido, dedicação e paciência. E por último a minha família pelo suporte.

ABSTRACT

The present work investigates the stability of compressible binary planar jets. Different from a homogeneous jet, where a single chemical species is present, the binary jet may have strong density gradients due to the choice of the chemical species considered in each stream. The work is divided in two parts. The first part consists of the analysis of stability using linear stability theory. The goal is to identify the possible instability modes for simple and co-flowing jets and investigate the effect of density gradients on the flow structure, growth rates, unstable frequency range and disturbance phase speed for each mode. The effect of species concentration on free shear layer stability has been reported previously in the literature, but detailed comparisons between stability modes and characteristics for a range of density ratios typical of oxygen and hydrogen mixtures as well as the identification of inner and outer sinuous and varicose modes are new. For the co-flowing jet four different modes are found, the inner and outer shear layers both have sinuous and varicose modes. Both for the sinuous and varicose modes the simple jet is more unstable when the fluid with the highest density is at the inner jet, with amplification rates twice as high as the lowest density ratio considered, but the range of unstable frequencies can be four times lower. The sinuous mode is less dispersive than the varicose and the disturbance speeds may vary by one order of magnitude with density ratio. For coflowing jets the external mode is up to seven times more unstable, but this is due to the choice of the velocity ratio considered. For the inner mode the density gradient has a stabilizing effect, regardless of which specie is present at the center of the jet. The co-flowing jet is more dispersive, except for the varicose inner mode. The variation of phase speed with density gradient is not as strong as in the simple jet. The second part of the work is the study of stability by use of parabolized stability equations (PSE). The Parabolized Stability Equations (PSE) results are obtained for a simple planar jet consisting of only one gas. Initial conditions for the PSE are obtained from the Linear Stability Theory (LST) numerical code used in the first part. Results of this analysis are reduced due to the early stages of numerical code.

Palavras-chave: LST. PSE. Hidrodinamic Stability. Instability. Jet.

CARACTERÍSTICAS DE ESTABILIDADE DE JATOS PLANARES BINÁRIOS

RESUMO

O trabalho atual investiga a estabilidade de jatos compressíveis simples e binários. Diferente de um jato homogêneo, onde uma única espécie está presente, no jato binário fortes gradientes podem estar presentes na massa específica devido a diferentes espécies consideradas nos jatos. O trabalho é dividido em duas partes. A primeira parte trata da análise de estabilidade com uso da teoria linear. O objetivo é identificar os modos instáveis para a configuração de jato simples e de jato composto (co-flowing), também estudar o efeito de gradientes de fração mássica na estrutura do escoamento, a taxa de amplificação, faixas instáveis de frequência e velocidade de fase para cada modo. O efeito da concentração de espécies no escoamento livre é documentado previamente na literatura, mas comparações detalhadas entre modos de estabilidade e características para uma faixa de razões de massa específica típicas de misturas de oxigênio e hidrogênio, assim como a identificação de modos internos, externos, sinuoso e varicoso é novo. Para o jato complexo (co-flowing), quatro modos diferentes são encontrados, as camadas cisalhantes internas e externas possuem ambos modos varicosos e sinuosos. Para ambos os modos, sinuoso e varicoso, o jato simples é mais instável quando o fluido mais denso está no jato interno, com taxas de amplificação duas vezes maiores comparadas com a razão com menor densidade, mas com a faixa de frequência instáveis pode ser quatro vezes menos. O modo sinuoso é menos dispersivo que o varicoso e a velocidade das perturbações pode variar em uma ordem de magnitude com a razão de massa específica. Para o jato co-fluente, o modo externo é até sete vezes mais instável, mas isso é devido a escolha da razão de velocidade. Para o modo interno, o gradiente de massa específica tem um efeito estabilizante, independente de qual espécie estiver no centro do jato. O jato complexo, é mais dispersivo, exceto para o modo interno varicoso. A variação da velocidade de fase com o gradiente de massa específica não é tão forte como no jato simples. A segunda parte é o desenvolvimento e estudo de estabilidade usando equações parabolizadas. Os resultados das Equações de Estabilidade Parabolizadas (PSE) são obtidos para o jato simples considerando somente um gás. As condições iniciais para o Equações de Estabilidade Parabolizadas (PSE) são obtidas usando o código da primeira parte, que faz uso da Teoria de Estabilidade Linear (LST). Resultados obtidos com essa análise são escassos, devido ao código não estar totalmente desenvolvido.

Palavras-chave: LST. PSE. Estabilidade Hidrodinâmica. Instabilidade. Jato.

LIST OF FIGURES

	<u>Page</u>
2.1 Velocity profile $\bar{u}(y)$ for simple and co-planar jet.	21
3.1 (a) Sinuous and (b) varicose fluid topology	41
3.2 Mass fraction, simple and co-planar jet profiles as a function of y coordinate.	42
3.3 Sinuous mode spatial amplification rate α_i as a function of angular frequency ω for different gas ratios. Mach number = 0.9. Simple jet configuration.	44
3.4 Sinuous mode streamwise wavenumber α_r as a function of angular frequency ω for different gas ratios. Mach number = 0.9. Simple jet configuration.	44
3.5 Sinuous mode phase velocity cp as a function of angular frequency ω for different gas ratios. Mach number = 0.9. Simple jet configuration.	45
3.6 Sinuous mode lines of constant vorticity for the largest spatial growth rate α_i for $R_{\text{ratio}} = 0.25$ Positive values in continuous black lines, negative values in dashed lines. Vorticity range from -3.0 to 3.0	46
3.7 Sinuous mode lines of constant vorticity for the largest spatial growth rate α_i for $R_{\text{ratio}} = 1.0$ Positive values in continuous black lines, negative values in dashed lines. Vorticity range from -3.0 to 3.0	46
3.8 Sinuous mode lines of constant vorticity for the largest spatial growth rate α_i for $R_{\text{ratio}} = 4.0$ Positive values in continuous black lines, negative values in dashed lines. Vorticity range from -3.0 to 3.0	47
3.9 Pressure $\hat{p}(y)$ and normal velocity component $\hat{v}(y)$ eigenfunctions for the sinuous mode largest spatial growth rate α_i for different gas ratios R_{ratio} . Mach number = 0.9. Simple jet configuration.	48
3.10 Streamwise velocity component eigenfunction $\hat{u}(y)$ for the sinuous mode largest spatial growth rate α_i for different gas ratios R_{ratio} and Mach number = 0.9. Simple jet configuration.	49
3.11 Varicose mode spatial amplification rate α_i as a function of angular frequency ω for different gas ratios. Mach number = 0.9. Simple jet configuration.	50
3.12 Varicose mode streamwise wavenumber α_r as a function of angular frequency ω for different gas ratios. Mach number = 0.9. Simple jet configuration.	50

3.13	Varicose mode phase velocity cp as a function of angular frequency ω for different gas ratios. Mach number = 0.9. Simple jet configuration.	51
3.14	Varicose mode lines of constant vorticity for the largest spatial growth rate α_i for $R_{\text{ratio}} = 0.25$. $Ma = 0.90$. Positive values in continuous black lines, negative values in dashed lines. Vorticity range from -3.0 to 3.0 . . .	51
3.15	Varicose mode lines of constant vorticity for the largest spatial growth rate α_i for $R_{\text{ratio}} = 1.0$. $Ma = 0.90$. Positive values in continuous black lines, negative values in dashed lines. Vorticity range from -3.0 to 3.0 . . .	52
3.16	Varicose mode lines of constant vorticity for the largest spatial growth rate α_i for $R_{\text{ratio}} = 4.0$. $Ma = 0.90$. Positive values in continuous black lines, negative values in dashed lines. Vorticity range from -3.0 to 3.0 . . .	52
3.17	Pressure $\hat{p}(y)$ and normal velocity component eigenfunction $\hat{v}(y)$ for the varicose mode for the largest spatial growth rate α_i for different gas ratios R_{ratio} and Mach number = 0.9. Simple jet configuration.	53
3.18	Streamwise velocity component eigenfunction $\hat{u}(y)$ for the varicose mode for the largest spatial growth rate α_i for different gas ratios R_{ratio} and Mach number = 0.9. Simple jet configuration.	54
3.19	Spatial amplification rate α_i as a function of angular frequency ω , for different gas ratios. Mach number = 0.9. Sinuous external mode. Co-planar jet configuration.	57
3.20	Spatial amplification rate α_i for the sinuous mode as a function of angular frequency ω , for different gas ratios. Mach number = 0.9. Sinuous internal mode. Co-planar jet configuration.	57
3.21	Wavenumber α_r as a function of angular frequency ω , for different gas ratios R_{ratio} . Mach number = 0.9. Sinuous external mode. Co-planar jet configuration.	58
3.22	Wavenumber α_r as a function of angular frequency ω , for different gas ratios R_{ratio} . Mach number = 0.9. Sinuous internal mode. Co-planar jet configuration.	58
3.23	Phase velocity cp as a function of angular frequency ω , for different gas ratios. Mach number = 0.9. Sinuous external mode. Co-planar jet configuration.	59
3.24	Phase velocity cp as a function of angular frequency ω , for different gas ratios. Mach number = 0.9. Sinuous internal mode. Co-planar jet configuration.	60

3.25	Lines of constant vorticity for sinuous mode with the largest spatial amplification rate α_i of both internal and external modes, for $R_{\text{ratio}} = 0.25$. Vorticity range from -3.0 to 3.0. Positive values in continuous black lines, negative values in dashed lines.	60
3.26	Lines of constant vorticity for sinuous mode with the largest spatial amplification rate α_i of both internal and external modes, for $R_{\text{ratio}} = 1.0$. Vorticity range from -3.0 to 3.0. Positive values in continuous black lines, negative values in dashed lines.	61
3.27	Lines of constant vorticity for sinuous mode with the largest spatial amplification rate α_i of both internal and external modes, for $R_{\text{ratio}} = 4.0$. Vorticity range from -3.0 to 3.0. Positive values in continuous black lines, negative values in dashed lines.	61
3.28	Pressure $\hat{p}(y)$ and normal velocity component $\hat{v}(y)$ eigenfunction for the sinuous mode with maximum spatial amplification rate α_i for different gas ratios R_{ratio} and Mach number = 0.9, external mode, co-planar jet configuration.	62
3.29	Pressure $\hat{p}(y)$ and normal velocity component $\hat{v}(y)$ eigenfunction for the sinuous mode with maximum spatial amplification rate α_i for different gas ratios R_{ratio} and Mach number = 0.9, internal mode, co-planar jet configuration.	64
3.30	Streamwise velocity component eigenfunction $\hat{u}(y)$ for sinuous mode with maximum spatial amplification rate α_i for different gas ratios R_{ratio} and Mach number = 0.9, external mode, co-planar jet configuration.	65
3.31	Streamwise velocity component eigenfunction $\hat{u}(y)$ for the sinuous mode with maximum spatial amplification rate α_i for different gas ratios R_{ratio} and Mach number = 0.9, internal mode, co-planar jet configuration.	66
3.32	Spatial amplification rate α_i as a function of angular frequency ω , for different gas ratios. Mach number = 0.9. Varicose external mode. Co-planar jet configuration.	67
3.33	Spatial amplification rate α_i as a function of angular frequency ω , for different gas ratios. Mach number = 0.9. Varicose internal mode. Co-planar jet configuration.	67
3.34	Wavenumber α_r as a function of angular frequency ω , for different gas ratios. Mach number = 0.9. Varicose external modes. Co-planar jet configuration.	68
3.35	Wavenumber α_r as a function of angular frequency ω , for different gas ratios. Mach number = 0.9. Varicose external modes. Co-planar jet configuration.	68

3.36	Phase velocity cp as a function of angular frequency ω for different gas ratios. Mach number = 0.9. Varicose external mode. Co-planar jet configuration.	69
3.37	Phase velocity cp as a function of angular frequency ω for different gas ratios. Mach number = 0.9. Varicose internal mode. Co-planar jet configuration.	70
3.38	Lines of constant vorticity for varicose mode with the largest spatial amplification rate α_i of both internal and external modes, for $R_{\text{ratio}} = 0.25$. Vorticity range from -3.0 to 3.0. Positive values in continuous black lines, negative values in dashed lines.	70
3.39	Lines of constant vorticity for varicose mode with the largest spatial amplification rate α_i of both internal and external modes, for $R_{\text{ratio}} = 1.0$. Vorticity range from -3.0 to 3.0. Positive values in continuous black lines, negative values in dashed lines.	71
3.40	Lines of constant vorticity for varicose mode with the largest spatial amplification rate α_i of both internal and external modes, for $R_{\text{ratio}} = 4.0$. Vorticity range from -3.0 to 3.0. Positive values in continuous black lines, negative values in dashed lines.	71
3.41	Pressure $\hat{p}(y)$ and normal velocity component $\hat{v}(y)$ for the varicose mode with maximum spatial amplification rate α_i for different gas ratios R_{ratio} and Mach number = 0.9, external mode, co-planar jet configuration. . . .	72
3.42	Pressure $\hat{p}(y)$ and normal velocity component $\hat{v}(y)$ for the varicose mode with maximum spatial amplification rate α_i for different gas ratios R_{ratio} and Mach number = 0.9, internal mode, co-planar jet configuration. . . .	73
3.43	Streamwise velocity component $\hat{u}(y)$ for the varicose mode with maximum spatial amplification rate α_i for different gas ratios R_{ratio} and Mach number = 0.9, external mode, co-planar jet configuration.	77
3.44	Streamwise velocity component $\hat{u}(y)$ for the varicose mode with maximum spatial amplification rate α_i for different gas ratios R_{ratio} and Mach number = 0.9, internal mode, co-planar jet configuration.	78
3.45	Lines of constant vorticity disturbances. Maximum spatial amplification rate α_i is considered for both internal and external modes, $R_{\text{ratio}} = 0.25$ and $Ma = 0.90$. Positive values in continuous black lines, negative values in dashed lines. Range of vorticity levels from -3.0 to 3.0.	79
3.46	Lines of constant vorticity disturbances. Maximum spatial amplification rate α_i is considered for both internal and external modes, $R_{\text{ratio}} = 4.0$ and $Ma = 0.90$. Positive values in continuous black lines, negative values in dashed lines. Range of vorticity levels from -3.0 to 3.0.	80

3.47	LST Eigenfunctions \hat{u} , \hat{v} and \hat{p} for the sinuous mode with gas ratio $R_{ratio} = 1.0$ and Mach number = 0.9, simple jet configuration.	81
3.48	PSE Eigenfunctions \hat{u} , \hat{v} and \hat{p} for the sinuous mode with gas ratio $R_{ratio} = 1.0$ and Mach number = 0.9, simple jet configuration.	82
3.49	Wavenumber α_r and growth rate α_i evolution for the sinuous mode with gas ratios $R_{ratio} = 1.0$ and Mach number = 0.9, simple jet configuration.	83
3.50	Sinuous mode lines of constant vorticity for $R_{ratio} = 1.0$ and $Ma = 0.9$. Positive values in continuous black lines and negative values in dashed lines, vorticity range from -3.0 to 3.0	84

LIST OF TABLES

	<u>Page</u>
3.1 Largest spatial growth rate α_i and corresponding angular frequency ω , wavenumber α_r and phase speed cp for the simple jet.	43
3.2 Maximum spatial amplification rate α_i and corresponding angular frequency ω , wavenumber α_r and phase speed cp for the sinuous mode, co-planar jet.	55
3.3 Maximum spatial amplification rate α_i and corresponding angular frequency ω , wavenumber α_r and phase speed cp for the varicose instability, co-planar jet.	56
3.4 Spatial growth rate α_i and corresponding angular frequency ω , wavenumber α_r and phase speed cp for the simple jet.	75

LIST OF SYMBOLS

a	– Complex exponent
$a_1, a_2, a_3, a_4 a_5$	– Coefficients of the heat capacity polynomial
A, B, C, D, E, F, G, H	– Coefficients for the diffusion collision integral
A_k, B_k, C_k, D_k	– Coefficients for the thermal conductivity
$A_\mu, B_\mu, C_\mu, D_\mu$	– Coefficients for the viscosity
$A_m, B_m, C_m, D_m, E_m, R_m$	– 5×5 matrices given in the appendix
b	– Representation of rapid variations of the shape function
cp	– Heat capacity at constant pressure
hc_p	– Heat capacity at constant pressure
c_v	– Heat capacity at constant volume
D	– Mass diffusivity
D_{ab}	– Diffusion coefficient
e	– Internal energy
f_i	– External forces
h	– Enthalpy
i	– Imaginary number ($i = \sqrt{-1}$)
k	– Thermal conductivity
L	– Reference length value
M	– Gas mass
Mo	– Molar mass
p	– Pressure
R	– Gas constant
R_U	– Universal gas constant
R_{ratio}	– ratio of gas constants
t	– Time
T	– Temperature
u_{sound}	– Speed of sound $\sqrt{\gamma R_0^* T_0^*}$
u, v, w	– Instantaneous velocity components
x, y, z	– Cartesian coordinate system
X_n	– Molar fraction of n specie
S_n	– Mass fraction of n specie

GREEK

α_r	– Streamwise wavenumber
α_i	– Streamwise growth rate
β	– Spanwise wavenumber
$\delta_{i,j}$	– Kronecker delta
ε	– Characteristic Lennard-Jones energy

η	– Vorticity
λ	– Bulk viscosity
μ	– Dynamic viscosity
ν	– Kinematic viscosity
γ	– Heat capacity ratio – $\frac{c_{p0}^*}{c_{v0}^*}$
Γ	– Growth rate (Section PSE)
ω	– Angular frequency
Ω_d	– Diffusion collision integral
ρ	– Density
σ	– Characteristic Lennard-Jones Length
$\sigma_{i,j}$	– Stress Tensor
χ	– Exponential oscillatory term

SUB/SUPERSCRIPTS

$\hat{()}$	– dimensionless eigenfunction / complex amplitude
$()^*$	– dimensional variable
$()'$	– indicates that the variable is a perturbation
$()_0$	– reference fixed value
$\overline{()}$	– mean variable, from the base flow
$()_x$	– Derivative in the x coordinate
$()_y$	– Derivative in the y coordinate
$()_{mix}$	– Property consisting of a mixture of 2 gases
	– Variables without any superscript are dimensionless

DIMENSIONLESS NUMBERS

Ec	– Eckert Number – $Ma^2(\gamma - 1) = \frac{u_0^*}{c_{p0}^* T_0^*}$
Le	– Lewis Number – $k_0^*/\rho_0^* D_n^* c_{p0}^*$
Ma	– Mach Number – u^*/u_{sound}^*
Re	– Reynolds Number – $\rho^* u^* L^*/\mu^*$
Sc	– Schmidt Number – $\mu_0^*/(\rho_0^* D_0^*)$

CONTENTS

	<u>Page</u>
1 INTRODUCTION	1
1.1 Binary flows	3
1.2 Parabolized stability equation	11
1.3 Objective	13
2 MATHEMATICAL MODEL	15
2.1 LST	15
2.1.1 Linear stability theory	16
2.1.2 Base flow	20
2.1.2.1 Gas ratio (R_{ratio})	22
2.2 Parabolized stability equation	22
2.2.1 Non-dimensional parameters	24
2.2.2 Non-dimensional equations	24
2.2.3 Perturbation equations	26
2.2.4 Properties of mixtures	31
2.2.4.1 Density	31
2.2.4.2 Gas constant	32
2.2.4.3 Heat capacity	32
2.2.4.4 Mass diffusivity	33
2.2.4.5 Thermal conductivity	34
2.2.4.6 Viscosity	34
2.2.5 Linearized PSE for incompressible flow	35
2.2.6 Discretization	36
2.3 Numerical method	38
2.3.1 LST	38
2.3.2 PSE	38
2.3.2.1 Normalization condition	38
3 RESULTS	41
3.1 LST	42
3.1.1 Simple jet	42
3.1.1.1 Results for the sinuous mode	43
3.1.1.2 Results for the varicose mode	47

3.1.2	Co-planar jet	54
3.1.2.1	Results for the varicose mode	63
3.1.2.2	Sinuous and varicose mode mixing	74
3.2	PSE	74
3.2.1	Simple jet	75
4	CONCLUSION	85
4.1	Future works	85
	REFERENCES	87
	APPENDIX A - COMPLEMENTARY TERMS AND EQUATIONS	93
A.1	Non-dimensional equation of state	93
A.2	Equations: linear stability analysis	93
A.3	Taylor's expansion of dependent variables	98
A.4	Partial derivatives of perturbations	99
A.5	PSE equations	100
A.6	Elements of the matrices	102

1 INTRODUCTION

The transition phenomenon leads a fluid flow from a laminar behavior to random turbulent flow, and the study and understanding of this phenomenon have been an important part of fluid dynamics for more than a century now. This laminar-turbulent transition phenomenon is of great importance in fluid dynamics, mainly in aeronautical areas, where the design of vehicles and devices are in need of advanced performance, as general examples we have: combustion chambers, planes and missiles. However, transition is a very complex topic, and yet it is not completely understood.

It is important to highlight that when we talk about fluid flows, there are several cases in which some specific flow regime is preferred over others. It is possible to demonstrate this with some simple examples. Let's take a wind tunnel, here we have to assure a laminar fluid flow inside it, in order to avoid unrealistic and / or undesirable forces over the testing model, and with that to achieve a reliable experiment and consequently reliable set of data. Other example worth mentioning is the laminar flow over an airfoil. Once the laminar flow is established around it, the airfoil presents a drag reduction, which consequently leads to flight improvements and less fuel consumption.

In the turbulent regime, it is possible to mention the scramjet and ramjet engines. In both cases, a turbulent regime is desired inside the combustion chamber, but in scramjets this happens in a supersonic velocities. Supersonic fluid flow complicate the combustion process, because such regime has a stabilizing effect, decreasing the fuel-oxidizer mixing. In this case, instead of having a laminar flow, a turbulent one is not only preferred, but essential, once turbulence is needed to a fuel-oxidizer mixture to exists and to an efficient combustion process to occur.

Examples like these are important to emphasize that the study of transition phenomenon is very important and can lead to safer and more optimized devices and vehicles. Also, it allows us to understand the physics and mechanisms behind the transition process, as well as, to predict desirable and undesirable behaviors, e.g., the position where a disturbance can start to grow over an airfoil or where the fluid stabilizes inside a scramjet combustion chamber.

Essential work on stability of parallel flow of inviscid fluid can be credited to Helmholtz (1868), Kelvin (1871) and Rayleigh (1945) in the nineteenth century. Their work consisted of considering inertial instability of homogeneous incompress-

ible fluid, including its modification when transverse variation of density is present in the flow (Kelvin-Helmholtz instability). From these authors, we can highlight Lord Rayleigh, who in 1880 introduced an equation for hydrodynamic instability of inviscid parallel shear flow, equation that bears his name ever since. This equation is being mentioned because it is, basically, a simplified version of the Orr-Sommerfeld Equation. The simplification from the Orr-Sommerfeld to Rayleigh's equation is obtained when the viscosity is neglected.

For many years the analysis of instability phenomenon had relied on the formulation derived by Orr (1907) and Sommerfeld (1908) (Orr-Sommerfeld equation). With their formulation, it was possible to model the amplification of two-dimensional waves, of a fluid flow between two parallel flat plates. This early formulation, assumed that the mean flow could be represented by $u = u(y)$, i.e., the mean flow was assumed to be independent of the streamwise direction x . Therefore, with the parallel assumption, the partial differential equation could be simplified to a ordinary differential equation. This method can be called 'local analysis' because its non-explicitly dependence of the streamwise coordinate. Further simplification can be imposed with the assumption of temporal growth or decay of disturbances, gaining the name of temporal analysis. The simplification is made by assuming the frequency to be $\omega = \omega_r + i\omega_i$. Thanks to advances in mathematical and computational methods spatial analysis also became possible, which represents disturbances growing in space, by assuming $\alpha = \alpha_r + i\alpha_i$, where the imaginary part represents the disturbance growth rate, consequently leading to more complex equations.

The next step in stability analysis, since the development of the Orr-Sommerfeld equation, was taken by Tollmien (1929), whose work solved the Orr-Sommerfeld equation in a boundary layer flow. Tollmien, by neglecting the slow growth of the boundary streamwise direction, was able to obtain a parallel flow, and consequently, able to predict the location where instability waves would start to be amplified (critical Reynolds number) and to compute the neutral stability curve. Some years later, Schlichting (1933) developed an extension of Tollmien's work. In this work, Tollmien's results were extended to include growth rates between the points on the neutral stability curve. The modeling of two-dimensional waves in the analysis are, what we call today, the Tollmien-Schlichting waves.

Experimental verification of Tollmien's predictions were only obtained in the post war period (SCHUBAUER; SKRAMSTAD, 1948). Before experimental validation the idea of amplification of small oscillation were highly distrusted. At the same time,

the experiments conducted by Schubauer and Skramstad had been poorly conducted in wind tunnels with high free stream turbulence. Nevertheless they found good agreement between the theory and the experiment. Underlining that they observed spatial growth and the theoretical formulation were to be modeled as temporal. Furthermore, the theory neglected non-linear terms.

In parallel we have the work of HAAR (1965), suggesting to study the flow evolution beyond the limit of linearized theory. The temporal evolution of the amplitude was dependent on itself, assuming that initially a small disturbance with small amplitude does not grows indefinitely in time but an equilibrium condition is achieved corresponding to a finite amplitude.

We have other contributors worth mentioning like Lees e Lin (1946), which extended the linear stability theory to compressible boundary layer.

Later, with the development of computers, more precise Orr-Sommerfeld equation results could be obtained. We can here mention the works of (MACK, 1965; MACK, 1975), in this respect. He mapped the unknown part of the linear theory at that time. He revealed that three dimensional modes are important at high Mach numbers and that they have no influence in incompressible flows. Associated with that is the discovery of higher modes, which up to this day bears his name, Mack modes . Also Gaster (1965) came up with the idea of solving the Orr-Sommerfeld equation directly for spatial growth. He found out a relation between spatial and temporal growth rates and, like Mack, today this relation bears Gaster's name.

Focusing now in the non-linear theory we have Stuart (1960). Stuart derived Landau's equation from the Navier-Stokes equation using the amplification rate of the disturbance as an expansion parameter. Similarly, Watson (1960) made its own derivation but with the amplitude of the disturbance as the parameter.

A more complete background of the development of instability theory is presented in Bertolotti (1991) thesis.

1.1 Binary flows

As already mentioned in the previous section, it is easy to show that the stability of compressible flows is a topic of great interest in the aeronautical industry. Regarding free shear layers, the three main aeronautical applications involving hydrodynamic stability are related to the generation of noise due to turbulence, the combustion stability in combustion chambers and high speed combustion in hypersonic vehicles.

Jet noise at the exit of gas turbines is associated with large and small turbulent structures that are the source of noise. Combustion stability is associated with the interplay of acoustics, hydrodynamic stability, turbulence and combustion unsteadiness. High speed combustion is required for hypersonic vehicles in order to reduce pressure losses due to shock waves, but compressibility has a strong stabilization effect that prevents the proper mixing of reactants in the combustion chamber.

The present investigation address the problem of stability of compressible jets considering different chemical species in the flow, representing streams of different concentrations of oxidizer and fuel. Both simple jets and co-flowing jets are considered. In a simple jet, fuel or oxidizer is discharged to an environment containing a certain concentration of oxidizer or fuel, respectively. In the case of co-flowing jet, an inner jet containing oxidizer or fuel and an outer jet containing fuel or oxidizer, respectively, issues from a nozzle where the ambient environment is of the same chemical species as the outer jet.

Frequently, the flow geometry is axissymmetric, but is not uncommon to find applications where the jets flow out of rectangular nozzles with a large aspect ratio. In this case the jet may be considered as a two-dimensional planar jet. There is a large body of work on axissymmetric jets, but a smaller number of studies considering planar jets. The following review of the literature considers mostly planar compressible jets of homogeneous and binary streams. The more recent publications that are relevant to the present investigation are considered. There are other articles dedicated to the presentation and discussion of classic papers on the subject.

Extensive work on the stability of compressible, uniform and binary flows, has been done. In an early work, [Jackson e Grosch \(1989\)](#) studied the spatial stability of a compressible mixing layer . The methodology and conclusions apply to other free shear layers in compressible flow in terms of the effect of Mach number, temperature ratios and direction of the most unstable modes. They classify the disturbances as subsonic, fast mode, slow mode and supersonic, depending on the phase speed and on the Mach number. The work also showed that the boundary conditions away from the shear layer support both exponentially decaying disturbances and radiating outgoing waves for the fast, slow and supersonic modes. The details of the slow and fast modes was latter complemented by the investigation of [Zhuang et al. \(1990\)](#).

One year latter, [Jackson e Grosch \(1990\)](#) investigated the stability of compressible mixing layers and identified the transition from convective to absolute instability . They found that subsonic mixing layers are convectively unstable if there is no

strong backflow. They defined an expression for the convective Mach number for flows with different chemical species and show that this definition is not associated with the propagation velocity of large vortical structures or on the phase speed of the fastest growing mode. Nevertheless the convective Mach number proposed is the relevant compressibility parameter for binary mixing layers. Their definition of convective Mach number for binary mixing layers is defined as

$$M_c = M(1 - \beta_U)/(1 + \sqrt{\beta_\gamma/\beta_\rho}).$$

where M is the Mach number of the fast stream, β_U, β_γ and β_ρ are the velocity, specific heat ratio and density ratios between the fast and slow streams.

The experimental study of planar compressible jets of [Gutmark et al. \(1991\)](#) showed the effect of compressibility on the flow stability. Their motivation was the enhanced mixing when using rectangular and co-planar jets compared to a simple cylindrical jet. The convective Mach number was varied by changing the gas composition and temperature in the inner stream. The results show that rectangular jets are more unstable than circular jets and that, for the tests considered, the interface between the inner and outer jets in the coaxial configuration is also more unstable than the circular jet.

[Shih et al. \(1992\)](#) also studied the stability of rectangular jets in the compressible flow regime. They found that for very low mach numbers the varicose mode is the most unstable, but as compressibility effects increase the sinuous mode becomes relevant and then predominant at transonic and supersonic conditions. They also collected noise measurements and found relevant screech tones that depend on the aspect ratio of the nozzle.

The stability of rectangular jets has also been studied by [Tam e Thies \(1993\)](#), using a vortex sheet model, found different instability modes, where the dominant mode is termed the central mode since the largest fluctuation amplitude is located at the center of the jet. Corner instability modes are relevant close to the nozzle jet exit and are responsible for smearing the jet into a more round profile downstream.

The stability of very large aspect ratio rectangular jets in compressible flows was investigated by [Miles \(1996\)](#) with an interest in increase mixing in high convective Mach number conditions. His interest was on applications with an array of parallel nozzles in order to increase mixing between the jet and the ambient gas. Growth

rates, phase speed and disturbance wavelength are reported for different nozzle spacings.

Stanley e Sarkar (1997) presented results from numerical simulations of shear layers and planar jets. A detailed review of previous work on transitional and turbulent planar jet is presented. As also found latter by Reichert e Biringen (2007), two dimensional simulations are able to recover the initial stages of flow instability and development of the initial anisotropic structure, but result in stronger disturbances further downstream than experimental three dimensional results. The simulation of transition to turbulence in planar jets results in significant differences from experimental results since spanwise instabilities associated with the third degree of freedom are not present.

Grosch et al. (1997) studied the mixing characteristics of confined jets issuing from a rectangular nozzle in order to elucidate the enhancement of mixing due to inserts positioned at the nozzle exit. They used direct numerical simulations, considering a hot jet in a colder co-flowing stream. The numerical experiments considered a range of convective Mach numbers defined as $M_c = (U_1 - U_2)/(c_1 + c_2)$, where U_1, c_1 and U_2, c_2 are the velocities and sound speed at the jet and at the parallel co-flowing ambient fluid. The inserts generate counter rotating longitudinal vortices that are responsible increased mixing.

Kennedy et al. (1998) investigated the effect of temperature variations in compressible jets using boundary layer similar solutions for the base flow profiles. They found that a hot jet into a cold ambient have growth rates ten times greater then a jet in isothermal conditions and that the range of unstable frequencies is also greater. On the other hand a cold jet is more stable than the isothermal jet. The results are related to density gradients and have a greater effect on growth rate than compressibility effects.

Watanabe e Maekawa (2002), interested in jet noise, studied planar jets in the supersonic regimes using linear stability theory and direct numerical simulation. Two-dimensional sinuous mode disturbances are predominant under convective Mach number equal to 0.8 and above this limit, up to Mach 1.5, the dominant mode is the sinuous three-dimensional mode. Above convective Mach number of 1.5, two-dimensional disturbances are dominant, but sinuous mode is the preferred mode. Their results show the existence of radiating modes associated with noise propagation. They show details of the flow structure through vorticity and dilatation plots, which allow the identification of the dominant oscillation modes and the radiation

angle and intensity of sound waves. They show which mode is responsible for the generation of acoustic waves depending on their phase speed been subsonic or supersonic.

Suresh et al. (2008) experimentally studied the dependence of planar jet development on viscous effects by varying the Reynolds number of the flow in the range of 250 to 6250. The results show that at low Reynolds number large vortical structures are responsible for enhanced entrainment, spreading and jet decay, while at higher Reynolds number the flow structure has the characteristics of fully turbulent flows with more isotropic disturbances and a larger spectrum of scales. Due to the enhanced entrainment, low Reynolds number jets achieve similarity conditions for the mean components in the near field of the nozzle, but without achieving isotropic turbulent conditions. Investigation on the development of planar jets under different Reynolds number conditions confirmed Suresh's results regarding the mean velocity decay and jet half-width associated with the size of the corresponding coherent structures. The works presented further details of the turbulence statistics, turbulence scales and flow structures (DEO et al., 2008; DEO et al., 2013).

Another study that considered planar jets is the one developed by Reichert e Birnigen (2007), who considered a jet stream on a co-flowing ambient with velocity ratio of 1.67. In the work, three-dimensional numerical simulations were performed and revealed the inadequacy of two-dimensional studies in the latter stages of transition to turbulence. Despite the fact that the early instability linear regime is well represented by two-dimensional base flows, two-dimensional studies show much more organized structures as well as a more severe stabilization due to compressibility effects in the turbulent regime. Two years latter, HABLI et al. also published about plane jets in a co-flow environment in a turbulent regime to study the influence of co-flow velocity ratio on the mean flow properties and length of the potential core.

Weder (2012) investigated the stability and acoustics of compressible subsonic planar jets using linear stability theory. Imposing canonical velocity profiles typical or turbulent flows he was able to recover instability and acoustic modes that are relevant for noise generation and propagation. The analysis of disturbance energy balance presented suggests the main mechanisms associated with disturbance growth to be due to the production term in the Reynolds-Orr energy equation, while growth associated with thermal effects are minor.

Also considering realistic base flow profiles given by accurate boundary layer profiles, Quintanilha et al. (2015) studied the stability of incompressible and compressible

mixing layers. They found two instability modes for two stream coaxial jets and three different modes for three stream coaxial jets. The growth rates of these modes depend strongly on the vorticity thickness. The relevance of using accurate base flow profiles was highlighted.

Interested in mixing processes, another interesting investigation of planar jets was published [Datta e Sinhamahapatra \(2015\)](#). This study was made of planar jets going into a co-flowing ambient but in turbulent regime. The results present the main jet parameters such as jet spreading and inviscid core length as well as turbulence statistics and how these properties depend on the velocity ratio between the jet and co-flow. Latter, [Datta e Sinhamahapatra \(2016\)](#) and [Datta e Sinhamahapatra \(2016\)](#), presented additional results considering the effect of compressibility and show that the potential core and jet spreading do not strongly depend on the convective Mach number while the turbulence statistics do not become self-similar.

Regarding the study of binary mixtures in free shear layers, a number of publications may be found. [Kennedy e Gatski \(1994\)](#) presented results for laminar shear layers composed of nitrogen and hydrogen. The authors solved the self-similar boundary layer equations for compressible, binary mixing layers, considering variable properties such that Prandtl, Chapman-Rubesin and Lewis numbers vary continuously across the layer. The results show that variable properties have a significant effect on the velocity, temperature, density and mass fraction profiles. As a result, the vorticity structure decouples from the density profile for large density ratios. The variable properties results have strong implications for flow stability as shown latter in different investigations.

In a more extensive investigation than the one presented by [Kennedy e Gatski \(1994\)](#), [Kozusko et al. \(1996a\)](#) investigated the laminar flow structure of a binary, compressible mixing layer for thirty different combinations of gas mixtures. The gas properties are considered variable and dependent on temperature and mass fraction distributions, such that Lewis and Prandtl numbers vary considerably across the layer. The resulting velocity, density, temperature and mass fraction profiles are very different from profiles obtained for constant nondimensional numbers approximation and are not necessarily symmetric. The results also depend on the more dense gas being on the fast or slow stream. These results show the importance of correctly modeling the base flow for stability analysis. In the same subject, [Kozusko et al. \(1996b\)](#) studied the stability of compressible, binary mixing layers. The results are presented in terms of the ratio between the molecular mass on the two streams, since

it has a significant effect on the phase speeds, growth rates and range of unstable frequencies. Nevertheless the normalized growth rates for a given convective Mach number is not strongly dependent on the gas composition.

Hsu et al. (2004) considered the flow field of planar binary jets. The numerical and experimental results were obtained for low Reynolds numbers. They considered a mixture of oxygen and nitrogen issuing into the atmosphere from a vertically mounted nozzle. Due to the low Reynolds number range, gravitational forces were taken into consideration in the analysis, which showed the influence of density stratification and the interdependence of density distribution on the flow field.

The temporal linear stability of compressible binary shear layers with large density ratios was investigated by Fedioun e Lardjane (2005). The stabilizing effect of compressibility for convective Mach numbers above 0.6 was reported and showed to be independent of the density ratio. As compressibility effects increase, the most amplified mode becomes three-dimensional. For binary flows the most amplified mode, the corresponding wavelength and the wave speed, depend on the species considered, temperature distribution and free stream velocities, and not only on the convective Mach number.

Salemi e Mendonça (2008) investigated the stability of compressible mixing layers when different chemical species are present on the two streams. They studied the effect of compressibility and mass fraction stratification on the mixing layer stability. Following the work of Salemi and Mendonça, Mendonça (2014) investigated the stability of mixing layers modified by jets and wakes. Both the effect of more complex flow structures and the effect of large density gradients due to different chemical species in each stream were assessed. The base flow velocities, temperature and mass fraction distributions were given by the solution of boundary layer equations in an intent to have more realistic conditions than the ones given by canonical profiles. This approach is similar to the formulation of Salemi, who used similarity solutions for the binary compressible base flow. The boundary layer solution allows the consideration of temperature gradient and mass fraction distribution dependent properties, such as viscosity, specific heat, etc, which has shown to have a significant effect on the stability characteristics. The results show that the combined effect of different species and distortion of the mixing layer by jets and wakes have a strong effect on the stability characteristics. Stability diagrams show significant differences whether an oxygen jet on a hydrogen ambient or an hydrogen jet on a oxygen ambient is considered. The heavier fluid at the jet is two times more unstable than

the lighter fluid at the jet.

Schumaker e Driscoll (2012) investigated experimentally coaxial jets also considering large density ratios. They varied the velocity ratio, density ratio, diameters of the inner and outer jet and used hydrogen and oxygen, as well as methane and oxygen streams, typical reactants in rocket engines. The mixing measure was the length necessary to achieve a given concentration of species. Results were compared to different entrainment models and show good comparisons for some of the models and the weaknesses of some other models when strong density or velocity ratios are considered. The flow conditions investigated did not show significant dependence on the Reynolds number.

The effect of strong temperature gradients and disturbances propagation angle on O₂/H₂ mixing layers where studied by Freitas et al. (2014) using linear stability analysis. Growth rates as a function of temperature gradient and Mach number were presented and the differences due to the simplified hypothesis of canonical base flow profiles versus base flow profiles given by the solution of boundary layer equations were highlighted.

The results obtained by Mendonça (2014) were continued by Manco et al. (2015), introducing compressible mixing layers, jets and wakes composed of different chemical species in the different stream. They used direct numerical simulations to analyze the flow structures resulting from the stability of complex mixing layers modified by wakes and jets. Again, realistic base flow variables were evaluated using results from boundary layer simulations, and velocity, temperature and mass fraction profiles are significantly different from canonical profiles used in other studies. The results show that the more complex base flows enhance instability, which is responsible for stronger mixing between reactants. The fastest growing disturbances for the different conditions considered were determined.

The stability of compressible binary planar jets was investigated by Rogenski et al. (2017) using direct numerical simulations. The laminar viscous flow is obtained from Navier-Stokes simulations and stability results are obtained from a high order of accuracy Euler solver. They considered two different cases, a hydrogen jet in a oxygen environment and a oxygen jet on a hydrogen environment. They found that, for the conditions investigated, the sinuous mode when an oxygen jet is considered, is the most unstable. The flow structure are presented through the velocity and vorticity fields in the nonlinear regime, for the most unstable sinuous and varicose cases.

Following the methodology presented by Rogenski et al. (2017), Lacerda et al. (2018) performed additional direct numerical simulations of planar jets and mixing layers in the compressible flow regime. Results were compared to linear stability theory results for a range of Mach numbers, showing the stabilizing effect of compressibility. The nonlinear regime was also studied through the analysis of the vorticity field, showing the structure of the sinuous and varicose instability development.

The literature review presented above is far from exhaustive, but presents the main topics that are relevant for the investigation in the present research. As seen above, there is a considerable amount of work on the stability of mixing layers and jets in compressible homogeneous flows. Considering binary free shear flows, there was an intense interest in the nineteen nineties and early two thousand. Since then, the work on compressible binary mixing layers started by Salemi e Mendonça (2008) has evolved, including studies of more complexity, in order to include binary and compressible flow configurations (MENDONÇA, 2014; MANCO et al., 2015; ROGENSKI et al., 2017; LACERDA et al., 2018).

The present investigation extends existing results by considering simultaneously the co-flowing / coaxial planar jet configuration and different chemical species in each stream. The investigation is concerned with the stability of planar jets in a quiescent environment, where the jet and the ambient fluid are of different chemical species. Both simple planar jets and co-flowing jets are considered, where the jet stream in the inner jet is of a different chemical species from the jet in the outer stream and ambient gas. Results are discussed in terms of growth rates, range of unstable frequencies, phase speeds, wavenumbers, eigenfunctions and flow structure. Stability results for four different combinations of varicose and sinuous, inner and outer modes are identified and compared.

1.2 Parabolized stability equation

After all the struggle and limitations of the past decades a new approach, and more efficient one, in the stability analysis was developed by Herbert and Bertolotti. They developed a stability analysis which allows spatial formulation in nonparallel stability problems, maintaining its validity for both, non-linear and linear regimes (HERBERT; BERTOLOTTI, 1987; BERTOLOTTI; HERBERT, 1991). This new formulation is valid since the fluid flow quantities/properties are varying slowly in the streamwise direction. The resulting set equations of this approach are parabolic and receive the name of Parabolized Stability Equation (PSE). The PSE formulation follows the same initial steps of other well known stability problems. Initially, the

flow properties are decomposed in two, a mean flow quantity plus a disturbance. These variables, are then substituted into the Navier-Stokes set of equations and the quantities satisfying the mean flow are removed. The innovation of PSE lies in the definition of the disturbances. Disturbances are defined as a product of a shape function and an exponential term, containing a streamwise coordinate dependence in both terms.

The substitution of the shape function and the exponential term into the disturbance equations, with the assumption that the shape function, wavenumber and growth rate vary slowly in the streamwise direction, ends up in a set of parabolic equations that can be marched downstream of the flow. The simplification provided by the PSE formulation, that is, the reduction from elliptic equations to parabolic ones, holds its validity if and only if the stability problem is governed by information traveling downstream. Because of that it is called convective instability.

Application of PSE can be seen in a large range of instability problems, starting from simple problems as, for example, linear incompressible ones to high speed flows with nonlinear instability development. In the work of Bertolotti et al. (1992), linear and nonlinear development of Tollmien-Schlichting waves in flat plate boundary layers are presented. The results of the PSE are compared with results obtained from Direct Numerical Simulation (DNS), and it presents very good agreement in the comparison. For the numerical model, a spectral collocation method is used to discretize the equations in the normal coordinate, while finite differences is used in the streamwise direction.

More recently, Gloor et al. (2013) published a study on the stability of coaxial jets. Such study investigates the influence parameter on the linear stability characteristics of viscous compressible coaxial jet flow at subsonic flow velocities. The impact of parameters on disturbance development, such as Reynolds number, Mach number, temperature and velocity ratio between bypass flow and core stream are studied, considering the influence of the azimuthal.

Another important work is published by Weder (2012), where a linear stability solver for a two-dimensional, compressible and viscous jet is developed. The author investigates the temporal and spatial linear stability of the plain jet by deriving a compressible counterpart to the Orr-Sommerfeld equation, which is numerically solved. Further, investigation on the acoustic modes is performed but this part is not actually treated in this work.

1.3 Objective

The current work is split into two parts. The first one is based on linear stability theory. In this part, investigation of compressible binary planar jets is performed. Different from homogeneous jet, where a single chemical specie is present, the binary jet may present different density gradients, as a consequence of choosing chemical species in each stream. Inside this first part of the work, two configurations of jet are used, a simple plane jet and a binary jet. The main goal is to identify the instability modes for the simple and the co-flowing jets and also to investigate the effect of density gradients on the flow structure, growth rates, unstable frequency range and disturbance phase speed for each mode. Linear stability theory is used to determine stability characteristics of different configurations taking into concern sinuous and varicose modes.

The second part is a continuation of the first part, however the problem is solved by use of parabolized stability equations. Both parts try to complement previous mentioned work of [Gloor et al. \(2013\)](#). The same methodology will be employed. Selection of the current boundary layer equation in the base flow solution, is justified by [Mendonça \(2014\)](#), whose work shows that velocity, temperature, density and mass fraction profiles differs greatly from those obtained by hyperbolic tangent/secant commonly used in stability analysis of jets, wakes and mixing layers. Initially, this second part would replicate the simple and the binary jet studied in the first part adding to it more complexity. However due to a series of complications the code is not fully developed, limiting the obtainment of results. The code in its actual state is limited to the simple jet configuration with fixed gas ratio ($R_{ratio} = 1/\rho_{ratio} = 1$), which means that the jet and the quiescent ambient have the same density. Only sinuous mode in a limited angular frequency ω_r range is calculated. Gas is assumed to be incompressible.

A separate program was developed in order to compute the evolution of the base flow, program that would be able to increase the complexity of the problem by introducing variable properties, but as a consequence of the great amount of time dedicated to the PSE to work with simple configurations it is not used. The base flow is considered steady for both PSE and LST.

2 MATHEMATICAL MODEL

In this chapter formulation for both Linear stability theory (LST) and Parabolized stability equation (PSE) are presented.

2.1 LST

The flow configuration consists of two streams issuing from a nozzle into a quiescent ambient. The fast stream of a given chemical species is surrounded by a slower stream of a different chemical species, as presented in Figure 2.1.

The problem is formulated as a stability problem by reducing the compressible Euler equations to the compressible version of the Rayleigh stability equation. Starting with the non-dimensional Euler equations in Cartesian coordinates for three-dimensional compressible flows of a binary mixture of two different gases, with reference values given by the stream at the center, the set of governing equations are:

Continuity equation

$$\frac{\partial \rho}{\partial t} + \frac{\partial \rho u}{\partial x} + \frac{\partial \rho v}{\partial y} + \frac{\partial \rho w}{\partial z} = 0. \quad (2.1)$$

Streamwise momentum equation

$$\rho \frac{\partial u}{\partial t} + \rho u \frac{\partial u}{\partial x} + \rho v \frac{\partial u}{\partial y} + \rho w \frac{\partial u}{\partial z} = -\frac{1}{\gamma_1 Ma^2} \frac{\partial p}{\partial x}. \quad (2.2)$$

Normal momentum equation

$$\rho \frac{\partial v}{\partial t} + \rho u \frac{\partial v}{\partial x} + \rho v \frac{\partial v}{\partial y} + \rho w \frac{\partial v}{\partial z} = -\frac{1}{\gamma_1 Ma^2} \frac{\partial p}{\partial y}. \quad (2.3)$$

Spanwise momentum equation

$$\rho \frac{\partial w}{\partial t} + \rho u \frac{\partial w}{\partial x} + \rho v \frac{\partial w}{\partial y} + \rho w \frac{\partial w}{\partial z} = -\frac{1}{\gamma_1 Ma^2} \frac{\partial p}{\partial z}. \quad (2.4)$$

Internal Energy equation, in terms of temperature

$$\rho \frac{\partial T}{\partial t} + \rho u \frac{\partial T}{\partial x} + \rho v \frac{\partial T}{\partial y} + \rho w \frac{\partial T}{\partial z} = -\frac{p(\gamma - 1)}{R} \left(\frac{\partial u}{\partial x} + \frac{\partial v}{\partial y} + \frac{\partial w}{\partial z} \right). \quad (2.5)$$

Mass fraction equation

$$\rho \frac{\partial S_1}{\partial t} + \rho u \frac{\partial S_1}{\partial x} + \rho v \frac{\partial S_1}{\partial y} + \rho w \frac{\partial S_1}{\partial z} = 0. \quad (2.6)$$

Equation of state for a perfect gas

$$p = \rho RT. \quad (2.7)$$

Gas constant

$$R = S_1 + (1 - S_1)R_{\text{ratio}}. \quad (2.8)$$

were

$$S_1 + S_2 = 1 \quad (2.9)$$

In the above equations ρ is the mixture density, u, v, w are the velocity components in the x, y, z , streamwise, normal and spanwise directions, γ is the ratio of heat capacity, Ma is the Mach number based on the inner stream velocity and speed of sound, p is the pressure, T is the temperature, R is the mixture gas constant, S_1 and S_2 are the mass fraction of species 1 and 2, and R_{ratio} is the gas constant ratio of the outer and inner streams.

2.1.1 Linear stability theory

In order to derive the stability equations the instantaneous flow variables are decomposed in a steady base flow and a disturbance,

$$\phi(x, y, z, t) = \bar{\phi}(y) + \phi'(x, y, z, t), \quad (2.10)$$

where the base flow has been assumed parallel. The base flow variables are defined as

$$\bar{\phi}(y) = [\bar{\rho}(y), (\bar{U}(y), 0, 0), \bar{P} = 1, \bar{T}(y), \bar{S}_1(y), \bar{R}(y)]^T. \quad (2.11)$$

And the disturbances as,

$$\phi'(x, y, z, t) = [\rho', u', v', w', p', T', S'_1, R']^T. \quad (2.12)$$

Substituting Equation (2.10) on the Euler equations and making a linearization, after some mathematical work, follows that

Continuity equation

$$\frac{\partial \rho'}{\partial t} + \bar{U} \frac{\partial \rho'}{\partial x} + \bar{\rho} \frac{\partial u'}{\partial x} + \bar{\rho} \frac{\partial v'}{\partial y} + \bar{\rho} \frac{\partial w'}{\partial z} + v' \frac{\partial \bar{\rho}}{\partial y} = 0. \quad (2.13)$$

Streamwise momentum equation

$$\bar{\rho} \frac{\partial u'}{\partial t} + \bar{\rho} \bar{U} \frac{\partial u'}{\partial x} + \bar{\rho} v' \frac{\partial \bar{U}}{\partial y} = -\frac{1}{\gamma_1 Ma^2} \frac{\partial p'}{\partial x}. \quad (2.14)$$

Normal momentum equation

$$\bar{\rho} \frac{\partial v'}{\partial t} + \bar{\rho} \bar{U} \frac{\partial v'}{\partial x} = -\frac{1}{\gamma_1 Ma^2} \frac{\partial p'}{\partial y} + \rho' g. \quad (2.15)$$

Spanwise momentum equation

$$\bar{\rho} \frac{\partial w'}{\partial t} + \bar{\rho} \bar{U} \frac{\partial w'}{\partial x} = -\frac{1}{\gamma_1 Ma^2} \frac{\partial p'}{\partial z}. \quad (2.16)$$

Energy equation

$$\bar{\rho} \frac{\partial T'}{\partial t} + \bar{\rho} \bar{U} \frac{\partial T'}{\partial x} + \bar{\rho} v' \frac{\partial \bar{T}}{\partial y} = -\frac{(\gamma-1)}{R} \frac{\partial u'}{\partial x} - \frac{(\gamma-1)}{R} \frac{\partial v'}{\partial y} - \frac{(\gamma-1)}{R} \frac{\partial w'}{\partial z}. \quad (2.17)$$

The energy equation may be further simplified multiplying equation (2.17) by R , assuming $R = \bar{R} + R'$ and keeping only the linear and parallel terms,

$$\bar{\rho} \frac{\partial T'}{\partial t} + \bar{\rho} \bar{U} \frac{\partial T'}{\partial x} + \bar{\rho} v' \frac{\partial \bar{T}}{\partial y} = -\frac{(\gamma-1)}{\bar{R}} \frac{\partial u'}{\partial x} - \frac{(\gamma-1)}{\bar{R}} \frac{\partial v'}{\partial y} - \frac{(\gamma-1)}{\bar{R}} \frac{\partial w'}{\partial z}. \quad (2.18)$$

Mass fraction equation

$$\bar{\rho} \frac{\partial S'_1}{\partial t} + \bar{\rho} \bar{U} \frac{\partial S'_1}{\partial x} + \bar{\rho} v' \frac{\partial \bar{S}_1}{\partial y} = 0. \quad (2.19)$$

Equation of state

$$p' = \bar{\rho}\bar{R}T' + \bar{\rho}R'\bar{T} + \rho'\bar{R}\bar{T}. \quad (2.20)$$

Solution for this set of equations may be sought by normal modes, assuming

$$\phi'(x, y, z, t) = \mathcal{R} \left\{ \hat{\phi}(y) \exp [i(\alpha x + \beta z - \omega t)] \right\}, \quad (2.21)$$

where $\hat{\phi}$ is a complex amplitude, $\alpha = \alpha_r + i\alpha_i$ where α_r is the streamwise wavenumber and α_i is the streamwise growth rate, β is the spanwise wavenumber and ω is the angular frequency.

Substituting the normal modes solution into the linearized Euler equations (Appendix A.2), results in:

Continuity equation

$$\hat{\rho}i(\alpha\bar{U} - \omega) + \hat{v}\frac{d\bar{\rho}}{dy} + \bar{\rho} \left[i(\alpha\hat{u} + \beta\hat{w}) + \frac{d\hat{v}}{dy} \right] = 0. \quad (2.22)$$

Streamwise momentum equation

$$\hat{u}i(\alpha\bar{U} - \omega) + \hat{v}\frac{d\bar{U}}{dy} + \frac{i\alpha\hat{p}}{\bar{\rho}\gamma_1 Ma^2} = 0. \quad (2.23)$$

Normal momentum equation

$$\hat{v}i(\alpha\bar{U} - \omega) + \frac{1}{\bar{\rho}\gamma_1 Ma^2} \frac{d\hat{p}}{dy} = 0. \quad (2.24)$$

Spanwise momentum equation

$$\hat{w}i(\alpha\bar{U} - \omega) + \frac{i\beta\hat{p}}{\bar{\rho}\gamma_1 Ma^2} = 0. \quad (2.25)$$

Energy equation

$$\hat{T}i(\alpha\bar{U} - \omega) + \hat{v}\frac{d\bar{T}}{dy} + \frac{(\gamma - 1)}{\bar{\rho}\bar{R}} \left[i(\alpha\hat{u} + \beta\hat{w}) + \frac{d\hat{v}}{dy} \right] = 0. \quad (2.26)$$

Mass fraction

$$\hat{S}_1 i (\alpha \bar{U} - \omega) + \hat{v} \frac{d\bar{S}_1}{dy} = 0. \quad (2.27)$$

Perfect Gas

$$p' = \bar{\rho} \bar{R} \hat{T} + \bar{\rho} \hat{R} \bar{T} + \hat{\rho} \bar{R} \bar{T}. \quad (2.28)$$

The gas constant for the mixture is

$$R = \hat{S}_1 (1 - R_{ratio}), \quad (2.29)$$

Such that, for the base flow and the disturbance

$$\bar{R} = \bar{S}_1 + (1 - \bar{S}_1) R_{ratio}, \quad (2.30)$$

$$R' = S'_1 + S'_1 R_{ratio}. \quad (2.31)$$

After some manipulation, it is possible to rewrite Equations (2.22), (2.23), (2.24), (2.25), (2.26), (2.27) and (2.28) into a system composed of two Eqs:

$$(\alpha \bar{U} - \omega) \frac{d\hat{v}}{dy} - \alpha \hat{v} \frac{d\bar{U}}{dy} = \frac{i\alpha^2 G \hat{p}}{\gamma_1 Ma^2}. \quad (2.32)$$

$$\hat{v} i (\alpha \bar{U} - \omega) = -\frac{1}{\bar{\rho} \gamma_1 Ma^2} \frac{d\hat{p}}{dy}.$$

where the last equation is the normal momentum equation, Equation (2.24).

Now, the new variable proposed by Gropengiesser (1970) is applied:

$$\chi = \frac{i\alpha \hat{p}}{\gamma Ma^2 \hat{v}}. \quad (2.33)$$

then applying Equations (2.32) and (2.24) into Equation (2.33), it is possible to write the following equation:

$$\frac{d\chi}{dy} = \frac{\alpha^2(\bar{U} - \omega/\alpha)}{R\bar{T}} - \chi \left[\frac{\chi G + (d\bar{U}/dy)}{(\bar{U} - \omega/\alpha)} \right], \quad (2.34)$$

where

$$G = \frac{\alpha^2 + \beta^2}{\bar{\rho}\alpha^2} - Ma_1^2 \frac{\gamma_1}{\gamma} \frac{(\alpha\bar{U} - \omega)^2}{\alpha^2}. \quad (2.35)$$

As described by (SANDHAM, 1990), the boundary conditions are derived accounting that for $y \rightarrow \pm\infty$ we have $\chi = \text{constant}$, $d\chi/dy = 0$, $d\bar{u}/dy = 0$ and $d\bar{\rho}/dy = 0$. Then:

$$\chi(y \rightarrow \pm\infty) = \pm \frac{\alpha(\bar{U} - \omega/\alpha)}{\sqrt{GR\bar{T}}}. \quad (2.36)$$

As it is known, the study of jet stability presents two different instability modes, a varicose and a sinuous one. The varicose mode has the characteristic that the disturbance v and its derivative v' go to zero at the centerline of the jet.

In order to capture the varicose mode, the inverse of the Gropengiesser transformation may be used to avoid singularities, then

$$\chi^I = \frac{\gamma Ma^2 \hat{v}}{i\alpha \hat{p}}. \quad (2.37)$$

such that

$$\frac{\gamma Ma^2 \hat{v}'}{i\alpha} = \chi^I \hat{p} + \chi^I \hat{p}'. \quad (2.38)$$

Replacing the new term in \hat{v} and \hat{p} the equations, with the new χ^I definition

$$\chi'^I = (\alpha g + aU' \chi^I) \frac{1}{\alpha U - \omega} - \rho\alpha(\alpha U - \omega)(\chi^I)^2. \quad (2.39)$$

2.1.2 Base flow

The present investigation considers simple planar jet and a co-planar jet. For the co-planar jet, a inner jet is surrounded by an outer jet symmetric with respect to

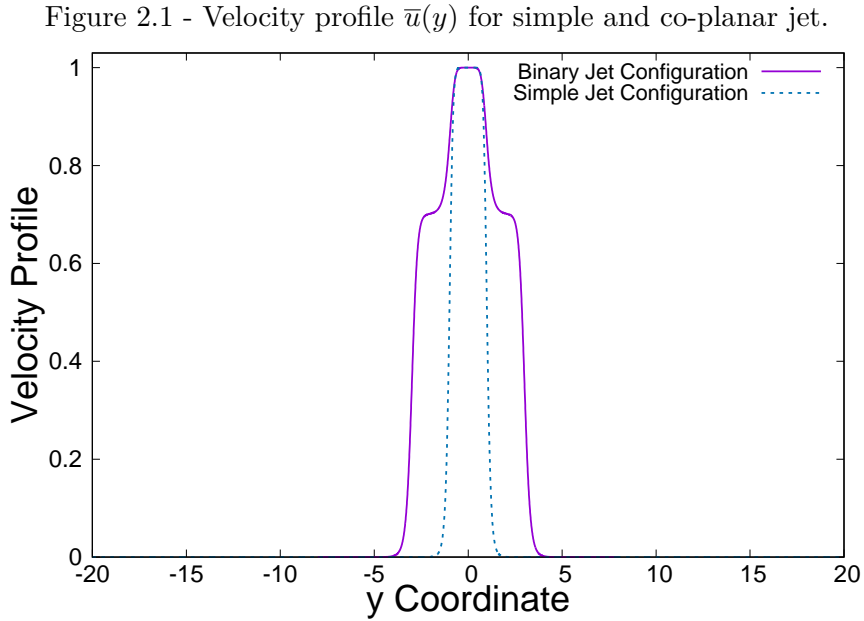
the inner jet centerline above and below.

The base flow appears in the equations due to decomposition of the flow variables into a base component plus a small oscillation. The present work use the same base flow velocity profile as Weder (2012), which was studied by Michalke (1984):

$$\bar{u}(y) = \lim_{\zeta \rightarrow y} \frac{1}{2} \left[1 + \tanh \frac{R_{1/2}}{4\theta} \left(\frac{R_{1/2}}{|\zeta|} - \frac{|\zeta|}{R_{1/2}} \right) \right]. \quad (2.40)$$

where $R_{1/2}$ is the jet half width and θ is the momentum boundary layer thickness.

For the co-planar jet the profile is also based on the above equation. The outer stream has speed equal to 0.7 of the inner jet. The velocity profiles can be seen in Figure 2.1.



The jet is assumed to be at a constant temperature. The pressure across the jet is assumed uniform. The chemical species at the inner jet is different from the surrounding ambient for simple jet. For the co-planar jet the inner and outer jets are streams of different chemical species and the outer jet is of the same chemical species as the ambient environment.

The values used in Equation (2.40), to generate Figure 2.1 are all taken from Weder

(2012). We use these values in order to replicate his results, so we are able to have a comparative case which we use to validate our numerical code.

2.1.2.1 Gas ratio (R_{ratio})

Considering the inner and outer jet streams at the same temperature and pressure of the quiescent ambient, through the equation of state a relation between the baseflow gas constant ratio R_{ratio} and the density ratio ρ_{ratio} , results

$$R_{ratio} = \frac{1}{\rho_{ratio}}. \quad (2.41)$$

such that, considering the inner jet as the reference state, $R_{ratio} > 1$ corresponds to $\rho_{ratio} < 1$, which corresponds to a heavy jet at the inner stream and $R_{ratio} < 1$ corresponds to $\rho_{ratio} > 1$ with light jet at the inner stream.

2.2 Parabolized stability equation

The flow configuration consists of a single jet issuing from a nozzle into a quiescent ambient. The jet velocity profile is presented in Figure 2.1.

The problem is formulated as a stability problem by reducing the compressible Navier-Stokes equations to the incompressible version of the parabolized stability equation. Starting with the dimensional Navier-Stokes equations in Cartesian coordinates for two-dimensional compressible flows of a binary mixture of two different gases, with reference values given by the jet at the center, the set of governing equations are:

$$\frac{\partial \rho^*}{\partial t^*} + \frac{\partial(\rho^* u_i^*)}{\partial x_i^*} = 0. \quad (2.42)$$

the momentum equation:

$$\rho^* \frac{\partial u_j^*}{\partial t^*} + \rho u_k^* \frac{\partial u_j^*}{\partial x_k^*} = \frac{\partial \sigma_{ij}^*}{\partial x_i} + \rho^* f_i^*. \quad (2.43)$$

where δ_{ij} is the Kronecker delta, λ is the bulk viscosity, μ^* is the dynamic viscosity, p^* is the pressure, ρ^* is the fluid density, t^* is the time and u_i^* , with $i = 1, 2$, is the velocity components. The momentum equation is in the non-conservative form.

The thermal energy equation is given by:

$$\begin{aligned} & \frac{\partial \rho e^*}{\partial t^*} + u_k^* \frac{\partial \rho e^*}{\partial x_k^*} = \\ -p \frac{\partial u_k^*}{\partial x_k} + \frac{\partial}{\partial x_k^*} \left(k^* \frac{\partial T^*}{\partial x_k^*} \right) + \lambda^* \left(\frac{\partial u_k^*}{\partial x_k^*} \right)^2 + \mu^* \frac{\partial u_j^*}{\partial x_i^*} \left(\frac{\partial u_i^*}{\partial x_j^*} + \frac{\partial u_j^*}{\partial x_i^*} \right). \end{aligned} \quad (2.44)$$

where e^* is the internal energy, k^* is the thermal conductivity and T^* is the temperature.

The species balance equation is given by:

$$\frac{\partial \rho^* S_n}{\partial t^*} + \frac{\partial}{\partial x_k^*} (\rho^* S_n u_k^*) = \frac{\partial}{\partial x_k^*} \left(\rho^* D^* \frac{\partial S_n}{\partial x_k^*} \right). \quad (2.45)$$

where D^* is the mass diffusivity and S_n mass fraction of the n species. The superscript $*$ indicates a dimensional property.

Considering a Newtonian fluid, the tensor is given by:

$$\sigma_{ij} = -p^* \delta_{ij} + \lambda \delta_{ij} \frac{\partial u_k^*}{\partial x_k^*} + \mu^* \left(\frac{\partial u_i^*}{\partial x_j^*} + \frac{\partial u_j^*}{\partial x_i^*} \right). \quad (2.46)$$

The enthalpy is introduced in the problem by the relation:

$$h^* = e^* + \frac{p^*}{\rho^*}, \quad (2.47)$$

it is implied that enthalpy is a temperature dependent property $h^* = h^*(T)$, then enthalpy is defined as:

$$h^* = \int_{T_0^*}^{T^*} h c_p^* dT, \quad (2.48)$$

the relation of bulk viscosity is given by Stokes hypothesis:

$$\lambda^* = -\frac{2}{3}\mu^*, \quad (2.49)$$

and the dimensional equation of state:

$$p^* = \rho^* R^* T^*. \quad (2.50)$$

2.2.1 Non-dimensional parameters

The nondimensionalization of the problem was made based on the boundary layer approximation. The non-dimensional variables are:

$$\begin{aligned} x &= \frac{x^*}{L^*}, & y &= \frac{y^*}{L^*}, & u &= \frac{u^*}{u_0^*}, \\ v &= \frac{v^*}{u_0^*}, & T &= \frac{T^*}{T_0^*}, & k &= \frac{k^*}{k_0^*}, \\ \mu &= \frac{\mu^*}{\mu_0^*}, & \rho &= \frac{\rho^*}{\rho_0^*}, & D &= \frac{D^*}{D_0^*}, \\ p &= \frac{p^*}{\rho_0^* u_0^{*2}}, & t &= \frac{t^*}{(L^*/u_0^*)}. \end{aligned} \quad (2.51)$$

2.2.2 Non-dimensional equations

Introducing the tensor definition (2.46), the enthalpy relation (2.47) and (2.48), the Stokes hypothesis (2.49) and the non-dimensional parameters (2.51) into Equations (2.42), (2.43), (2.44) and (2.45), the set of non-dimensional equations are obtained:

$$\frac{\partial \rho}{\partial t} + \frac{\partial \rho u}{\partial x} + \frac{\partial \rho v}{\partial y} = 0, \quad (2.52)$$

$$\begin{aligned} & \frac{\partial \rho u}{\partial t} + u \frac{\partial \rho u}{\partial x} + v \frac{\partial \rho u}{\partial y} = \\ & -\frac{\partial p}{\partial x} - \frac{2}{3} \frac{\mu}{Re} \frac{\partial}{\partial x} \left(\frac{\partial u}{\partial x} + \frac{\partial v}{\partial y} \right) + 2 \frac{\mu}{Re} \frac{\partial^2 u}{\partial x^2} + \frac{\mu}{Re} \frac{\partial}{\partial y} \left(\frac{\partial u}{\partial y} + \frac{\partial v}{\partial x} \right), \end{aligned} \quad (2.53)$$

$$\begin{aligned} \frac{\partial \rho v}{\partial t} + u \frac{\partial \rho v}{\partial x} + v \frac{\partial \rho v}{\partial y} = & \quad (2.54) \\ -\frac{\partial p}{\partial y} - \frac{2}{3} \frac{\mu}{Re} \frac{\partial}{\partial y} \left(\frac{\partial u}{\partial x} + \frac{\partial v}{\partial y} \right) + 2 \frac{\mu}{Re} \frac{\partial^2 v}{\partial y^2} + \frac{\mu}{Re} \frac{\partial}{\partial x} \left(\frac{\partial u}{\partial y} + \frac{\partial v}{\partial x} \right), \end{aligned}$$

where $Re = \rho^* u^* L^* / \mu^*$ is the Reynold's number. This non-dimensional number is the ratio of inertial forces do viscous forces in a moving fluid.

$$\begin{aligned} \frac{D(c_p \rho T)}{Dt} - \frac{Dp}{Dt} = & \quad (2.55) \\ -pEc \left(\frac{\partial u}{\partial x} + \frac{\partial v}{\partial y} \right) + \frac{1}{PrRe} \left[\frac{\partial}{\partial x} \left(k \frac{\partial T}{\partial x} \right) + \frac{\partial}{\partial y} \left(k \frac{\partial T}{\partial y} \right) \right] \\ - \frac{2}{3} \frac{Ec}{Re} \mu \left(\frac{\partial u}{\partial x} + \frac{\partial v}{\partial y} \right)^2 + \frac{Ec}{Re} \mu \left[\frac{\partial u}{\partial y} \left(\frac{\partial u}{\partial y} + \frac{\partial v}{\partial x} \right) + \frac{\partial v}{\partial x} \left(\frac{\partial v}{\partial x} + \frac{\partial u}{\partial y} \right) \right], \end{aligned}$$

$Ec = Ma^2(\gamma - 1) = u_0^{*2} / (hc_{p0}^* T_0^*)$ is the Eckert number, it is the ratio of advective transport to heat dissipation potential. $Pr = hc_{p0}^* \mu_0^* / k_0^*$ is the Prandtl number, it is the ratio of momentum diffusivity to thermal diffusivity. Mach number is defined as $Ma = u^* / u_{sound}^*$, where $u_{sound}^* = \sqrt{\gamma R_0^* T_0^*}$ is the speed of sound and $\gamma = hc_p^* / c_v^*$ is the heat capacity ratio. In Equation (2.55) some properties are expressed in terms of material derivative.

$$\frac{\partial \rho S_n}{\partial t} + u \frac{\partial \rho S_n}{\partial x} + v \frac{\partial \rho S_n}{\partial y} = \frac{1}{ReSc} \left[\frac{\partial}{\partial x} \left(\rho D \frac{\partial S_n}{\partial x} \right) + \frac{\partial}{\partial y} \left(\rho D \frac{\partial S_n}{\partial y} \right) \right], \quad (2.56)$$

$Sc = \mu_0^* / (\rho_0^* D_0^*)$ is the Schimidt number, it is the ratio of momentum diffusivity to mass diffusivity. This non-dimensional number relates to the Lewis Number ($Le = k_0^* / \rho_0^* D_n^* hc_{p0}^*$ - thermal diffusivity to mass diffusivity) by the expression $Le = Sc / Pr$.

Equations (2.52), (2.53), (2.54), (2.55) and (2.56) are the non-dimensional mass balance, momentum balance in the x coordinate, momentum balance in y coordinate, energy balance and species balance, respectively.

The non-dimensional equation of state is:

$$\frac{p}{\gamma Ma^2} = \rho RT. \quad (2.57)$$

2.2.3 Perturbation equations

The set of governing perturbation equations for the two dimensional jet are obtained by the decomposition of the dependent properties. The non-dimensional equations properties are split into a base flow component (mean component) denoted by an overline ($\bar{\phi}$), and a small amplitude perturbation denoted by an apostrophe (ϕ').

$$\phi = \bar{\phi} + \phi', \quad (2.58)$$

where $\phi = \{hc_p, D, k, \mu, p, \rho, T, u, v\}$

Applying Equation (2.58) into Equations (2.52), (2.53), (2.54), (2.55) and (2.56):

$$\frac{\partial}{\partial t} (\bar{p} + \rho') + \frac{\partial}{\partial x} [(\bar{p} + \rho')(\bar{u} + u')] + \frac{\partial}{\partial y} [(\bar{p} + \rho')(\bar{v} + v')] = 0, \quad (2.59)$$

$$\begin{aligned} \frac{\partial}{\partial t} [(\bar{p} + \rho')(\bar{u} + u')] + u \frac{\partial}{\partial x} [(\bar{p} + \rho')(\bar{u} + u')] + v \frac{\partial}{\partial y} [(\bar{p} + \rho')(\bar{u} + u')] = & \quad (2.60) \\ & - \frac{\partial}{\partial x} (\bar{p} + p') - \frac{2(\bar{\mu} + \mu')}{3 Re} \frac{\partial}{\partial x} \left(\frac{\partial}{\partial x} (\bar{u} + u') + \frac{\partial}{\partial y} (\bar{v} + v') \right) \\ & + 2 \frac{(\bar{\mu} + \mu')}{Re} \frac{\partial^2}{\partial x^2} (\bar{u} + u') + \frac{(\bar{\mu} + \mu')}{Re} \frac{\partial}{\partial y} \left(\frac{\partial}{\partial y} (\bar{u} + u') + \frac{\partial}{\partial x} (\bar{v} + v') \right), \end{aligned}$$

$$\begin{aligned} \frac{\partial}{\partial t} [(\bar{p} + \rho')(\bar{v} + v')] + u \frac{\partial}{\partial x} [(\bar{p} + \rho')(\bar{v} + v')] + v \frac{\partial}{\partial y} [(\bar{p} + \rho')(\bar{v} + v')] = & \quad (2.61) \\ & - \frac{\partial}{\partial y} (\bar{p} + p') - \frac{2(\bar{\mu} + \mu')}{3 Re} \frac{\partial}{\partial y} \left(\frac{\partial}{\partial x} (\bar{u} + u') + \frac{\partial}{\partial y} (\bar{v} + v') \right) \\ & + 2 \frac{(\bar{\mu} + \mu')}{Re} \frac{\partial^2}{\partial y^2} (\bar{v} + v') + \frac{(\bar{\mu} + \mu')}{Re} \frac{\partial}{\partial x} \left(\frac{\partial}{\partial y} (\bar{u} + u') + \frac{\partial}{\partial x} (\bar{v} + v') \right), \end{aligned}$$

$$\begin{aligned}
& \frac{\partial}{\partial t} [(\bar{\rho} + \rho')(\bar{c}_p + c'_p)(\bar{T} + T')] - \frac{\partial}{\partial t}(\bar{p} + p') \quad (2.62) \\
& + (\bar{u} + u') \frac{\partial}{\partial x} [(\bar{\rho} + \rho')(\bar{c}_p + c'_p)(\bar{T} + T')] \\
& + (\bar{v} + v') \frac{\partial}{\partial y} [(\bar{\rho} + \rho')(\bar{c}_p + c'_p)(\bar{T} + T')] \\
& - (\bar{u} + u') \frac{\partial}{\partial x}(\bar{p} + p') - (\bar{v} + v') \frac{\partial}{\partial y}(\bar{p} + p') = \\
& - (\bar{p} + p') Ec \left[\frac{\partial}{\partial x}(\bar{u} + u') + \frac{\partial}{\partial y}(\bar{v} + v') \right] \\
& + \frac{1}{PrRe} \left\{ \frac{\partial}{\partial x} \left[(\bar{k} + k') \frac{\partial}{\partial x}(\bar{T} + T') \right] + \frac{\partial}{\partial y} \left[(\bar{k} + k') \frac{\partial}{\partial y}(\bar{T} + T') \right] \right\} \\
& - \frac{2}{3} \frac{Ec}{Re} (\bar{\mu} + \mu') \left[\frac{\partial}{\partial x}(\bar{u} + u') + \frac{\partial}{\partial y}(\bar{v} + v') \right]^2 \\
& + \frac{Ec}{Re} (\bar{\mu} + \mu') \left\{ \frac{\partial}{\partial y}(\bar{u} + u') \left[\frac{\partial u}{\partial y}(\bar{u} + u') + \frac{\partial}{\partial x}(\bar{v} + v') \right] \right. \\
& \left. + \frac{\partial}{\partial x}(\bar{v} + v') \left[\frac{\partial}{\partial x}(\bar{v} + v') + \frac{\partial}{\partial y}(\bar{u} + u') \right] \right\},
\end{aligned}$$

$$\begin{aligned}
& \frac{\partial}{\partial t} [(\bar{\rho} + \rho')(\bar{S}_n + S'_n)] \quad (2.63) \\
& + (\bar{u} + u') \frac{\partial}{\partial x} [(\bar{\rho} + \rho')(\bar{S}_n + S'_n)] + (\bar{v} + v') \frac{\partial}{\partial y} [(\bar{\rho} + \rho')(\bar{S}_n + S'_n)] = \\
& \frac{1}{ReSc} \left\{ \frac{\partial}{\partial x} \left[(\bar{\rho} + \rho')(\bar{D} + D') \frac{\partial}{\partial x}(\bar{S}_n + S'_n) \right] \right. \\
& \left. + \frac{\partial}{\partial y} \left[(\bar{\rho} + \rho')(\bar{D} + D') \frac{\partial}{\partial y}(\bar{S}_n + S'_n) \right] \right\}.
\end{aligned}$$

In order to obtain the perturbation set of equations, the base equations, or in other words, the mean flow equations are subtracted from the decomposed set of equations and products of perturbation are neglected.

Subtracting Equation (2.52) from Equation (2.59):

$$\frac{\partial \rho}{\partial t} + u' \frac{\partial \bar{\rho}}{\partial x} + \bar{\rho} \frac{\partial u'}{\partial x} + \rho' \frac{\partial \bar{u}}{\partial x} + \bar{u} \frac{\partial \rho'}{\partial x} + v' \frac{\partial \bar{\rho}}{\partial x} + \bar{\rho} \frac{\partial v'}{\partial x} + \rho' \frac{\partial \bar{v}}{\partial x} + \bar{v} \frac{\partial \rho'}{\partial x} = 0. \quad (2.64)$$

Subtracting Equation (2.53) from Equation (2.60):

$$\begin{aligned}
& \frac{\partial}{\partial t}(\bar{\rho}u' + \rho'\bar{u}) + \bar{\rho}u \frac{\partial u'}{\partial x} + \frac{\partial \bar{u}}{\partial x}(\bar{\rho}u' + \rho'\bar{u}) \quad (2.65) \\
& \quad + \bar{\rho}v \frac{\partial u'}{\partial y} + \frac{\partial \bar{u}}{\partial y}(\bar{\rho}v' + \rho'\bar{v}) = \\
& \quad - \frac{\partial p'}{\partial x} - \frac{2}{3Re} \left\{ \mu' \frac{\partial}{\partial x} \left(\frac{\partial \bar{u}}{\partial x} + \frac{\partial \bar{v}}{\partial y} \right) + \bar{\mu} \frac{\partial}{\partial x} \left(\frac{\partial u'}{\partial x} + \frac{\partial v'}{\partial y} \right) \right\} \\
& + \frac{2}{Re} \left(\mu' \frac{\partial^2 \bar{u}}{\partial x^2} + \bar{\mu} \frac{\partial^2 u'}{\partial x^2} \right) + \frac{1}{Re} \left[\mu' \frac{\partial}{\partial y} \left(\frac{\partial \bar{v}}{\partial x} + \frac{\partial \bar{u}}{\partial y} \right) + \bar{\mu} \frac{\partial}{\partial y} \left(\frac{\partial v'}{\partial x} + \frac{\partial u'}{\partial y} \right) \right].
\end{aligned}$$

Subtracting Equation (2.54) from Equation (2.66):

$$\begin{aligned}
& \frac{\partial}{\partial t}(\bar{\rho}v' + \rho'\bar{v}) + \bar{\rho}v \frac{\partial v'}{\partial x} + \frac{\partial \bar{v}}{\partial x}(\bar{\rho}u' + \rho'\bar{u}) \quad (2.66) \\
& \quad + \bar{\rho}v \frac{\partial v'}{\partial y} + \frac{\partial \bar{v}}{\partial y}(\bar{\rho}v' + \rho'\bar{v}) = \\
& \quad - \frac{\partial p'}{\partial y} - \frac{2}{3Re} \left\{ \mu' \frac{\partial}{\partial y} \left(\frac{\partial \bar{u}}{\partial x} + \frac{\partial \bar{v}}{\partial y} \right) + \bar{\mu} \frac{\partial}{\partial y} \left(\frac{\partial u'}{\partial x} + \frac{\partial v'}{\partial y} \right) \right\} \\
& + \frac{2}{Re} \left(\mu' \frac{\partial^2 \bar{v}}{\partial y^2} + \bar{\mu} \frac{\partial^2 v'}{\partial y^2} \right) + \frac{1}{Re} \left[\mu' \frac{\partial}{\partial x} \left(\frac{\partial \bar{v}}{\partial x} + \frac{\partial \bar{u}}{\partial y} \right) + \bar{\mu} \frac{\partial}{\partial x} \left(\frac{\partial v'}{\partial x} + \frac{\partial u'}{\partial y} \right) \right].
\end{aligned}$$

Subtracting Equation (2.55) from Equation (2.67):

$$\begin{aligned}
& \frac{\partial}{\partial t} (\bar{T} \bar{\rho} c'_p + \bar{T} \rho' \bar{c}_p + T' \bar{\rho} \bar{c}_p) - \frac{\partial p'}{\partial t} + u' \frac{\partial}{\partial x} (\bar{T} \bar{\rho} \bar{c}_p) \quad (2.67) \\
& + \bar{u} \frac{\partial}{\partial x} (\bar{T} \bar{\rho} c'_p + \bar{T} \rho' \bar{c}_p + T' \bar{\rho} \bar{c}_p) + v' \frac{\partial}{\partial y} (\bar{T} \bar{\rho} \bar{c}_p) + \bar{v} \frac{\partial}{\partial y} (\bar{T} \bar{\rho} c'_p + \bar{T} \rho' \bar{c}_p + T' \bar{\rho} \bar{c}_p) \\
& + Ec \left[u' \frac{\partial \bar{p}}{\partial x} + \bar{u} \frac{\partial p'}{\partial x} + v' \frac{\partial \bar{p}}{\partial y} + \bar{v} \frac{\partial p'}{\partial y} - p' \left(\frac{\partial \bar{u}}{\partial x} + \frac{\partial \bar{v}}{\partial y} \right) - p' \left(\frac{\partial u'}{\partial x} + \frac{\partial v'}{\partial y} \right) \right] \\
& + \frac{1}{Pr Re} \left[\frac{\partial}{\partial x} \left(k' \frac{\partial \bar{T}}{\partial x} + \bar{k} \frac{\partial T'}{\partial x} \right) + \frac{\partial}{\partial y} \left(k' \frac{\partial \bar{T}}{\partial y} + \bar{k} \frac{\partial T'}{\partial y} \right) \right] \\
& - \frac{2 Ec}{3 Re} \left[\mu' \left(\frac{\partial \bar{u}}{\partial x} \right)^2 + \mu' \left(\frac{\partial \bar{v}}{\partial y} \right)^2 + 2\bar{\mu} \frac{\partial u'}{\partial x} \frac{\partial \bar{u}}{\partial x} + 2\bar{\mu} \frac{\partial v'}{\partial y} \frac{\partial \bar{v}}{\partial y} \right] \\
& - \frac{4 Ec}{3 Re} \left[\mu' \frac{\partial \bar{u}}{\partial x} \frac{\partial v'}{\partial y} + \bar{\mu} \left(\frac{\partial \bar{u}}{\partial x} \frac{\partial v'}{\partial y} + \frac{\partial \bar{v}}{\partial y} \frac{\partial u'}{\partial x} \right) \right] \\
& - \frac{Ec}{Re} \left[\mu' \left(\frac{\partial \bar{u}}{\partial y} \right)^2 + \mu' \left(\frac{\partial \bar{v}}{\partial x} \right)^2 + 2\bar{\mu} \frac{\partial u'}{\partial y} \frac{\partial \bar{u}}{\partial y} + 2\bar{\mu} \frac{\partial v'}{\partial x} \frac{\partial \bar{v}}{\partial x} \right].
\end{aligned}$$

Subtracting Equation (2.56) from Equation (2.68):

$$\begin{aligned}
& \frac{\partial}{\partial t} (\bar{\rho} S'_n + \bar{S}_n \rho') \quad (2.68) \\
& + \bar{\rho} u' \frac{\partial S'_n}{\partial x} + \frac{\partial \bar{S}_n}{\partial x} (\bar{\rho} u' + \rho' \bar{u}) + \bar{\rho} v' \frac{\partial S'_n}{\partial y} + \frac{\partial \bar{S}_n}{\partial y} (\bar{\rho} v' + \rho' \bar{v}) = \\
& \frac{1}{Re Sc} \left[\bar{\rho} \bar{D} \frac{\partial S'_n}{\partial x} + \frac{\partial \bar{S}_n}{\partial x} (\bar{\rho} \bar{D}' + \rho' \bar{D}) + \bar{\rho} \bar{D} \frac{\partial S'_n}{\partial y} + \frac{\partial \bar{S}_n}{\partial y} (\bar{\rho} \bar{D}' + \rho' \bar{D}) \right].
\end{aligned}$$

The boundary condition is given by:

$$u', v', T', S'_n, p' \longrightarrow 0 \quad \text{for } y = 0 \quad \text{and } y = \infty. \quad (2.69)$$

Equation (2.69) express the fact that away from the jet all fluctuations must decay to zero. It is also possible to define:

$$\frac{\partial u'}{\partial y}, \frac{\partial v'}{\partial y}, \frac{\partial T'}{\partial y}, \frac{\partial S'_n}{\partial y}, \frac{\partial p'}{\partial y} \longrightarrow 0 \quad \text{for } y = 0 \quad \text{and } y = \infty. \quad (2.70)$$

Decomposing the non-dimensional equation of state into a mean value plus a per-

turbation:

$$\frac{p'}{\gamma Ma^2} = \rho' \overline{RT} + \bar{\rho} R' \overline{T} + \bar{\rho} \overline{RT}', \quad (2.71)$$

R is the gas constant.

Variable dependent properties like hc'_p, k', μ and R' should be linearized by use of Taylor's series expansion as demonstrated in Appendix Equations (A.43) and (A.44). Considering properties only dependent of the species considered and from now on assuming constant properties ($\phi' = 0$, where $\phi' = \{hc'_p, D', \mu', \rho'\}$) and homogeneous flow, it is possible to rewrite the equations.

Applying the simplification into Equation (2.64)

$$\frac{\partial u'}{\partial x} + \frac{\partial v'}{\partial x} = 0. \quad (2.72)$$

Equation (2.65) becomes

$$\begin{aligned} & \bar{\rho} \frac{\partial u'}{\partial t} + \bar{\rho} \bar{u} \frac{\partial u'}{\partial x} + \bar{\rho} u' \frac{\partial \bar{u}}{\partial x} + \bar{\rho} \bar{v} \frac{\partial u'}{\partial y} + \bar{\rho} v' \frac{\partial \bar{u}}{\partial y} = \\ & - \frac{\partial p'}{\partial x} - \frac{2\bar{\mu}}{3Re} \frac{\partial}{\partial x} \left(\frac{\partial u'}{\partial x} + \frac{\partial v'}{\partial y} \right) + \frac{2\bar{\mu}}{Re} \frac{\partial^2 u'}{\partial x^2} + \frac{\bar{\mu}}{Re} \frac{\partial}{\partial y} \left(\frac{\partial v'}{\partial x} + \frac{\partial u'}{\partial y} \right). \end{aligned} \quad (2.73)$$

Equation (2.66) becomes

$$\begin{aligned} & \bar{\rho} \frac{\partial v'}{\partial t} + \bar{\rho} \bar{u} \frac{\partial v'}{\partial x} + \bar{\rho} u' \frac{\partial \bar{v}}{\partial x} + \bar{\rho} \bar{v} \frac{\partial v'}{\partial y} + \bar{\rho} v' \frac{\partial \bar{v}}{\partial y} = \\ & - \frac{\partial p'}{\partial y} - \frac{2\bar{\mu}}{3Re} \frac{\partial}{\partial y} \left(\frac{\partial u'}{\partial x} + \frac{\partial v'}{\partial y} \right) + \frac{2\bar{\mu}}{Re} \frac{\partial^2 v'}{\partial y^2} + \frac{\bar{\mu}}{Re} \frac{\partial}{\partial x} \left(\frac{\partial v'}{\partial x} + \frac{\partial u'}{\partial y} \right). \end{aligned} \quad (2.74)$$

Equation (2.67) becomes

$$\begin{aligned}
& \bar{\rho} \bar{c}_p \frac{\partial T'}{\partial t} - \frac{\partial p'}{\partial t} + \bar{\rho} \bar{c}_p u' \frac{\partial \bar{T}}{\partial x} + \bar{\rho} \bar{c}_p \bar{u} \frac{\partial T'}{\partial x} + v' \frac{\partial}{\partial y} (\bar{T} \bar{\rho} \bar{c}_p) + \bar{\rho} \bar{c}_p \bar{v} \frac{\partial T'}{\partial y} = \quad (2.75) \\
& + Ec \left[u' \frac{\partial \bar{p}}{\partial x} + \bar{u} \frac{\partial p'}{\partial x} + v' \frac{\partial \bar{p}}{\partial y} + \bar{v} \frac{\partial p'}{\partial y} - p' \left(\frac{\partial \bar{u}}{\partial x} + \frac{\partial \bar{v}}{\partial y} \right) - p' \left(\frac{\partial u'}{\partial x} + \frac{\partial v'}{\partial y} \right) \right] \\
& \quad + \frac{\bar{k}}{Pr Re} \left[\frac{\partial^2 T'}{\partial x^2} + \frac{\partial^2 T'}{\partial y^2} \right] - \frac{2 Ec}{3 Re} \left[2\bar{\mu} \frac{\partial u'}{\partial x} \frac{\partial \bar{u}}{\partial x} + 2\bar{\mu} \frac{\partial v'}{\partial y} \frac{\partial \bar{v}}{\partial y} \right] \\
& \quad - \frac{4 Ec}{3 Re} \left[\bar{\mu} \left(\frac{\partial \bar{u}}{\partial x} \frac{\partial v'}{\partial y} + \frac{\partial \bar{v}}{\partial y} \frac{\partial u'}{\partial x} \right) \right] - \frac{Ec}{Re} \left[2\bar{\mu} \frac{\partial u'}{\partial y} \frac{\partial \bar{u}}{\partial y} + 2\bar{\mu} \frac{\partial v'}{\partial x} \frac{\partial \bar{v}}{\partial x} \right].
\end{aligned}$$

Equation (2.68) becomes

$$\frac{\partial S'_n}{\partial t} + \bar{\rho} \bar{u} \frac{\partial S'_n}{\partial x} + \bar{\rho} u' \frac{\partial \bar{S}_n}{\partial x} + \bar{\rho} \bar{v} \frac{\partial S'_n}{\partial y} + \bar{\rho} v' \frac{\partial \bar{S}_n}{\partial y} = \frac{1}{Re Sc} \left[\bar{\rho} \bar{D} \frac{\partial S'_n}{\partial x} + \bar{\rho} \bar{D} \frac{\partial S'_n}{\partial y} \right]. \quad (2.76)$$

The equation of state is simplified to

$$p' = T' \gamma Ma^2. \quad (2.77)$$

The mean flow properties are given in the following section.

2.2.4 Properties of mixtures

Variable properties will be employed to describe the behavior of binary gases. The use of variable properties is reinforced by [Shin e Freziger \(1991\)](#), whose work demonstrates a super estimation in the results of spatial growth rate of a mixing layer using constant properties. [Kozusko et al. \(1996a\)](#) work pointed out the dependence of the base flow solution of binary mixing flow on the fluid properties. Also, [Fedioun e Lardjane \(2005\)](#) presented differences on the stability characteristics of the problem due to the presence of different gases in the mixing layer.

2.2.4.1 Density

To calculate the density of an individual gas was introduced by [Clapeyron \(1834\)](#)

$$\rho^* = \frac{p^*}{R^* T^*}, \quad (2.78)$$

where p^* is the pressure in $[Pa]$, ρ^* is the fluid density $[kg/m^3]$, R^* is the gas constant $[J/(kg K)]$ and T^* is the fluid temperature $[K]$. The density of a mixture of gases would be obtained from the total mass of the gases, which is the sum of the masses of each.

$$\rho_{mix}^* = \sum_n \rho_n(p^*, T, R^*). \quad (2.79)$$

2.2.4.2 Gas constant

The gas constant of individual species is given by

$$R^* = \frac{R_U^*}{M^*}, \quad (2.80)$$

where R_U^* is the universal gas constant $kJ/(kmolK)$ and M^* is the gas mass $[kg/(kmol)]$.

For a mixture the gas constant is given by

$$R_{mix}^* = \sum_n R_n^* S_n, \quad (2.81)$$

where S_n is the mass fraction of the gas n and it is dimensionless.

2.2.4.3 Heat capacity

The polynomial expression to calculate the heat capacity of a single gas is given by

$$\frac{hc_p^*}{R^*} = a_1 + a_2 T^* + a_3 T^{*2} + a_4 T^{*3} + a_5 T^{*4}, \quad (2.82)$$

where a_1, a_2, a_3, a_4 and a_5 is given by [Mcbride et al. \(1993\)](#).

Considering a mixture of gases, the heat capacity of the mixture is given by

$$hc_{p,mix}^* = \sum_n c_{p,n}^* S_n, \quad (2.83)$$

The heat capacity is in $[kJ/(kg K)]$ (TEJA, 1983).

2.2.4.4 Mass diffusivity

The mass diffusivity used here will be function of only species concentration gradients. Effects like Soret and Dufour are small and will be neglected (SALEMI, 2006).

The theoretical equation for mass diffusivity comes from the solving of the Boltzmann equation by Chapman and Enskog

$$D_{ab} = \frac{0.00266T^{*2/3}}{p^*M_{ab}^{*1/2}\sigma_{ab}^{*2}\Omega_d}, \quad (2.84)$$

where D_{ab} is the diffusion coefficient $[cm^2/s]$, Ω_d is the diffusion collision integral [non-dimensional], p^* is the pressure $[bar]$, σ_{ab}^* is the characteristic length $[\text{\AA}]$ and T^* the temperature $[K]$.

The use of Equation (2.84) needs the interaction value σ_{ab} from σ_a and σ_b . The diffusion collision integral Ω_d is a function of $k^*T^*/\varepsilon_{ab}^*$, where ε^* and σ^* are the characteristics Lennard-Jones energy and length, respectively. A relation is needed for ε_{ab} (POLING et al., 2001).

$$\varepsilon_{ab} = (\varepsilon_a^* + \varepsilon_b^*)^{\frac{1}{2}}, \quad (2.85)$$

$$\sigma_{ab}^* = \frac{\sigma_a^* + \sigma_b^*}{2}, \quad (2.86)$$

Ω_d is tabulated for the 12-6 Lennard-Jones potential (HIRSCHFELDER et al., 1955). The Neufeld et al. (1972) relation is

$$\Omega_d = \frac{A}{T_h^B} + \frac{C}{\exp(DT_h)} + \frac{E}{\exp(FT_h)} + \frac{G}{\exp(HT_h)}, \quad (2.87)$$

where $T_h = k^*T^*/\varepsilon^*$ and the coefficients $A, B, C, D, E, F,$ and H are given (POLING et al., 2001).

2.2.4.5 Thermal conductivity

The thermal conductivity equation is given by least squares fit to the following equation

$$\log(k^*) = A_k \log(T^*) + \frac{B_k}{T^*} + \frac{C_k}{T^{*2}} + D_k, \quad (2.88)$$

where k^* is the thermal conductivity [$\mu W/cm K$], T^* is the temperature in [K] and the constants A_k , B_k , C_k and D_k are obtained by data fitting (SVEHLA, 1995).

Following Salemi (2006)'s work, the thermal conductivity of binary mixtures is given by Wassiljewa (REID et al., 1977)

$$k_{mix}^* = \frac{X_a k_a^*}{X_a + X_b \Gamma_{ab}} + \frac{X_b k_b^*}{X_b + X_a \Gamma_{ba}}, \quad (2.89)$$

where k_{mix} is the thermal conductivity of the mixture [$W/(m K)$]. X_a and X_b are the non-dimensional parameters known as molar fraction of gas a and b , respectively. Γ_{ab} and Γ_{ba} are also dimensionless parameters provided by Mason and Saxena (REID et al., 1977). Combining Equation (2.89) with Mason and Saxena parameters

$$\Gamma_{ab} = \frac{\left[1 + \left(\frac{k_a^*}{k_b^*} \right)^{1/2} \left(\frac{M_{ob}}{M_{oa}} \right)^{1/4} \right]^2}{\left[8 \left(1 + \frac{M_a}{M_b} \right) \right]^{1/2}}, \quad (2.90)$$

$$\Gamma_{ba} = \Gamma_{ab} \frac{k_b^* M_{oa}}{k_a^* M_{ob}}, \quad (2.91)$$

where the parameters M_{oa} and M_{ob} are the molar masses of gases a and b respectively [$kg/kmol$].

2.2.4.6 Viscosity

The fluid viscosity is given by

$$\log(\mu^*) = A_\mu \log(T^*) + \frac{B_\mu}{T^*} + \frac{C_\mu}{T^{*2}} + D_\mu, \quad (2.92)$$

the constants A_μ , B_μ , C_μ and D_μ are fitted data. The viscosity μ^* is given in [$\mu g/cm/s$] and the temperature T^* in [K].

In order to calculate the viscosity of the binary fluid, the extended Chapman-Enskog theory is needed, because it is generally non-linear.

$$\mu_{mix} = \frac{X_a \mu_a^*}{X_a + X_b \Phi_{ab}} + \frac{X_b \mu_b^*}{X_b + X_a \Phi_{ba}}, \quad (2.93)$$

μ_{mix} is the mixture viscosity and its unity will be the same of the inputs μ_a^* and μ_b^* . Φ_{ab} and Φ_{ba} are dimensionless parameter provided by Wilke, utilizing Sutherland theory (REID et al., 1977).

$$\Phi_{ab} = \frac{\left[1 + \left(\frac{\mu_a^*}{\mu_b^*} \right)^{1/2} \left(\frac{Mo_b}{Mo_a} \right)^{1/4} \right]^2}{\left[8 \left(1 + \frac{Mo_a}{Mo_b} \right) \right]^{1/2}}, \quad (2.94)$$

$$\Phi_{ba} = \Phi_{ab} \frac{\mu_b^* Mo_a}{\mu_a^* Mo_b}. \quad (2.95)$$

2.2.5 Linearized PSE for incompressible flow

Now with the complete set of perturbation equations it is possible to modify those equations leading to the set of parabolized stability equations (PSE). These equations describe the spatial evolution of the disturbances, allowing the observation of non-linear and non-parallel effects, which is impossible when using linear stability theory. The PSE has another advantage, running a simulation requires very low computational processing. Its low computational coast, makes possible to obtain a large range of results, more complex than LST, without the need of running a direct simulation (DNS), which needs a very potent computer and can take up to several hours to complete.

The governing equations can be simplified, due to its wavelike nature, by rewriting them as a function of their frequency ω , wavenumber α and growth rate γ . It is possible by assuming that any perturbation $\phi' = (u', v', T', S'_n, p')^T$ is composed of a slowly varying function and an exponential oscillatory term. For linear problems ϕ' is mathematically given as a Fourier expression truncated to a finite number of modes:

$$\phi'(x, y, t) = \hat{\phi}(x, y)\chi(x, t) + c.c., \quad (2.96)$$

where $\phi' = (u', v', T', S'_n, p')^T$ is the perturbation vector, $\hat{\phi} = (\hat{u}, \hat{v}, \hat{T}, \hat{S}_n, \hat{p})^T$ is the shape function and $c.c.$ is the complex conjugate. If the complex conjugate is not used, an imaginary number will be representing a physical property, which does not match reality. After adding the complex conjugate the imaginary part disappears.

$$\chi(x, t) = \exp\left(\int_{x_0}^x a(\xi)d\xi - i\omega t\right), \quad (2.97)$$

χ is the function which models the wavelike behavior of the wave.

$$a(x) = \Gamma + i\alpha(x), \quad (2.98)$$

α is the wavenumber, a is the complex exponent composed of the growth rate and the streamwise wavenumber. For a linear problem like this one, only the fundamental mode is relevant. If the problem become more complex, that is, if it start including non-linear terms, it would be necessary to consider higher harmonics. It would be made by increasing the number of modes in the truncated Fourier expansion.

Equation (2.96) is introduced into Equations (2.72), (2.73), (2.74), (2.75) and (2.76). The assumption that shape function, wavelength and growth rate vary slowly in the streamwise direction is made. Second derivatives like $\partial^2\hat{\phi}/\partial x^2$, $\partial^2 a/\partial x^2$ and products between derivatives da/dx and $\partial\hat{\phi}/\partial x$ are neglected.

Partial derivatives of perturbation ϕ' are presented in Appendix Equations (A.49), (A.50), (A.51), (A.52), (A.53), (A.54) and (A.55). After some mathematical manipulation is possible to rewrite the PSE equations

The final set of equations utilized in PSE are the Equation (A.56), (A.58), (A.60), (A.61) and (A.62).

2.2.6 Discretization

In this section, the approximations used to transform our continuous equations in their discrete counterparts are presented. Our set of partial differential equations are to be solved implicitly by using second order backward differentiation in the

streamwise direction, and fourth order centered differentiation in the normal direction. Second order centered differentiation is used in the first points near the boundary.

First order backward differentiation is used in the first steps of the simulation

$$\frac{\partial\phi}{\partial x} = \frac{\phi_j^{i+1} - \phi_j^i}{\Delta x}, \quad (2.99)$$

First order centered differentiation is used in the first points near to the normal boundary conditions ($j = 2$ and $j = j_{max} - 1$):

$$\frac{\partial\phi}{\partial y} = \frac{\phi_{j+1}^{i+1} - \phi_{j-1}^{i+1}}{2\Delta x}, \quad (2.100)$$

In the streamwise direction implicit second order backward differencing is discretized as

$$\frac{\partial\phi}{\partial x} = \frac{3\phi_j^{i+1} - 4\phi_j^i + \phi_j^{i-1}}{2\Delta x}, \quad (2.101)$$

Then in every other point ($2 < j < j_{max} - 1$) in the normal coordinate, fourth order approximation is employed

$$\frac{\partial\phi}{\partial y} = \frac{1}{12\Delta y}(\phi_{j-2}^{i+1} - 8\phi_{j-1}^{i+1} + 8\phi_{j+1}^{i+1} - \phi_{j+2}^{i+1}), \quad (2.102)$$

$$\frac{\partial^2\phi}{\partial y^2} = \frac{1}{12\Delta y}(-\phi_{j-2}^{i+1} + 16\phi_{j-1}^{i+1} - 30\phi_j^{i+1} + 16\phi_{j+1}^{i+1} - \phi_{j+2}^{i+1}), \quad (2.103)$$

The discretization is applied to the partial differential Equations (A.56), (A.58), (A.60), (A.61) and (A.62). Rearranging them in terms of i and j

$$A_m\phi_{j-2}^{i+1} + B_m\phi_{j-2}^{i+1} + C_m\phi_j^{i+1} + D_m\phi_{j+1}^{i+1} + D_m\phi_{j+2}^{i+1} = R_m, \quad (2.104)$$

the matrices A_m , B_m , C_m , D_m , E_m and R_m ($m = 1, \dots, 5$) are given in appendix A.6.

2.3 Numerical method

2.3.1 LST

The problem posed by the Rayleigh equation, written in terms of the Gropengieser variable, and the corresponding boundary conditions away from the shear layer, are an eigenvalue problem in terms of α , β , ω , Ma and the gas constant ratio between the two gases R_{ratio} . Solution is found only for certain combination of eigenvalues. Since the stability equation does not have an analytical closed form solution, numerical methods must be used to solve the problem. In this work the equation is solved using a shooting method, where the equation are integrated from the two boundaries to the center at $y = 0$ for a given initial guess for the complex wavenumber α , and specified frequency ω , spanwise wavenumber β , Mach number Ma and gas constant ratio R_{ratio} . If the guessed wavenumber is incorrect the solutions coming from above and below $y = 0$ will not match and the value of α has to be corrected using a root finding algorithm such as the secant method. To integrate the differential equation from the boundaries towards the center a fourth order Runge-Kutta method is used.

2.3.2 PSE

The system of equations obtained is parabolic. In order to solve it, a numerical method based on finite differences was used, providing a discrete solution for each point on the mesh (i, j) . The discretization of the partial differential equations was done implicitly by use of a second order backward differentiation in the streamwise direction, and fourth order centered differentiation in the normal direction. The resultant coupled algebraic equations are given by a pentadiagonal system which was solved by LU decomposition. The first steps of the computation were made by using first order backward differentiation. This approximation was used in subsequent steps downstream in order to dump transient effects. For the points in the vicinity of the boundaries, second order central differences was applied. The numerical method utilized in this work is the same used by Mendonça (1997).

2.3.2.1 Normalization condition

The split of the perturbation $\phi'(x, y, t)$ into two functions $\hat{\phi}(x, y)$ and $\chi(x, t)$ is ambiguous, because both functions are dependent on the streamwise coordinate x . Therefore, it is necessary to assign how much variation will be represented by the shape function $\hat{\phi}(x, y)$, and how much variation will be represented by the exponential function $\chi(x, t)$. By defining that, it is possible to assure that rapid variations

in the x coordinate (streamwise direction) are prevented, ensuring that the hypothesis of slowly changing variables is maintained. The objective is to transfer all the fast variations of the shape function in the streamwise direction to the streamwise complex wavenumber $a = \Gamma + i\alpha(x)$. If the rapid variation is represented by b , then for each step in the streamwise direction it is necessary to iterate $a(x)$ until b to be smaller than a given value. For each step/iteration k , the wavenumber is updated according to:

$$a_{k+1} = a_k + b_k, \quad (2.105)$$

The updating of b of the shape function can be monitored in several different ways, for example:

$$\begin{aligned} b &= \frac{\partial u_{y_{max}}}{\partial x}, \\ b &= \int_0^\infty \left(u^\dagger \frac{\partial u}{\partial x} \right) dy, \\ b &= \int_0^\infty \frac{\partial \|\vec{u}\|^2}{\partial x} dy, \end{aligned} \quad (2.106)$$

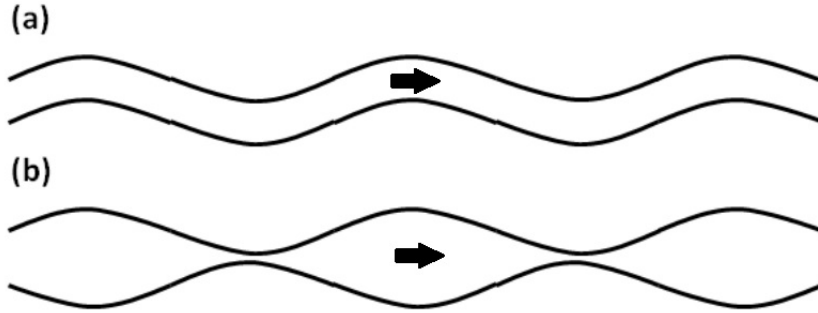
$u_{y_{max}}$ is the value of u at y location where amplitude has maximum value, u^\dagger is the complex conjugate of u and $\|\vec{u}\|^2$ is a measure of energy of perturbation velocity vector.

The limitation of variation of the shape function is known as normalization condition. The choosing of a fit normalization condition may vary slightly the resulting shape function and complex wavenumber, but the disturbances variation travelling downstream are not affected (MENDONÇA, 1997).

3 RESULTS

In this chapter results are shown for both LST and PSE. In the first part Linear Stability Theory results are presented and in the the second part Parabolized Stability Equations results are displayed. LST is further divided in two parts: simple jet and co-planar jet, and each of these new parts are further subdivided in sinuous and varicose modes. Characterization of sinuous and varicose modes are given by $\hat{p}(0) = 0$ and $\hat{v}(0) = 0$, respectively. The structure of sinuous and varicose fluid flows can be seen in Figure 3.1.

Figure 3.1 - (a) Sinuous and (b) varicose fluid topology



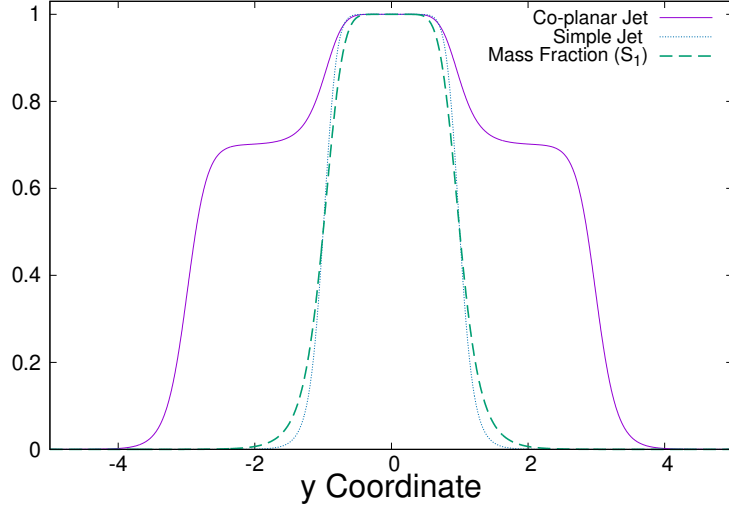
in Figure 3.2 mass fraction profile is displayed with both Simple and co-planar jet profiles.

The PSE results are shown for the simple jet configuration only. The velocity profile when mentioning simple and co-planar jets can be seen in Figure 2.1.

The LST development is made in order to calculate a compressible fluid flow. The PSE utilizes the compressible initial conditions obtained from LST, however PSE calculation is incompressible. After the the results section, a chapter is dedicated to the conclusions, followed by a section discussing future works. The max velocity of the central jet is fixed for $Ma = 0.9$ for all cases, in order to replicate Weder (2012) results. This assumption, allows us to compare and validate our numerical code.

An important observation is that, our results are presented as function of the gas ratio $R_{\text{ratio}} = \frac{1}{\rho_{\text{ratio}}}$, such that, considering the inner jet as the reference state, $R_{\text{ratio}} > 1$ corresponds to $\rho_{\text{ratio}} < 1$, which corresponds to a heavy jet at the inner stream and $R_{\text{ratio}} < 1$ corresponds to $\rho_{\text{ratio}} > 1$ with light jet at the inner stream.

Figure 3.2 - Mass fraction, simple and co-planar jet profiles as a function of y coordinate.



3.1 LST

To investigate the spatial stability of the simple jet and co-planar jet configurations, solutions for the dispersion relation $D(R_{\text{ratio}}, Ma, \alpha, \omega) = 0$ are sought. The real part of the eigenvalue α_r is the streamwise wave number and α_i is the streamwise spatial growth rate or amplification rate. The gas constant ratios considered for both simple and co-planar jets are $R_{\text{ratio}} = 0.125; 0.25; 0.5; 1.0; 2.0; 4.0; 8.0$. The inner jet Mach number is kept constant and equal to $Ma = 0.9$.

Results are presented in terms of phase speeds $cp = \omega/\alpha_r$, wavenumbers α_r , growth rates α_i , flow structure given by the vorticity fields and eigenfunctions \hat{p} , \hat{v} and \hat{u} .

The vorticity field is given by

$$\eta = \frac{\partial u'}{\partial y} - \frac{\partial v'}{\partial x}. \quad (3.1)$$

3.1.1 Simple jet

This section investigates the spatial stability of a single stream, plane jet flow given in Figure 2.1. The growth rates α_i corresponding to the fastest growing modes are numerically given in Table 3.1 for each gas ratio R_{ratio} , along with the corresponding angular frequency ω , streamwise wavenumber α_r and phase speed cp . For both the sinuous and varicose modes the frequency and phase velocity corresponding to the

fastest growing mode increase continuously with increasing gas ratio.

Table 3.1 - Largest spatial growth rate α_i and corresponding angular frequency ω , wavenumber α_r and phase speed cp for the simple jet.

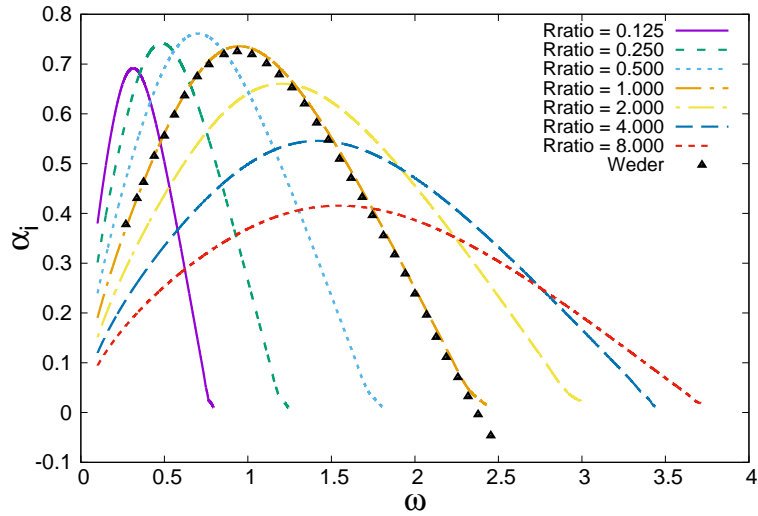
	R_{ratio}	ω	α_r	α_i	cp
Sinuous	0.125	0.313	1.231	0.692	0.254
	0.250	0.483	1.457	0.742	0.332
	0.500	0.670	1.666	0.761	0.420
	1.000	0.949	1.839	0.736	0.516
	2.000	1.202	1.954	0.660	0.615
	4.000	1.418	1.997	0.546	0.709
	8.000	1.547	1.959	0.416	0.789
Varicose	0.125	0.360	1.124	0.616	0.320
	0.250	0.516	1.349	0.731	0.383
	0.500	0.717	1.565	0.770	0.458
	1.000	0.960	1.758	0.743	0.546
	2.000	1.230	1.927	0.659	0.638
	4.000	1.488	2.050	0.532	0.726
	8.000	1.690	2.110	0.391	0.801

3.1.1.1 Results for the sinuous mode

Figures 3.3, 3.4 and 3.5 shows growth rate α_i , streamwise wavenumber α_r and phase speed c_p , as a function of the angular frequency ω for different gas ratios R_{ratio} for the sinuous case. Comparisons with results from Weder (2012) are presented in Figures 3.3 and 3.4. These comparisons serve as validation for the stability code used in this investigation. Results obtained from our numerical code are compared with his results, for the case considering gas ratio $R_{\text{ratio}} = 1$ and Mach number $Ma = 0.9$. In Weder (2012) the case for which the comparison is made is equivalent to a Reynold's number of $Re = 10^3$, however considering present stability analysis, which is inviscid, this value is not used. The Reynolds number is high enough so that viscous effects in the stability results are not relevant. Comparison with the Weder (2012) results are made for the spanwise wavenumber and growth rates.

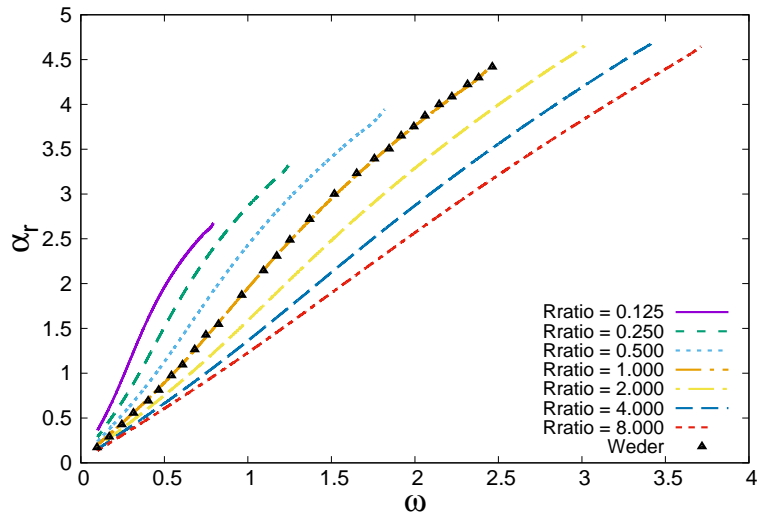
In Figure 3.3, for gas ratios of $R_{\text{ratio}} = 0.125; 0.25; 0.5, 1.0$ the largest amplification rate α_i appears not to have significant variations for gas ratios $R_{\text{ratio}} < 1$, having its highest value at $R_{\text{ratio}} = 0.5$. For gas ratios $R_{\text{ratio}} = 2.0, 4.0; 8.0$ the maximum amplification rate decrease significantly. It is important to highlight that besides the fact that the maximum amplification rate α_i is lower at higher gas ratios R_{ratio} ,

Figure 3.3 - Sinuous mode spatial amplification rate α_i as a function of angular frequency ω for different gas ratios. Mach number = 0.9. Simple jet configuration.



the range of frequencies ω in which the flow can become unstable is much wider in those gas ratios $R_{ratio} > 1$ values.

Figure 3.4 - Sinuous mode streamwise wavenumber α_r as a function of angular frequency ω for different gas ratios. Mach number = 0.9. Simple jet configuration.



In Figure 3.4, the wavenumber α_r is presented as a function of angular frequency ω , and the disturbance appear to be less dispersive by increasing the gas ratio R_{ratio} . However the wavenumber is not an optimal parameter to identify dispersion. A

better representation of dispersion can be seen in Figure 3.5 .

Figure 3.5 - Sinuous mode phase velocity cp as a function of angular frequency ω for different gas ratios. Mach number = 0.9. Simple jet configuration.

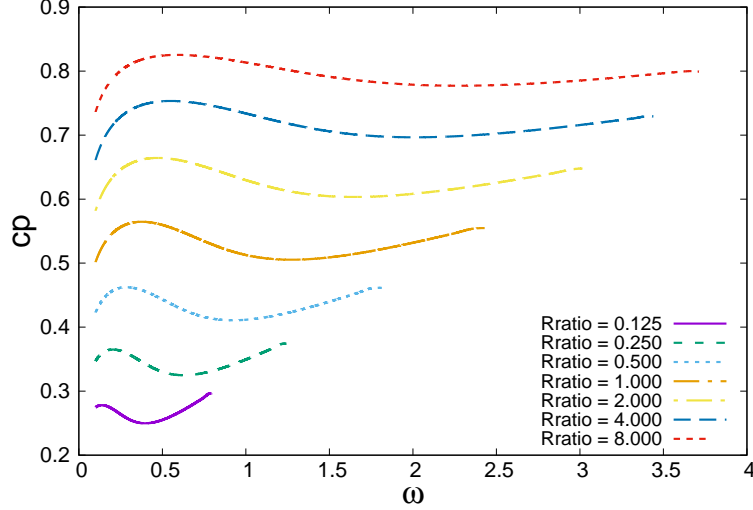
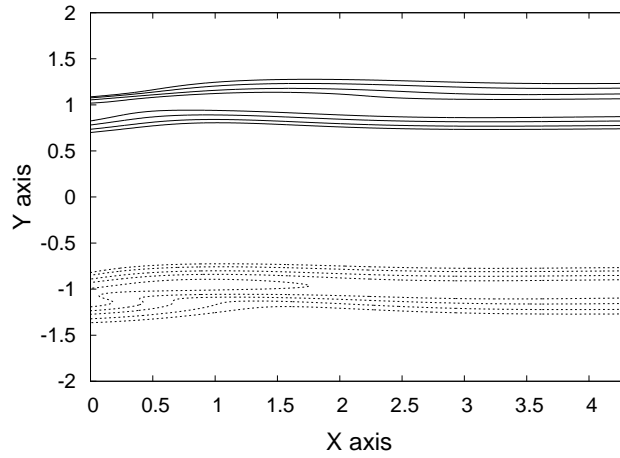


Figure 3.5 shows the phase velocity cp as a function of frequency ω . The phase velocity, shows us the velocity that perturbations are traveling in the flow. If a group of perturbation travels with same velocity for any frequency ω , after some displacement downstream, these perturbations should present the same configuration as before, because they travel together with same speed. This case would be represented in our Figure 3.5 as a horizontal flat line. As the perturbation start traveling at different velocities for different frequencies, the case is considered more dispersive. In Figure 3.5, it is possible to see that increasing the gas ratio, that is, increasing the density of the inner jet, results in less dispersive disturbances and higher phase speeds. The phase speed drops from around 80% of the jet centerline velocity for $R_{ratio} = 8$ to less than 30% for $R_{ratio} = 0.125$. Knowing that the density ratio is proportional to the inverse of the gas constant ratio, the disturbances travel much slower when the lighter fluid is in the jet and the heavier fluid is the ambient fluid.

Figures 3.6, 3.8 and 3.8 shows the lines of constant vorticity for the sinuous mode considering the case with maximum amplification rate α_i . In these Figures, it is possible to observe vorticity distribution for the gas ratios R_{ratio} equal to 0.25, 1.0 and 4.0, respectively. The flow structure does not change significantly with gas ratio variation. The characteristic distribution corresponding to a sinuous mode can be observed, see Figure 3.1, with vorticity concentrated at the two shear layers of the

Figure 3.6 - Sinuous mode lines of constant vorticity for the largest spatial growth rate α_i for $R_{\text{ratio}} = 0.25$ Positive values in continuous black lines, negative values in dashed lines. Vorticity range from -3.0 to 3.0 .



jet.

Figure 3.7 - Sinuous mode lines of constant vorticity for the largest spatial growth rate α_i for $R_{\text{ratio}} = 1.0$ Positive values in continuous black lines, negative values in dashed lines. Vorticity range from -3.0 to 3.0 .

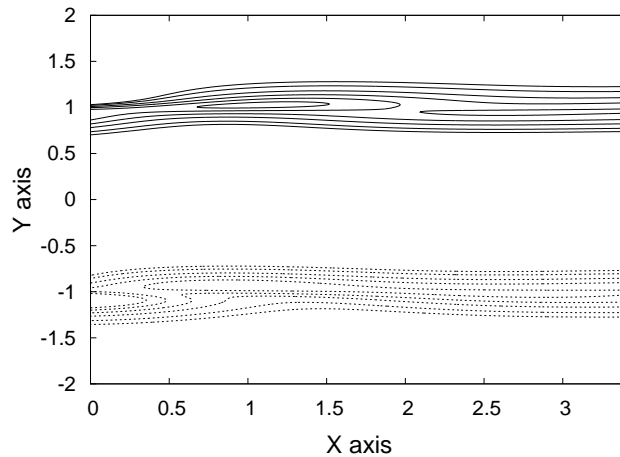
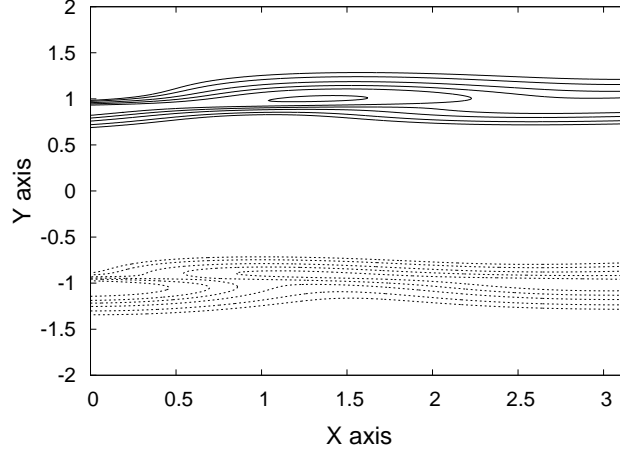


Figure 3.9 shows the pressure $\hat{p}(y)$ and the normal velocity component $\hat{v}(y)$ eigenfunctions for the sinuous mode largest spatial growth rate α_i for different gas ratios $R_{\text{ratio}} = 0.25, 1.0, 4.0$. The real and imaginary parts of the eigenfunctions \hat{p} and \hat{v} are shown. Figures are displayed in pairs, that is, side by side according to its R_{ratio} . The jet velocity profile is also demonstrated, so it is possible to see the strong correlation between the shear layer of the jet border and eigenfunction, which present

Figure 3.8 - Sinuous mode lines of constant vorticity for the largest spatial growth rate α_i for $R_{\text{ratio}} = 4.0$ Positive values in continuous black lines, negative values in dashed lines. Vorticity range from -3.0 to 3.0 .



maximum amplitudes in that region.

In Figure 3.10, streamwise velocity component $\hat{u}(y)$ eigenfunction for the sinuous mode largest spatial growth rate α_i , for different gas ratios $R_{\text{ratio}} = 0.25, 1.0, 4.0$, is shown. The disturbance phase is given by the ratio of the imaginary and real parts of the eigenfunction. In Figures 3.9 and 3.10 it is possible to see that the streamwise and normal velocity components depend significantly on R_{ratio} variation. The eigenfunction \hat{p} are less sensitive to R_{ratio} changes.

3.1.1.2 Results for the varicose mode

The same analysis conducted in the sinuous mode is now performed for varicose mode. Figure 3.11 shows the amplification rate α_i as a function of angular frequency ω for different gas ratios R_{ratio} . The behavior observed in the varicose instability is similar to the behavior observed sinuous case. It is possible to see in Figure 3.11 that the only difference between varicose and sinuous results is that for $R_{\text{ratio}} < 1$, that is, the jet less dense than the ambient, variations in the maximum amplification rate α_i are more relevant in the varicose. The range of unstable frequencies increases with increasing gas ratio R_{ratio} , the same happens in the sinuous case.

Figure 3.12 shows the wavenumber rate α_r as a function of angular frequency ω for different gas ratios R_{ratio} . Figures 3.11 and 3.12 are compared with the results from Weder (2012) thesis, showing good agreement between both works.

Figure 3.9 - Pressure $\hat{p}(y)$ and normal velocity component $\hat{v}(y)$ eigenfunctions for the sinusoidal mode largest spatial growth rate α_i for different gas ratios R_{ratio} . Mach number = 0.9. Simple jet configuration.

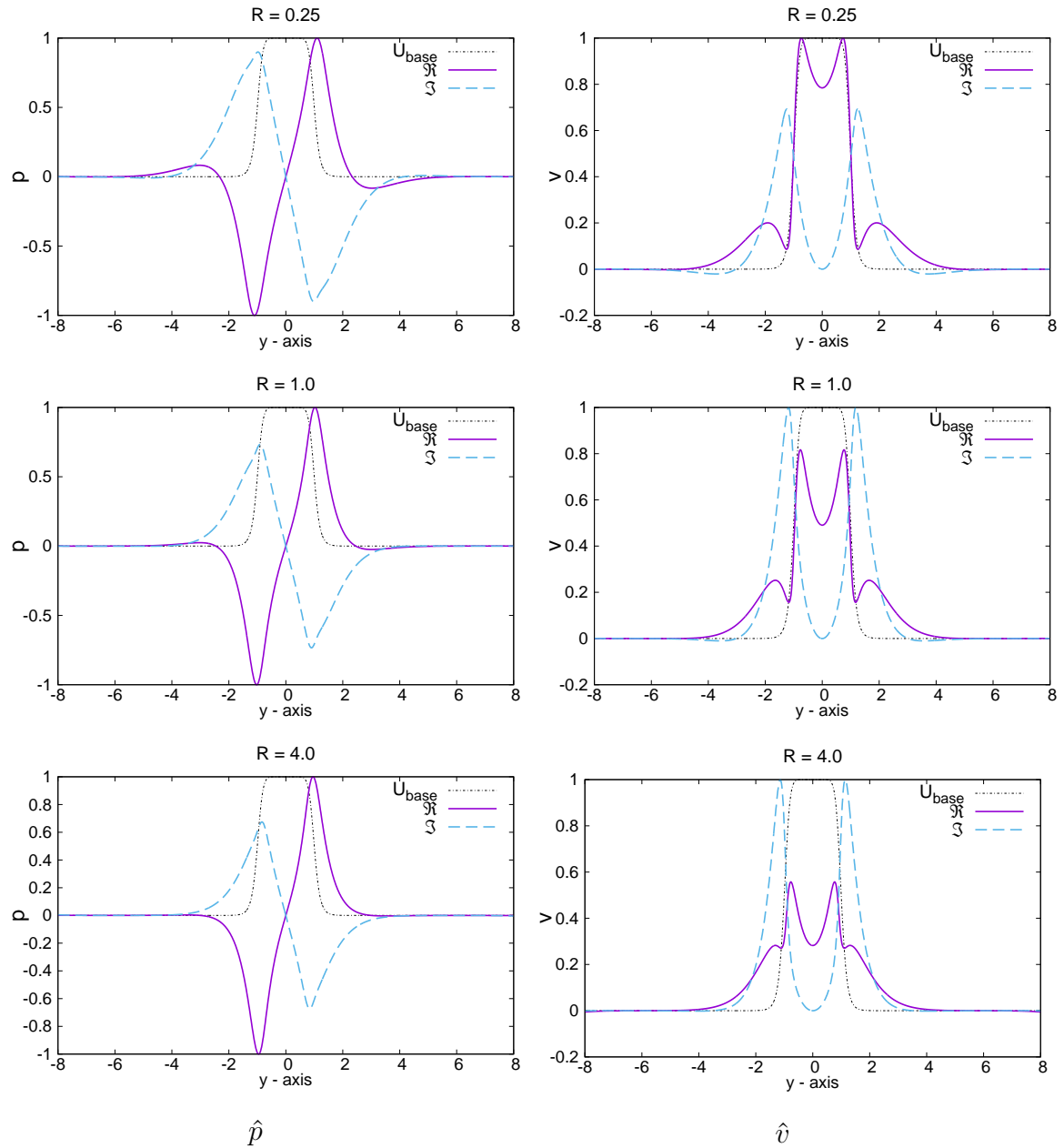
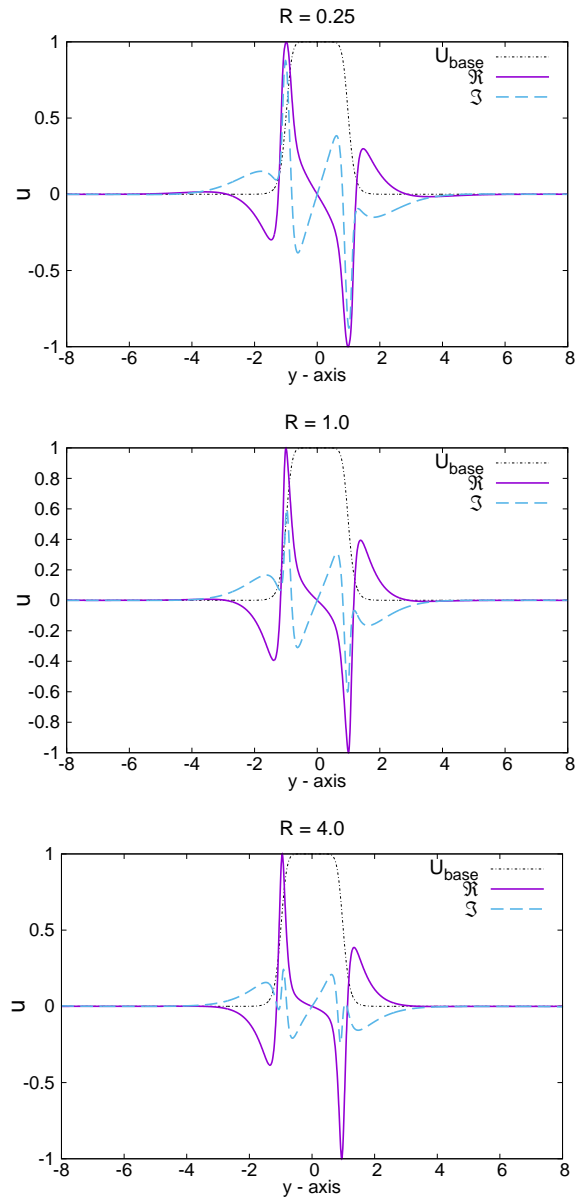


Figure 3.13 shows the phase velocity cp as a function of angular frequency ω for different gas ratios R_{ratio} . In this figure, it is possible to observe that, the lower the gas ratio R_{ratio} gets, that is, the lighter the jet becomes, more dispersive the problem become. It is also possible to see that by decreasing R_{ratio} , the frequency range in which dispersion occurs decreases. At higher frequencies the phase speed appears to have less variations, i.e, less dispersive. The same behavior that is observed in

Figure 3.10 - Streamwise velocity component eigenfunction $\hat{u}(y)$ for the sinuous mode largest spatial growth rate α_i for different gas ratios R_{ratio} and Mach number = 0.9. Simple jet configuration.



the sinuous mode is observed here in the varicose mode, meaning that lowering gas ratios R_{ratio} , results in slower perturbations velocity.

It is possible to conclude, by observing Figure 3.13 that phase speed $cp = \omega/\alpha_r$ is strongly dependent on R_{ratio} . For high gas ratios $R_{ratio} \geq 2$ and lower frequencies $\omega < 0.4$, perturbations travel with velocities near the velocities of the jet $cp \approx 1$, while for low gas ratios $R_{ratio} \leq 0.25$ and lower frequencies $\omega < 0.4$, the variation of

Figure 3.11 - Varicose mode spatial amplification rate α_i as a function of angular frequency ω for different gas ratios. Mach number = 0.9. Simple jet configuration.

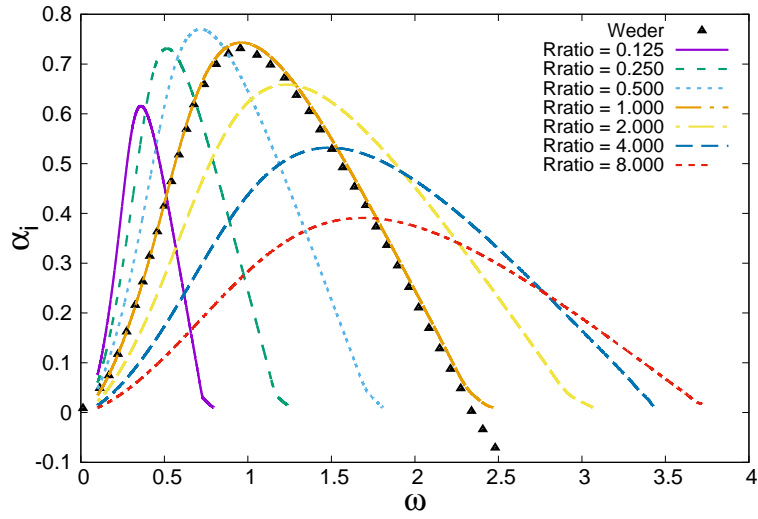
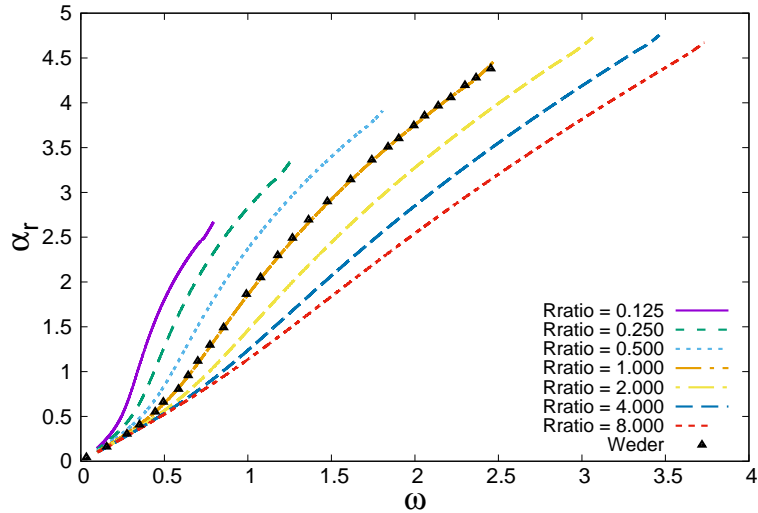


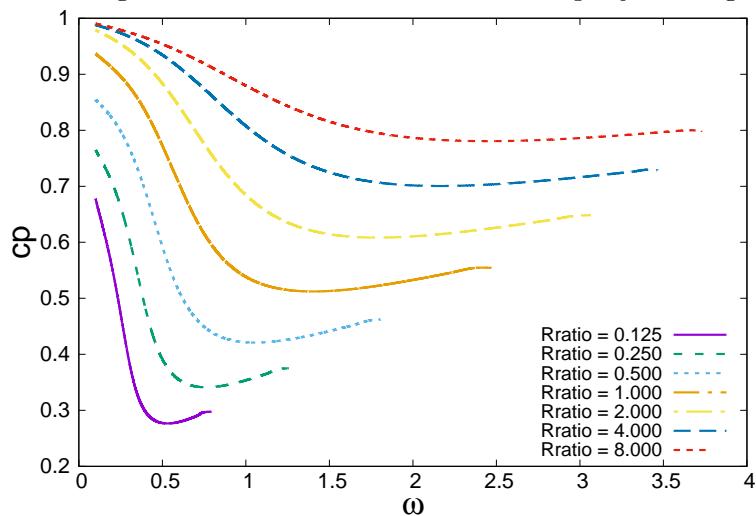
Figure 3.12 - Varicose mode streamwise wavenumber α_r as a function of angular frequency ω for different gas ratios. Mach number = 0.9. Simple jet configuration.



the perturbation velocities can decrease from approximately 0.7 to less than 0.3.

The flow structure is represented by the vorticity distribution in Figures 3.14, 3.14 and 3.14. The graphics correspond to gas ratio R_{ratio} equal to 0.25, 1.0 and 4.0, respectively. For all the graphics, the case of maximum amplification rate for each R_{ratio} is considered. The characteristic structure of a varicose oscillation can be identified, as expected Figure 3.1, and the flow structure does not present signifi-

Figure 3.13 - Varicose mode phase velocity cp as a function of angular frequency ω for different gas ratios. Mach number = 0.9. Simple jet configuration.



cant variations with different R_{ratio} . However the round inner structure that appears inside the mixing layer, vortical oval isoline, in all these Figures, seems to be convected downstream, or in other words, seems to develop further downstream with the increase of R_{ratio} .

Figure 3.14 - Varicose mode lines of constant vorticity for the largest spatial growth rate α_i for $R_{ratio} = 0.25$. $Ma = 0.90$. Positive values in continuous black lines, negative values in dashed lines. Vorticity range from -3.0 to 3.0

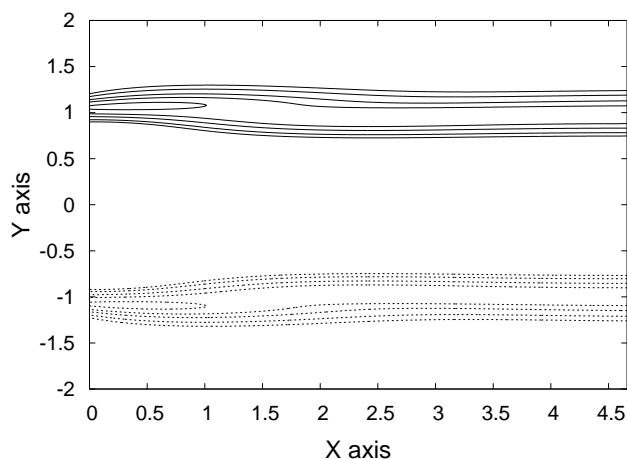


Figure 3.17 shows the pressure $\hat{p}(y)$ and the normal velocity component $\hat{v}(y)$ eigenfunctions for the sinuous mode largest spatial growth rate α_i for different gas ratios

Figure 3.15 - Varicose mode lines of constant vorticity for the largest spatial growth rate α_i for $R_{\text{ratio}} = 1.0$. $Ma = 0.90$. Positive values in continuous black lines, negative values in dashed lines. Vorticity range from -3.0 to 3.0

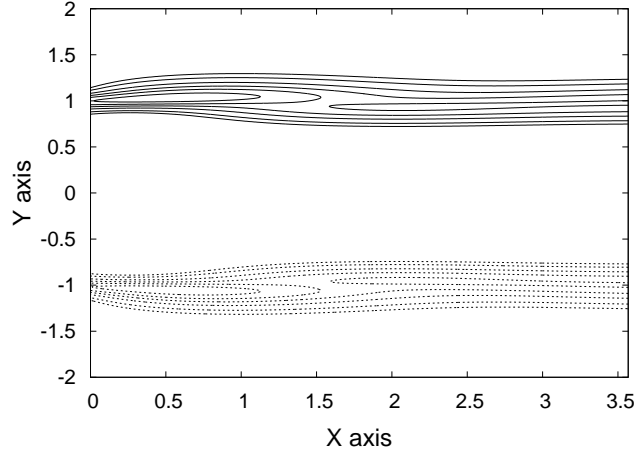
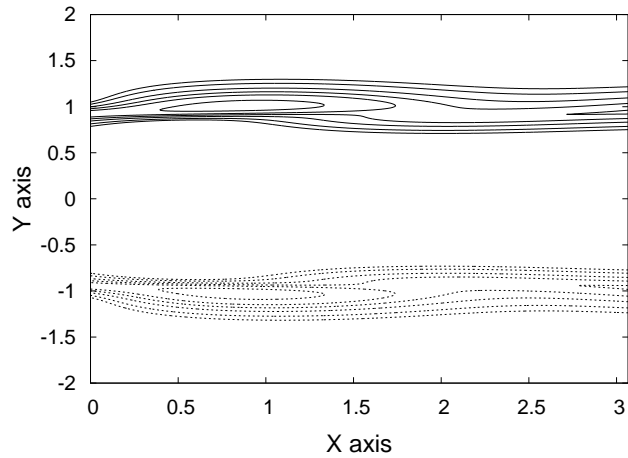


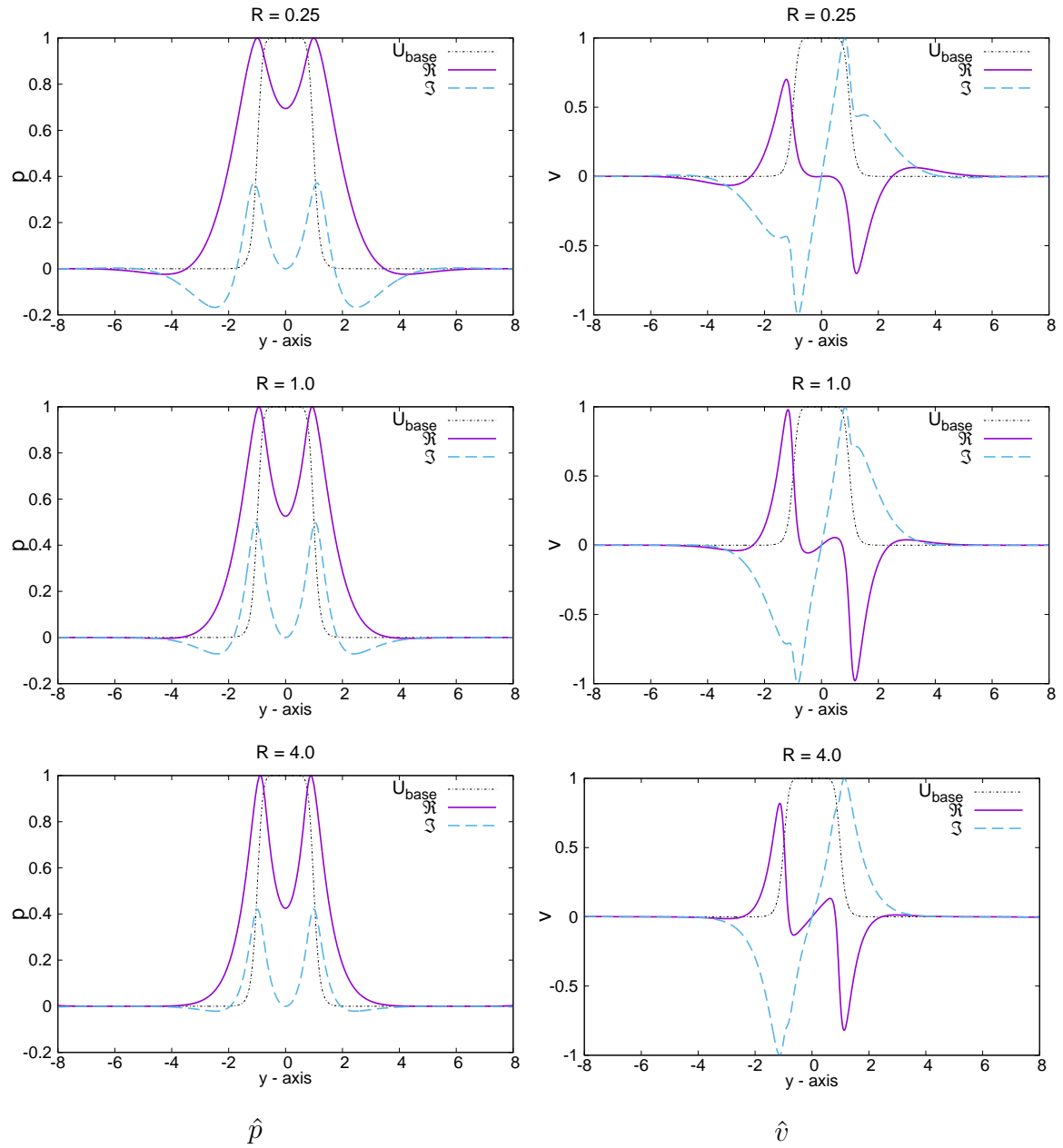
Figure 3.16 - Varicose mode lines of constant vorticity for the largest spatial growth rate α_i for $R_{\text{ratio}} = 4.0$. $Ma = 0.90$. Positive values in continuous black lines, negative values in dashed lines. Vorticity range from -3.0 to 3.0



$R_{\text{ratio}} = 0.25, 1.0, 4.0$. The real and imaginary parts of the eigenfunctions \hat{p} and \hat{v} are shown. Figures are displayed in pairs according to its R_{ratio} . Like the sinuous case, jet velocity profile is displayed with the eigenfunctions.

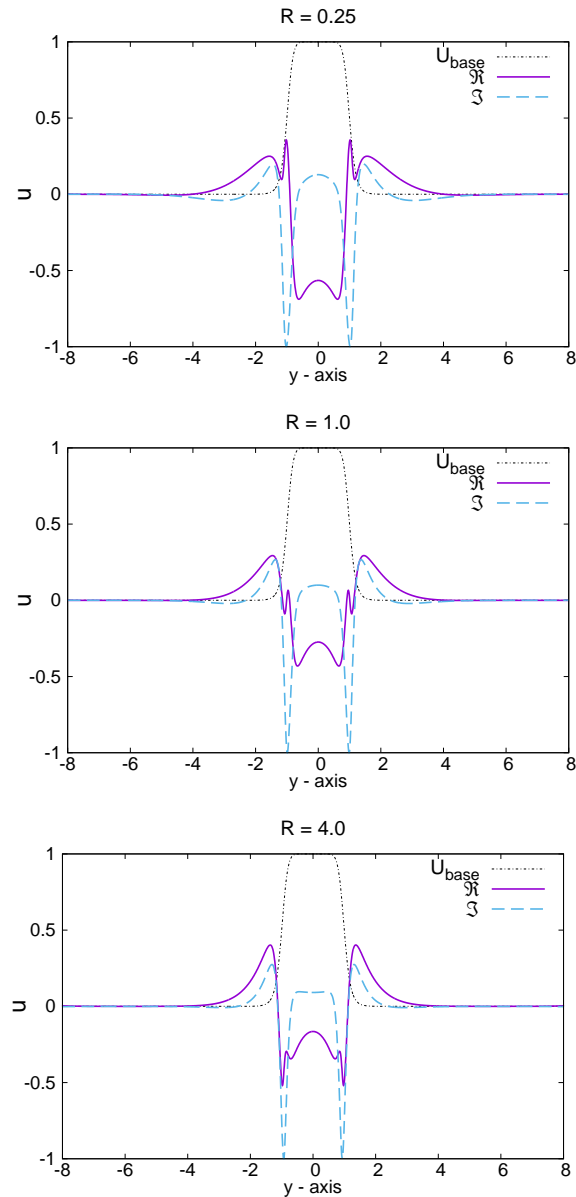
Figure 3.18 shows the streamwise velocity component eigenfunction $\hat{u}(y)$ for the varicose mode for the largest spatial growth rate α_i for three different gas ratios R_{ratio} . Observing the eigenfunction \hat{u} in Figure (3.18), it is possible to observe that maximum amplitudes are achieved inside the mixing layer.

Figure 3.17 - Pressure $\hat{p}(y)$ and normal velocity component eigenfunction $\hat{v}(y)$ for the varicose mode for the largest spatial growth rate α_i for different gas ratios R_{ratio} and Mach number = 0.9. Simple jet configuration.



Eigenfunctions \hat{u} , \hat{v} and \hat{p} are not grouped in one page due to the resulting size of each graphic, it would become unnecessarily compact. By separating them, images become more visible.

Figure 3.18 - Streamwise velocity component eigenfunction $\hat{u}(y)$ for the varicose mode for the largest spatial growth rate α_i for different gas ratios R_{ratio} and Mach number = 0.9. Simple jet configuration.



3.1.2 Co-planar jet

In this section, investigation of the spatial stability of the co-planar jet flow, see Figure 2.1, is performed. The distribution of gas species considers the outer jet and the ambient composed of the same chemical species and a different species at the inner jet, see Figure 3.2.

The comparisons are made regarding stability characteristics dependence on the gas

ratio R_{ratio} . The results allows comparisons between simple and co-planar jets. Since a co-planar jet has two shear layers, one between the inner jet and the outer jet and one between the outer jet and the ambient, two different modes are found, internal and external modes, where each of these modes have sinuous and varicose modes.

Table 3.2 - Maximum spatial amplification rate α_i and corresponding angular frequency ω , wavenumber α_r and phase speed cp for the sinuous mode, co-planar jet.

Sinuous	R_{ratio}	ω	α_r	α_i	cp
Internal mode	0.125	1.027	1.324	0.067	0.775
	0.250	1.138	1.427	0.087	0.798
	0.500	1.234	1.497	0.103	0.824
	1.000	1.309	1.534	0.112	0.853
	2.000	1.356	1.535	0.110	0.883
	4.000	1.364	1.498	0.099	0.911
	8.000	1.328	1.422	0.082	0.934
External mode	0.125	0.248	0.701	0.225	0.354
	0.250	0.403	1.121	0.413	0.359
	0.500	0.460	1.269	0.545	0.363
	1.000	0.473	1.293	0.630	0.366
	2.000	0.474	1.285	0.678	0.369
	4.000	0.473	1.274	0.704	0.371
	8.000	0.471	1.267	0.717	0.372

The largest growth rates α_i for each instability mode considering each gas ratio R_{ratio} and the corresponding angular frequency ω , streamwise wavenumber α_r and phase speed cp are given in Tables 3.2 and 3.3 for the sinuous and varicose modes respectively. The largest growth rate for the internal mode corresponds to gas ratio $R_{ratio} = 1$. The external mode growth rate increases continuously for increasing gas ratio R_{ratio} . Comparison between both tables, show that the results regarding sinuous and varicose modes do not differ much in terms of largest growth rates and corresponding angular frequencies for a given gas ratio.

The growth rates of the external modes are much higher than the growth rates of the internal modes. The external modes have growth rates comparable to the growth rates of the simple jet presented in Table 3.1, although the co-planar jet frequencies do not depend on the gas ratio as much as the frequencies of the simple jet. This has significant impact on the mixture of different species, since the interface between different species at the boundary of the inner and the outer jets is more stable. The higher growth rates of the external modes are due to the choice of velocity ratio

Table 3.3 - Maximum spatial amplification rate α_i and corresponding angular frequency ω , wavenumber α_r and phase speed cp for the varicose instability, co-planar jet.

Varicose	R_{ratio}	ω	α_r	α_i	cp
Internal mode	0.125	0.950	1.207	0.062	0.787
	0.250	1.086	1.340	0.082	0.810
	0.500	1.221	1.458	0.097	0.837
	1.000	1.353	1.560	0.103	0.867
	2.000	1.477	1.648	0.097	0.896
	4.000	1.576	1.708	0.083	0.923
	8.000	1.627	1.723	0.063	0.944
External mode	0.125	0.261	0.716	0.238	0.364
	0.250	0.400	1.107	0.414	0.361
	0.500	0.455	1.250	0.547	0.364
	1.000	0.470	1.279	0.631	0.367
	2.000	0.472	1.275	0.679	0.370
	4.000	0.471	1.268	0.704	0.371
	8.000	0.472	1.263	0.679	0.372

between the inner jet and the outer jet, which is equal to 0.7, such that the external velocity gradient is higher.

In Figures 3.19 and 3.20, spatial amplification rate α_i is displayed as a function of frequency ω , for the sinuous mode, considering seven different gas ratios R_{ratios} . The jet configuration used here is co-planar jet, see Figure 2.1. Figure 3.19 represents the results for the external mode, that is, the mode found in between the quiescent ambient and the external jet and Figure 3.20 represents the results for the internal mode, that is, mode is found in between the central jet and the outer jet.

In Figures 3.19 and 3.20 it is possible to see that the external mode presents higher values of maximum amplification rate α_i than values of maximum amplification ratio of internal mode. In Figure 3.19 it is also possible to see that for the external mode, the maximum amplification ratio increases with increasing gas ratio R_{ratio} . A different behavior is observed for the internal mode. In Figure 3.20, the maximum amplification ratio R_{ratio} reaches maximum value for gas ratio $R_{ratio} = 1.0$, then stars to decrease. External mode, besides having a higher maximum amplification rate or growth rate, has a range of unstable frequencies that is smaller than the unstable frequency range of the internal mode.

Figure (3.21) shows the wavenumber α_r as a function of angular frequency ω , for

Figure 3.19 - Spatial amplification rate α_i as a function of angular frequency ω , for different gas ratios. Mach number = 0.9. Sinuous external mode. Co-planar jet configuration.

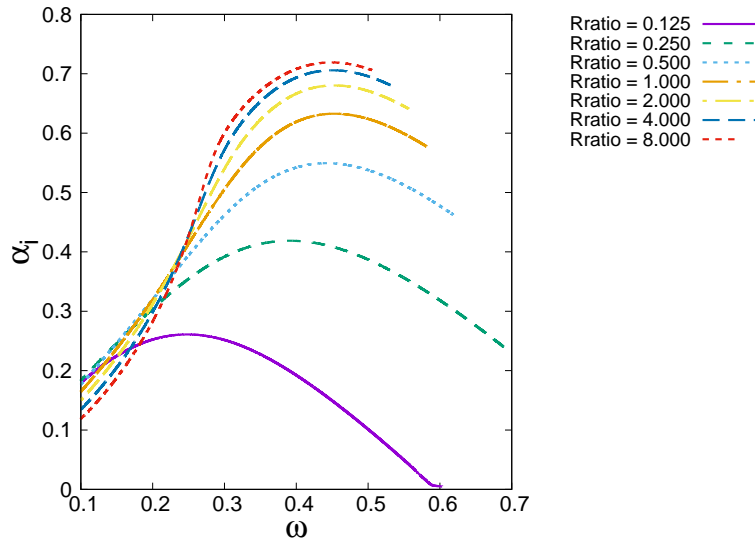
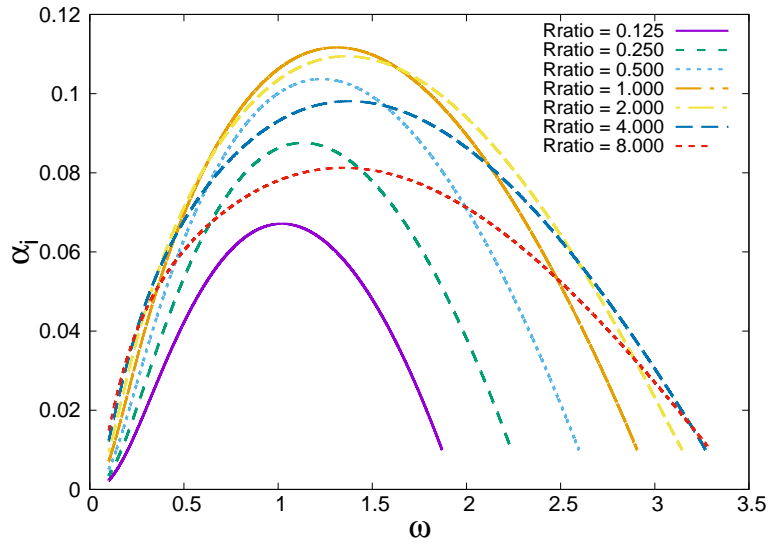


Figure 3.20 - Spatial amplification rate α_i for the sinuous mode as a function of angular frequency ω , for different gas ratios. Mach number = 0.9. Sinuous internal mode. Co-planar jet configuration.



seven different gas ratios R_{ratio} , for external sinuous mode and co-planar jet configuration.

Figure (3.23) shows the phase velocity cp as a function of angular frequency ω , for different gas ratios, for sinuous external mode and co-planar jet configuration. In this Figure it is possible to see that to increase the gas ratio R_{ratio} makes the problem less

Figure 3.21 - Wavenumber α_r as a function of angular frequency ω , for different gas ratios R_{ratio} . Mach number = 0.9. Sinuous external mode. Co-planar jet configuration.

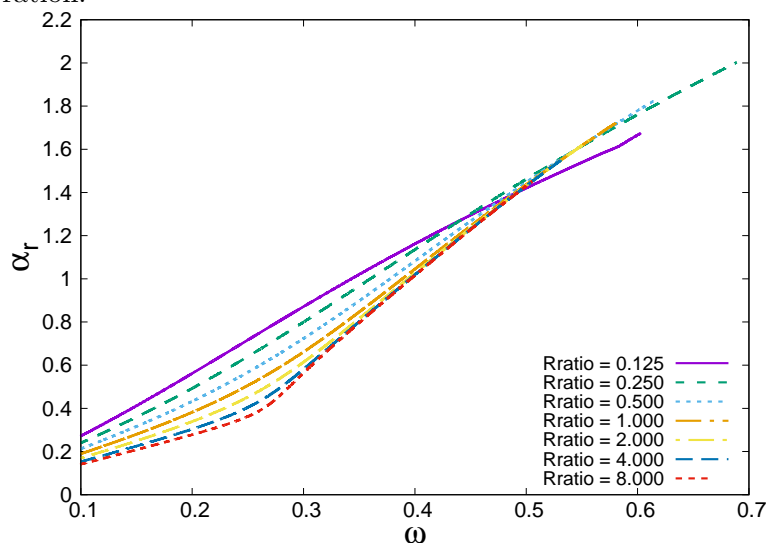
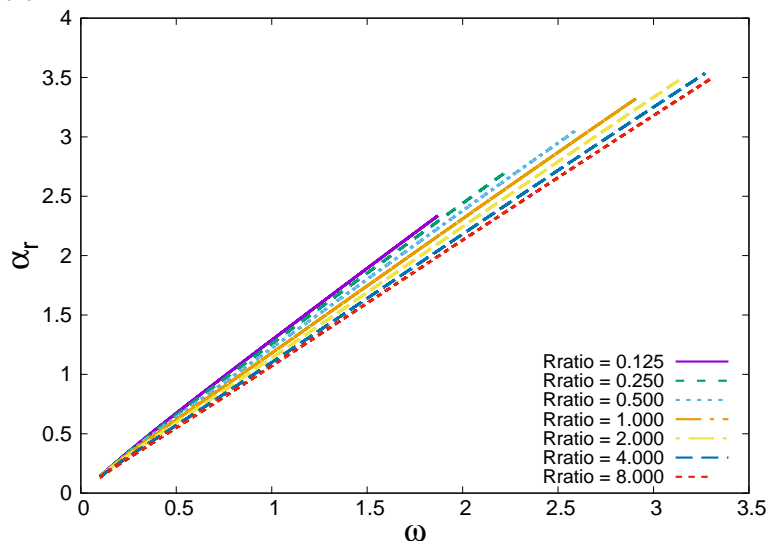


Figure 3.22 - Wavenumber α_r as a function of angular frequency ω , for different gas ratios R_{ratio} . Mach number = 0.9. Sinuous internal mode. Co-planar jet configuration.



dispersive for frequencies $\omega > 0.25$. For frequencies $\omega < 0.25$, the problem appears to have very low dispersion, independent of the chosen gas ratio R_{ratio} . However, for the lower frequencies, to increase the gas ratio increases the velocity that the perturbations travel in the flow. It is important to highlight that the inner jet has different species than the outer jet. The outer jet and the ambient have the same density and mass as initial condition, so the external mode is inside a region with

only one gas.

Figure 3.23 - Phase velocity cp as a function of angular frequency ω , for different gas ratios. Mach number = 0.9. Sinuous external mode. Co-planar jet configuration.

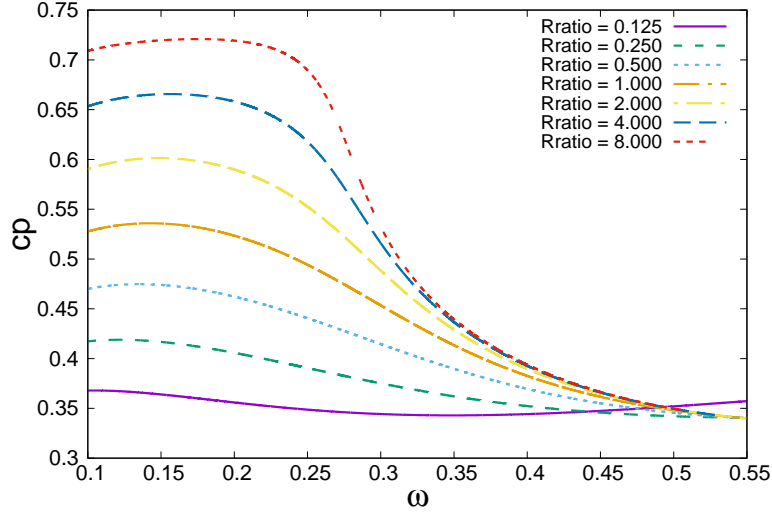
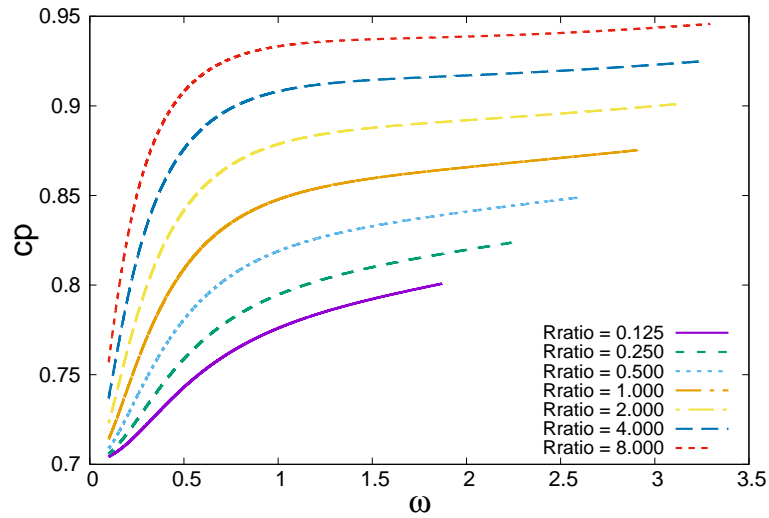


Figure (3.24) shows the phase velocity cp as a function of angular frequency ω , for different gas ratios, for sinuous internal mode and co-planar jet configuration. In this figure, it is possible to observe that, for lower frequencies, the internal mode is dispersive for all the gas ratios R_{ratio} , to increase the frequency diminishes the dispersion. Similarly to the external mode, to increase the density of the internal jet, that is, to increase the gas ratio R_{ratio} increases the velocity that the perturbations travel inside the flow.

Figures 3.25, 3.26 and 3.27 shows the isolines of vorticity for the sinuous mode considering the sum of internal and external modes. The largest spatial amplification rate α_i for both internal and external modes are used. The Figure 3.25 represents gas ratio of $R_{ratio} = 0.25$, the Figure 3.26 represents gas ratio of $R_{ratio} = 1.0$ and the Figure 3.27 represents gas ratio of $R_{ratio} = 4.0$. As throughout the whole work, Mach number of the inner jet is $Ma = 0.90$ and the isolines of vorticity present values ranging from -3.0 to 3.0, recalling that positive values are in continuous black lines and negative values are presented in dashed lines.

The sinuous flow structure presented in the three images of Figures 3.25, 3.26 and 3.27, like the the structure presented in Figure 3.1, can be observed in the inner jet, while it is much more subtle for the outer mode. The inner disturbances are shown

Figure 3.24 - Phase velocity cp as a function of angular frequency ω , for different gas ratios. Mach number = 0.9. Sinuous internal mode. Co-planar jet configuration.



in phase, but since the disturbances travel at different speeds the phase between the inner and outer modes changes continuously. No significant change in flow topology is observed for different gas ratio.

Figure 3.25 - Lines of constant vorticity for sinuous mode with the largest spatial amplification rate α_i of both internal and external modes, for $R_{ratio} = 0.25$. Vorticity range from -3.0 to 3.0. Positive values in continuous black lines, negative values in dashed lines.

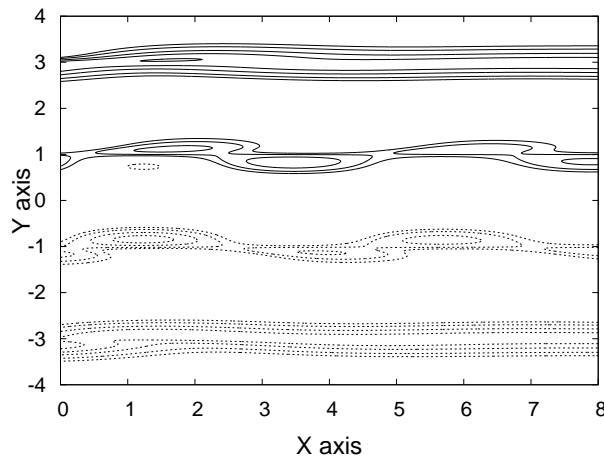


Figure 3.28 presents pressure $\hat{p}(y)$ and normal velocity component $\hat{v}(y)$ eigenfunctions for maximum spatial amplification rate α_i as a function of y coordinate, con-

Figure 3.26 - Lines of constant vorticity for sinuous mode with the largest spatial amplification rate α_i of both internal and external modes, for $R_{\text{ratio}} = 1.0$. Vorticity range from -3.0 to 3.0. Positive values in continuous black lines, negative values in dashed lines.

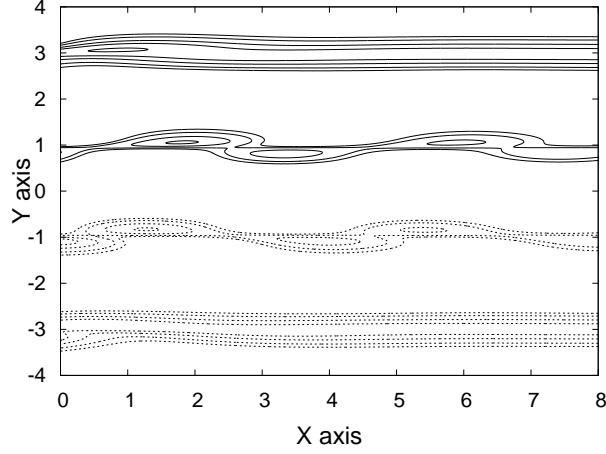
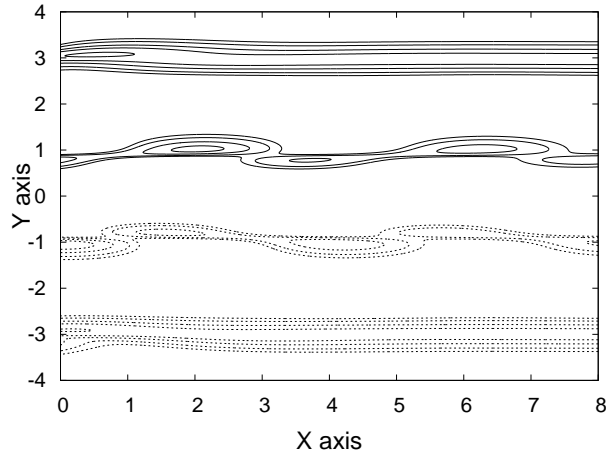


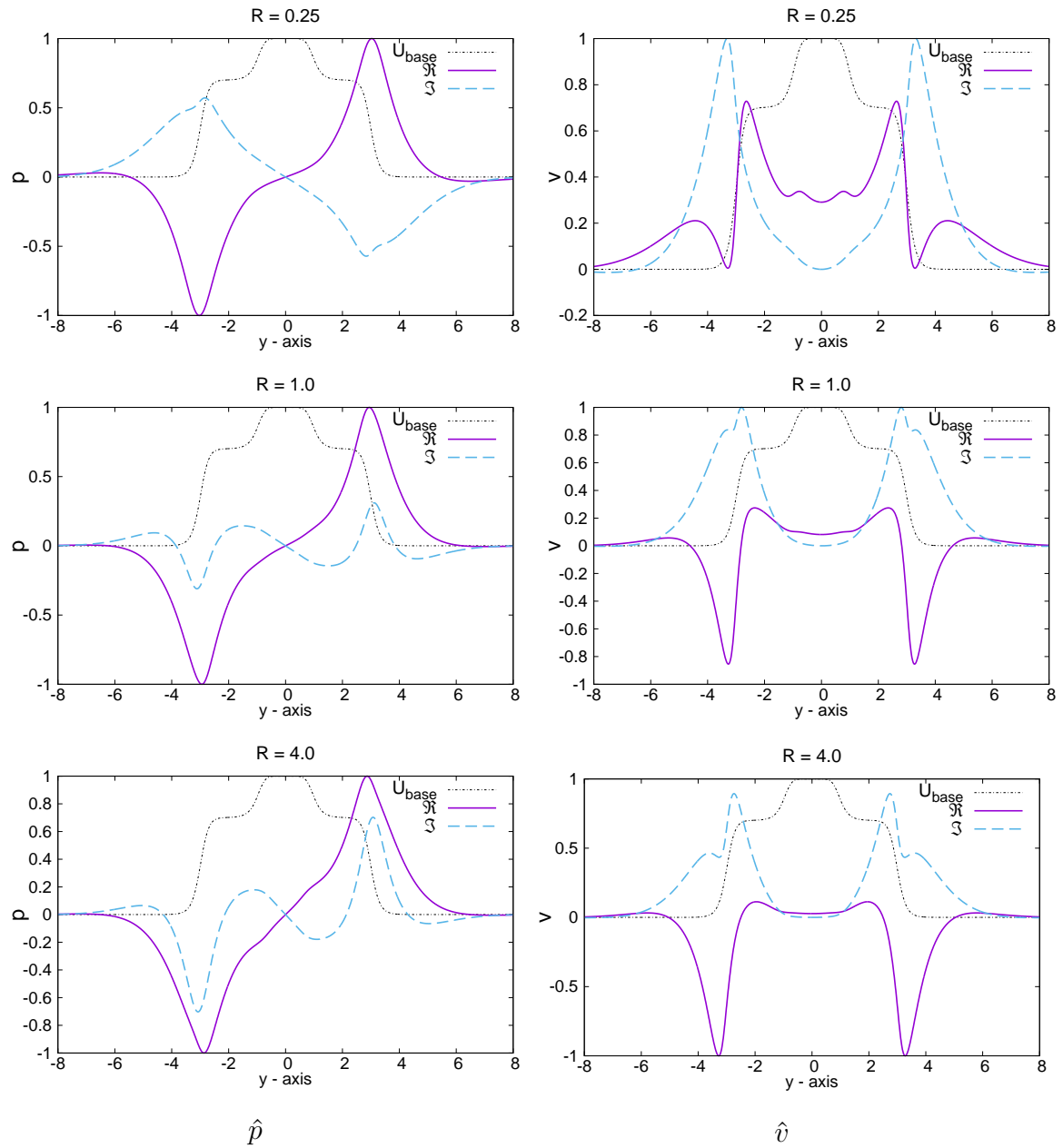
Figure 3.27 - Lines of constant vorticity for sinuous mode with the largest spatial amplification rate α_i of both internal and external modes, for $R_{\text{ratio}} = 4.0$. Vorticity range from -3.0 to 3.0. Positive values in continuous black lines, negative values in dashed lines.



sidering three different gas ratios $R_{\text{ratio}} = 0.25, 1.0$ and 4.0 for the sinuous external mode and co-planar jet configuration. In this Figure it is possible to identify external mode for the three gas ratios R_{ratio} for the maximum amplification rate.

The pressure $\hat{p}(y)$ and the normal velocity component $\hat{v}(y)$ eigenfunctions seems to be dependent, on the gas ratio R_{ratio} variation. The eigenfunctions are complex numbers, then both values are displayed in the graphic, where \Re indicates the real

Figure 3.28 - Pressure $\hat{p}(y)$ and normal velocity component $\hat{v}(y)$ eigenfunction for the sinusoidal mode with maximum spatial amplification rate α_i for different gas ratios R_{ratio} and Mach number = 0.9, external mode, co-planar jet configuration.



part and \Im indicates the imaginary part. Also, the velocity profile is plotted with the eigenfunctions to ease on the perception of shear layer-eigenfunction correlation. In Figure 3.28, observing gas ratio $R_{\text{ratio}} = 0.25, 1.0$ for $\hat{v}(y)$, this dependence becomes clear when observing the sign inversion in the real part \Re of the eigenfunction \hat{v} .

Figure 3.29 presents pressure $\hat{p}(y)$ and normal velocity component $\hat{v}(y)$ eigenfunc-

tions for maximum spatial amplification rate α_i as a function of y coordinate, considering three different gas ratios $R_{\text{ratio}} = 0.25, 1.0$ and 4.0 , respectively, for the sinuous internal mode and co-planar jet configuration. Correlation between the eigenfunctions and the corresponding shear layer allows the identification of the inner and outer modes, in this Figure the mentioned correlation identify the internal mode for three gas ratios R_{ratio} considering maximum amplification rate α_i . Also, Figure 3.29 shows that for gas ratio $R_{\text{ratio}} = 0.25$ the eigenfunction \hat{p} does not decay like in the other cases. When this happens, oscillations are propagated far away from its source and decays very slowly. This mode is called a radiating mode. Radiating modes have acoustic behavior, thus it will not be discussed here, however it is something that require further investigation.

Figure 3.30 shows the streamwise velocity component eigenfunction $\hat{u}(y)$ for maximum spatial amplification rate α_i considering three different gas ratios $R_{\text{ratio}} = 0.25, 1.0$ and 4.0 , for sinuous external mode and co-planar jet configuration. Like in the previous Figures, here is also possible to identify the external mode looking at the maximum amplitude of the eigenfunction \hat{u} .

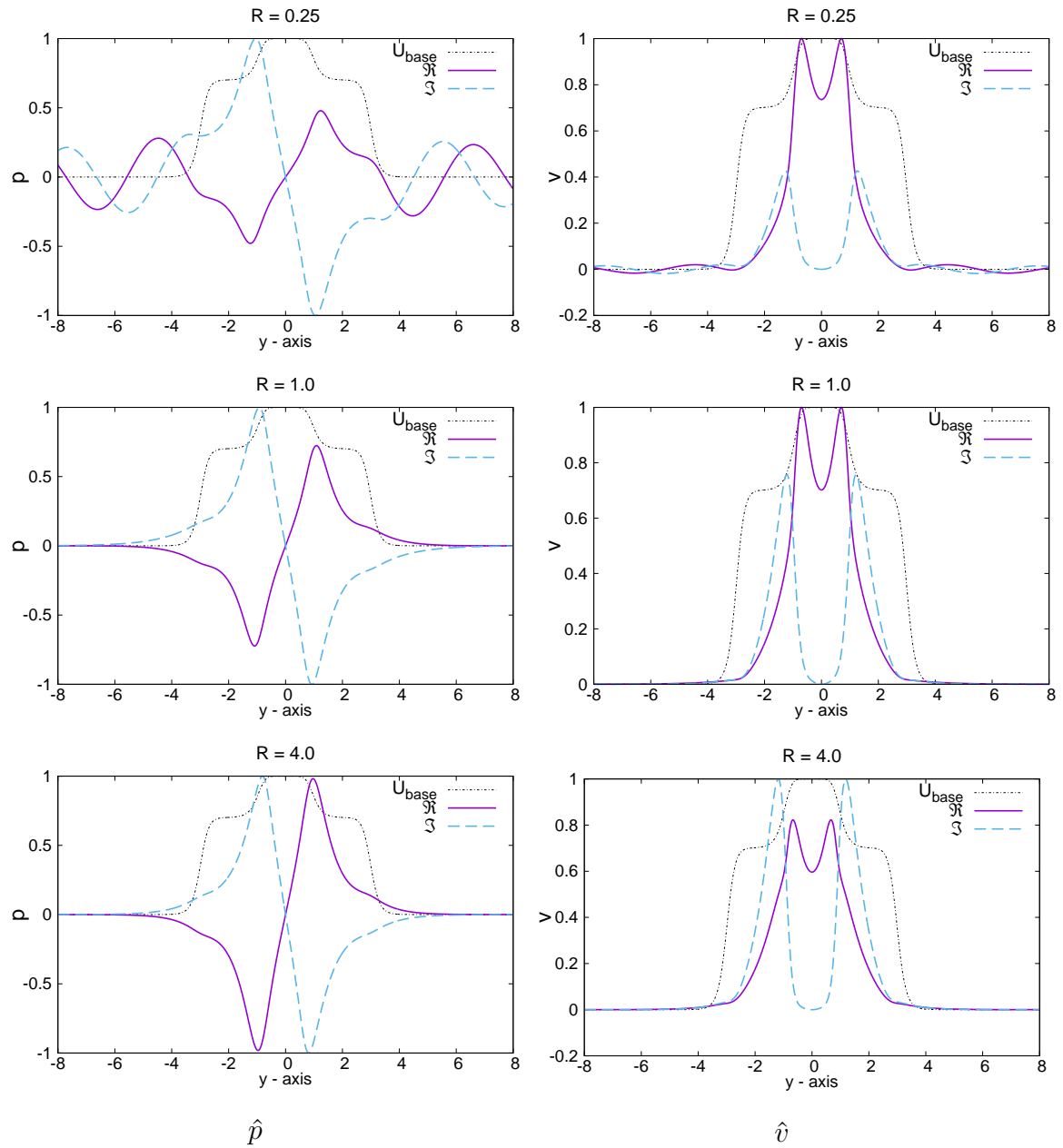
Figure 3.31 is similar to the previous figure, it shows the streamwise velocity component eigenfunction $\hat{u}(y)$ for maximum spatial amplification rate α_i considering three different gas ratios $R_{\text{ratio}} = 0.25, 1.0$ and 4.0 , for sinuous internal mode and co-planar jet configuration. Identification of internal mode is made by looking at the maximum amplitude of the eigenfunction \hat{u} . In both Figures 3.31 and 3.31, external mode and internal mode, respectively, the biggest difference appears to be between gas ratio $R_{\text{ratio}} = 0.25$ and $R_{\text{ratio}} = 1.0$.

3.1.2.1 Results for the varicose mode

In this section, results of internal and external varicose modes are presented. For the co-planar jet varicose external and internal modes, respectively, Figures 3.32 and 3.32 shows the spatial amplification rate as a function of frequency ω for different gas ratios R_{ratio} . Analyzing the amplification rate comparatively with the sinuous case, it is noticeable that differences between the varicose and sinuous for internal and external mode seems to be mild, with both cases having a similar behavior.

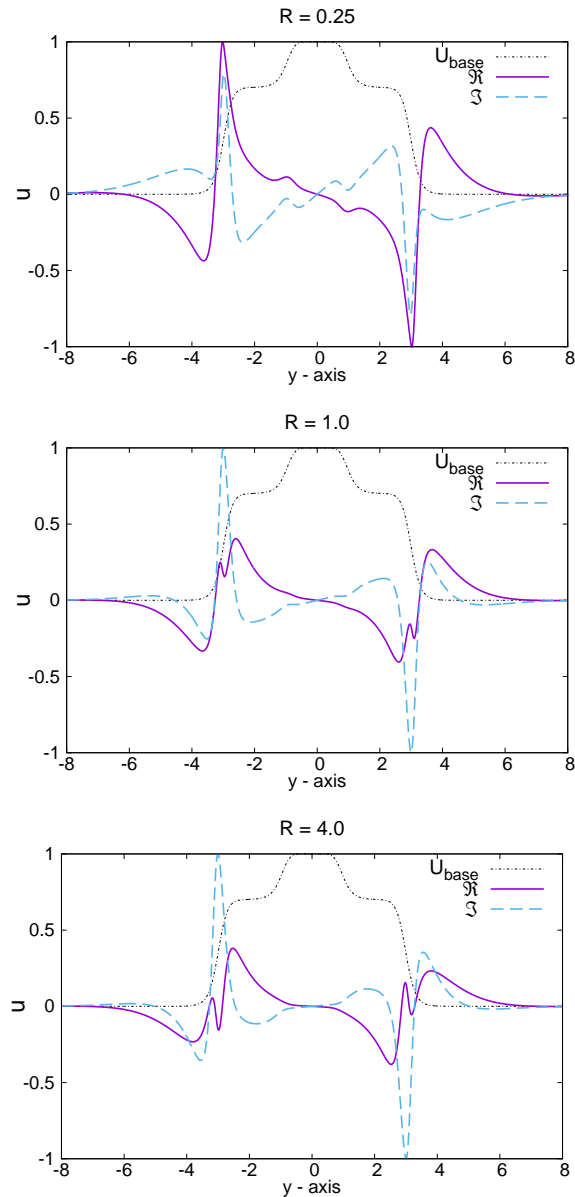
In Figure 3.32 it is possible to see that higher values of maximum amplification rate α_i are found in the external mode. The maximum amplification ratio of internal mode correspond to gas ratio $R_{\text{ratio}} = 1$, see Figure 3.33. The highest value of the internal mode is lower than the lowest amplification rate of the external mode.

Figure 3.29 - Pressure $\hat{p}(y)$ and normal velocity component $\hat{v}(y)$ eigenfunction for the sinusoidal mode with maximum spatial amplification rate α_i for different gas ratios R_{ratio} and Mach number = 0.9, internal mode, co-planar jet configuration.



Similarity to the sinusoidal mode can be seen in Figure 3.32. It is also possible to identify that for the external mode, the maximum amplification ratio increases with increasing gas ratio R_{ratio} . For the internal mode, Figure 3.33, the maximum amplification ratio R_{ratio} reaches maximum value when the gas ratio reaches $R_{ratio} = 1.0$, then, after that, maximum amplification rate start to decrease. The range of unstable frequencies of the external mode is wider than the range of unstable frequencies

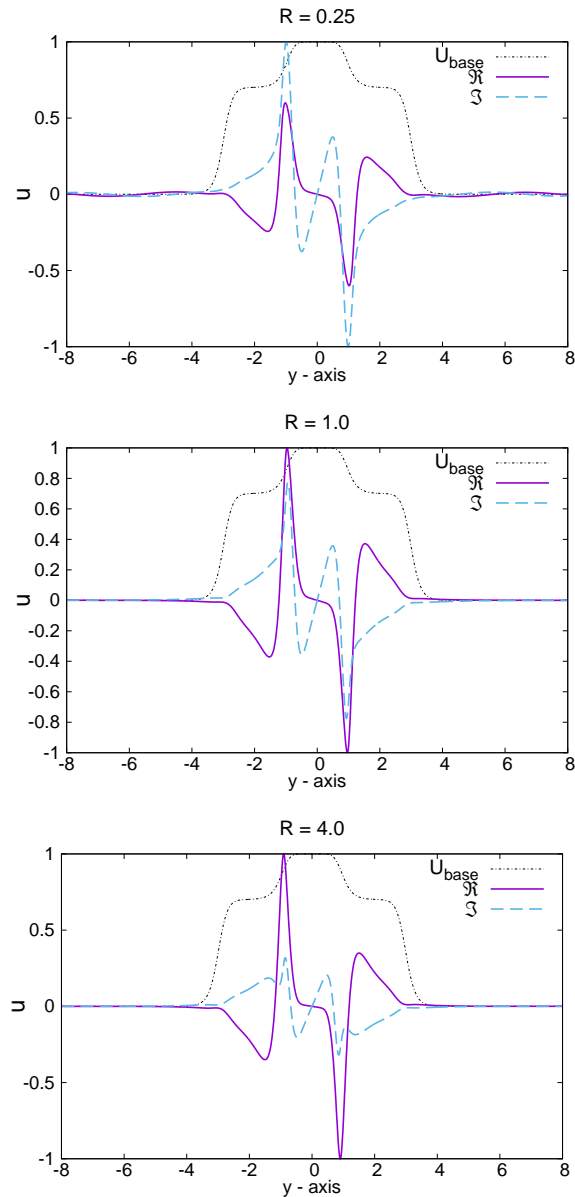
Figure 3.30 - Streamwise velocity component eigenfunction $\hat{u}(y)$ for sinuous mode with maximum spatial amplification rate α_i for different gas ratios R_{ratio} and Mach number = 0.9, external mode, co-planar jet configuration.



of internal mode, for all gas ratios R_{ratio} considered.

Figures 3.34 and 3.35, shows the wavenumber α_r of varicose external and internal modes, as a function of angular frequency ω , for different gas ratios. Wavenumber α_r is displayed because these values are used in order to calculate the phase speed $cp = \omega/\alpha_r$. Comparing these both previous mentioned Figures, it is possible to predict that the external mode is more dispersive than the internal mode, however

Figure 3.31 - Streamwise velocity component eigenfunction $\hat{u}(y)$ for the sinuous mode with maximum spatial amplification rate α_i for different gas ratios R_{ratio} and Mach number = 0.9, internal mode, co-planar jet configuration.



dispersion will be better discussed in Figures 3.36 and 3.36.

Figures 3.36 and 3.36 shows the phase velocity c_p , of varicose external mode, as a function of angular frequency ω for the co-planar jet configuration.

Figure 3.36 shows that the problem is highly dispersive for low frequencies ($\omega < 0.45$). To increase the gas ratio, increases the velocity that perturbations travel inside the flow for the external mode. Maximum dispersion is obtained for the frequency

Figure 3.32 - Spatial amplification rate α_i as a function of angular frequency ω , for different gas ratios. Mach number = 0.9. Varicose external mode. Co-planar jet configuration.

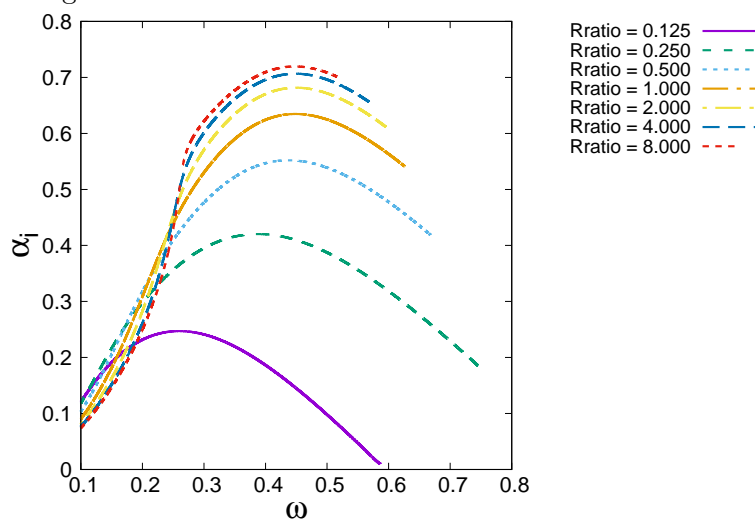
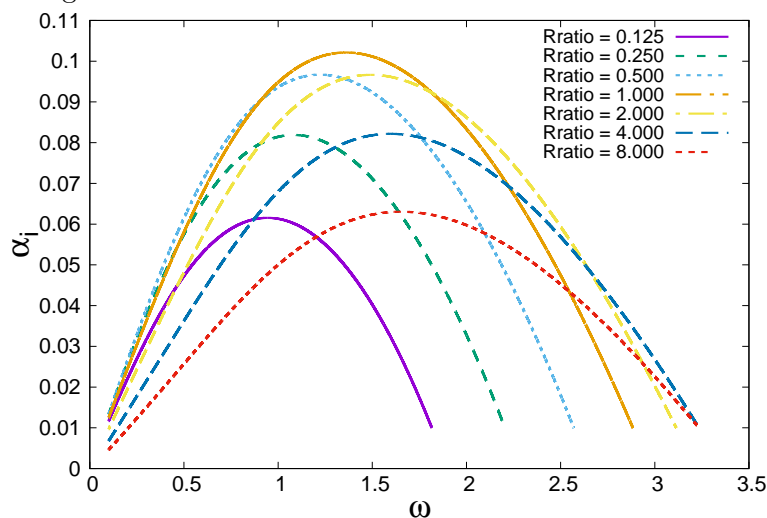


Figure 3.33 - Spatial amplification rate α_i as a function of angular frequency ω , for different gas ratios. Mach number = 0.9. Varicose internal mode. Co-planar jet configuration.



range of $0.27 < \omega < 0.35$ and gas ratio $R_{ratio} = 8.0$ Figure 3.37 shows the phase speed cp of the internal mode and it seems to have very low dispersion. Comparatively, the varicose internal mode is less dispersive in all of frequency range analyzed, while the external mode is somewhat more dispersive. The external mode can only be considered less dispersive for frequencies bigger than $\omega > 0.45$.

Figure 3.34 - Wavenumber α_r as a function of angular frequency ω , for different gas ratios. Mach number = 0.9. Varicose external modes. Co-planar jet configuration.

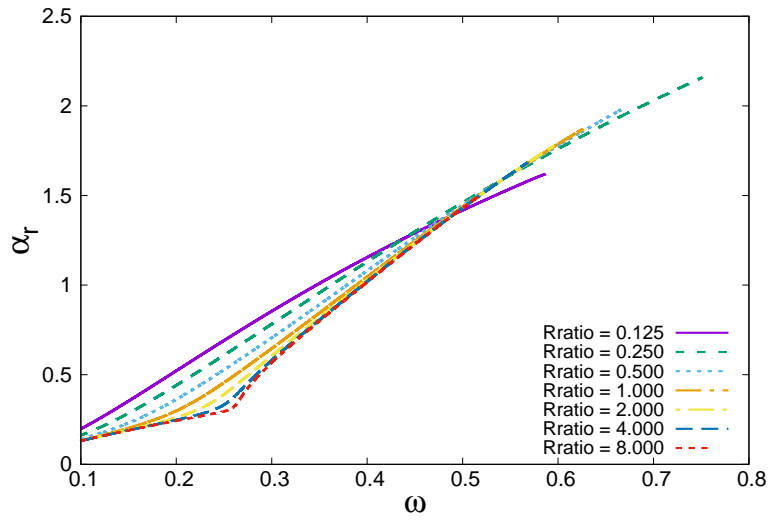
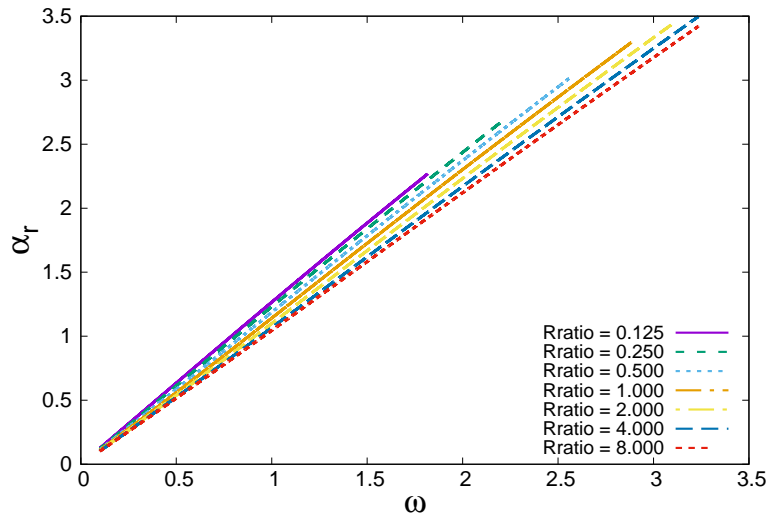
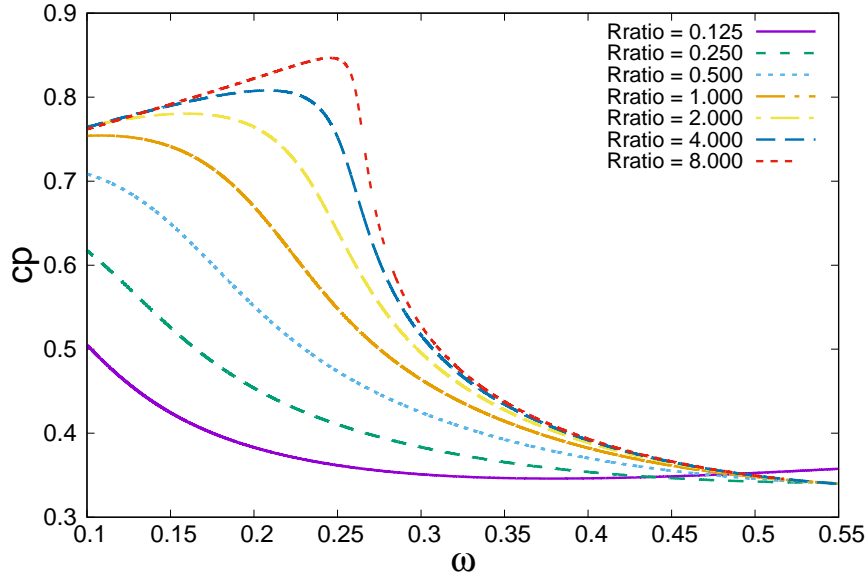


Figure 3.35 - Wavenumber α_r as a function of angular frequency ω , for different gas ratios. Mach number = 0.9. Varicose external modes. Co-planar jet configuration.



The effects of binary mixing of the varicose mode is similar to the sinuous mode. The external mode is strongly damped with decreasing gas ratio, both in terms of growth rate and range of unstable frequencies. The internal mode is less sensitive to the effect of binary mixing, where the largest amplification rate varies by about 50% and the range of unstable frequencies is reduced by the same amount for the lower values of gas ratio.

Figure 3.36 - Phase velocity cp as a function of angular frequency ω for different gas ratios. Mach number = 0.9. Varicose external mode. Co-planar jet configuration.



The implications for transition to turbulence are the same, low values of gas ratio result in strong damping of instabilities and range of unstable frequencies, while high gas ratios are somewhat more unstable than the uniform flow (gas ratio $R_{ratio} = 1$).

The phase speed reduces significantly as the gas ratio is reduced both for the internal and external modes.

Figures 3.38, 3.39 and 3.40 shows the isolines of vorticity for the varicose mode, the sum of internal and external modes is performed to display both modes together. The case of maximum spatial amplification rate α_i of both internal and external modes is used. Figure 3.38 represents gas ratio of $R_{ratio} = 0.25$, the Figure 3.39 represents gas ratio of $R_{ratio} = 1.0$ and the Figure 3.40 represents gas ratio of $R_{ratio} = 4.0$. Isolines of vorticity present values ranging from -3.0 to 3.0.

The varicose flow structure presented in the Figures 3.38, 3.39 and 3.40, like the the structure presented in Figure 3.1, can be observed in the inner jet, while it is much more subtle for the outer mode. The inner disturbances are shown in phase, but since the disturbances travel at different speeds the phase between the inner and outer modes changes. No significant change in flow topology is observed for different gas ratio.

Figure 3.41 presents three graphics for the pressure $\hat{p}(y)$ eigenfunction in the left

Figure 3.37 - Phase velocity cp as a function of angular frequency ω for different gas ratios. Mach number = 0.9. Varicose internal mode. Co-planar jet configuration.

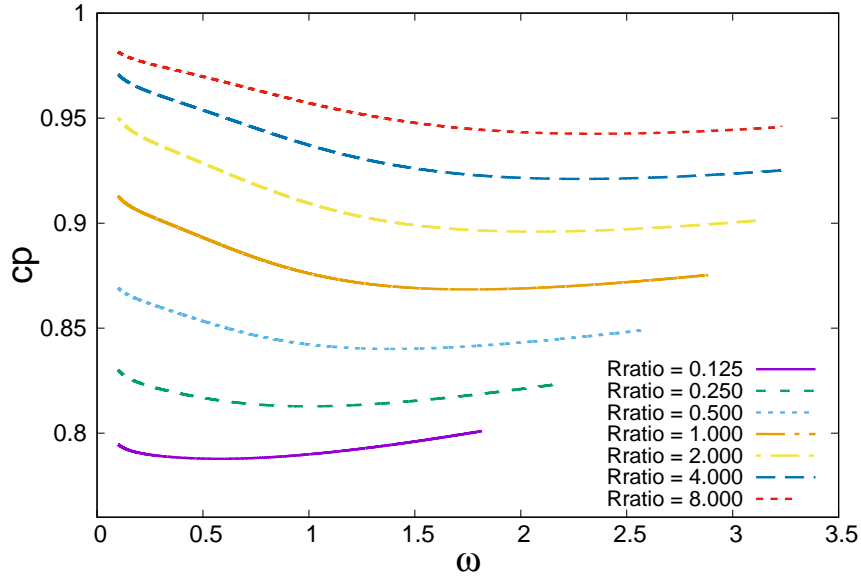
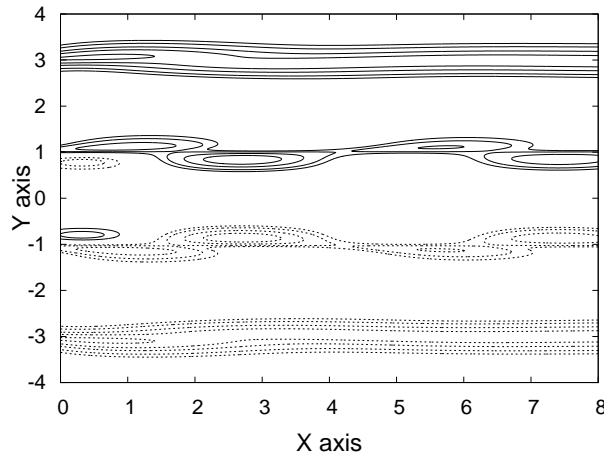


Figure 3.38 - Lines of constant vorticity for varicose mode with the largest spatial amplification rate α_i of both internal and external modes, for $R_{ratio} = 0.25$. Vorticity range from -3.0 to 3.0. Positive values in continuous black lines, negative values in dashed lines.



column and three graphics normal velocity component $\hat{v}(y)$ eigenfunction in the right column. All these graphics are disposed in pairs, relative to its gas ratio R_{ratio} for external varicose mode, considering the maximum spatial amplification rate α_i of each case. In Figure 3.41, it is possible to see that maximum amplitude of \hat{p} and \hat{v} identifies the external modes of the problem. Dependence of \hat{p} and \hat{v} on gas ratio R_{ratio} variations can be observed.

Figure 3.39 - Lines of constant vorticity for varicose mode with the largest spatial amplification rate α_i of both internal and external modes, for $R_{ratio} = 1.0$. Vorticity range from -3.0 to 3.0. Positive values in continuous black lines, negative values in dashed lines.

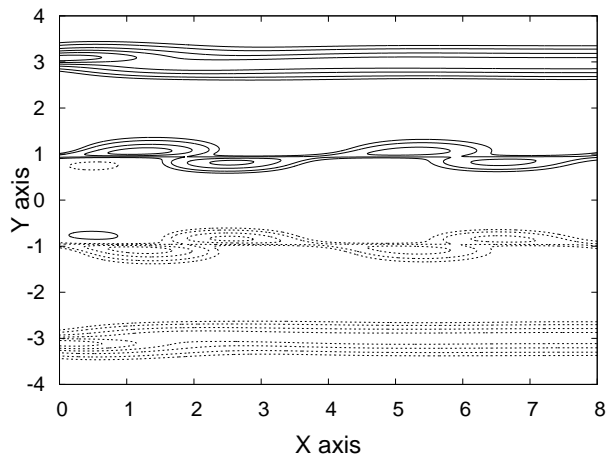


Figure 3.40 - Lines of constant vorticity for varicose mode with the largest spatial amplification rate α_i of both internal and external modes, for $R_{ratio} = 4.0$. Vorticity range from -3.0 to 3.0. Positive values in continuous black lines, negative values in dashed lines.

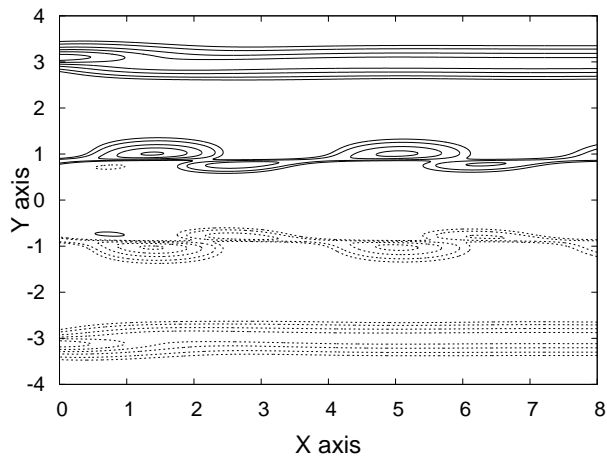
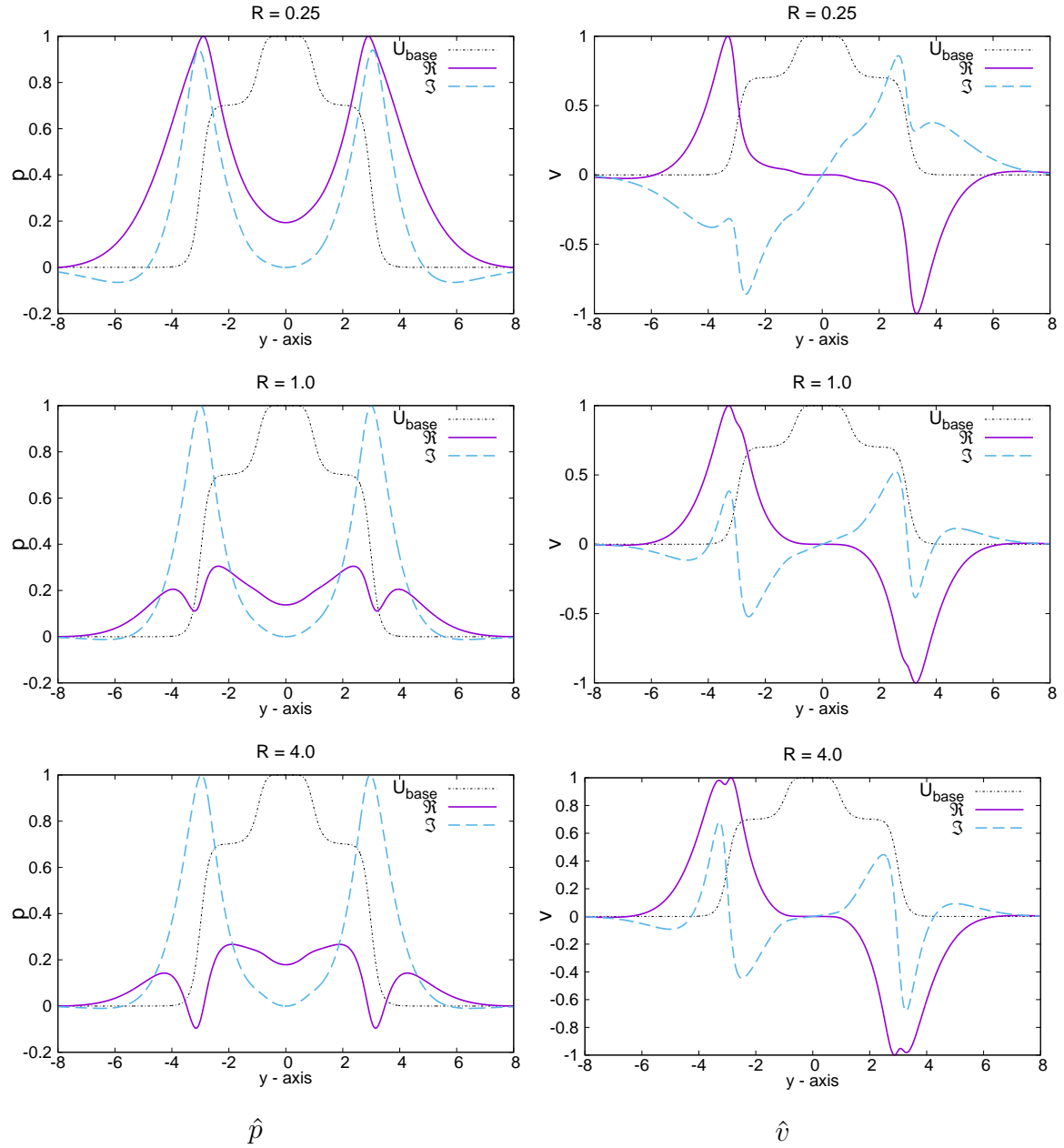


Figure 3.42, like the previous figure, presents three graphics for the pressure $\hat{p}(y)$ and normal velocity component $\hat{v}(y)$ eigenfunction. In this figure, maximum amplitude of \hat{p} and \hat{v} also serves to identify the internal modes of the problem. Dependence of \hat{p} and \hat{v} eigenfunction on gas ratio R_{ratio} variations, a radiant mode is observed for the gas ratio $R_{ratio} = 0.25$, similar to the sinuous case.

Figure 3.43 shows the streamwise velocity component eigenfunction $\hat{u}(y)$ for max-

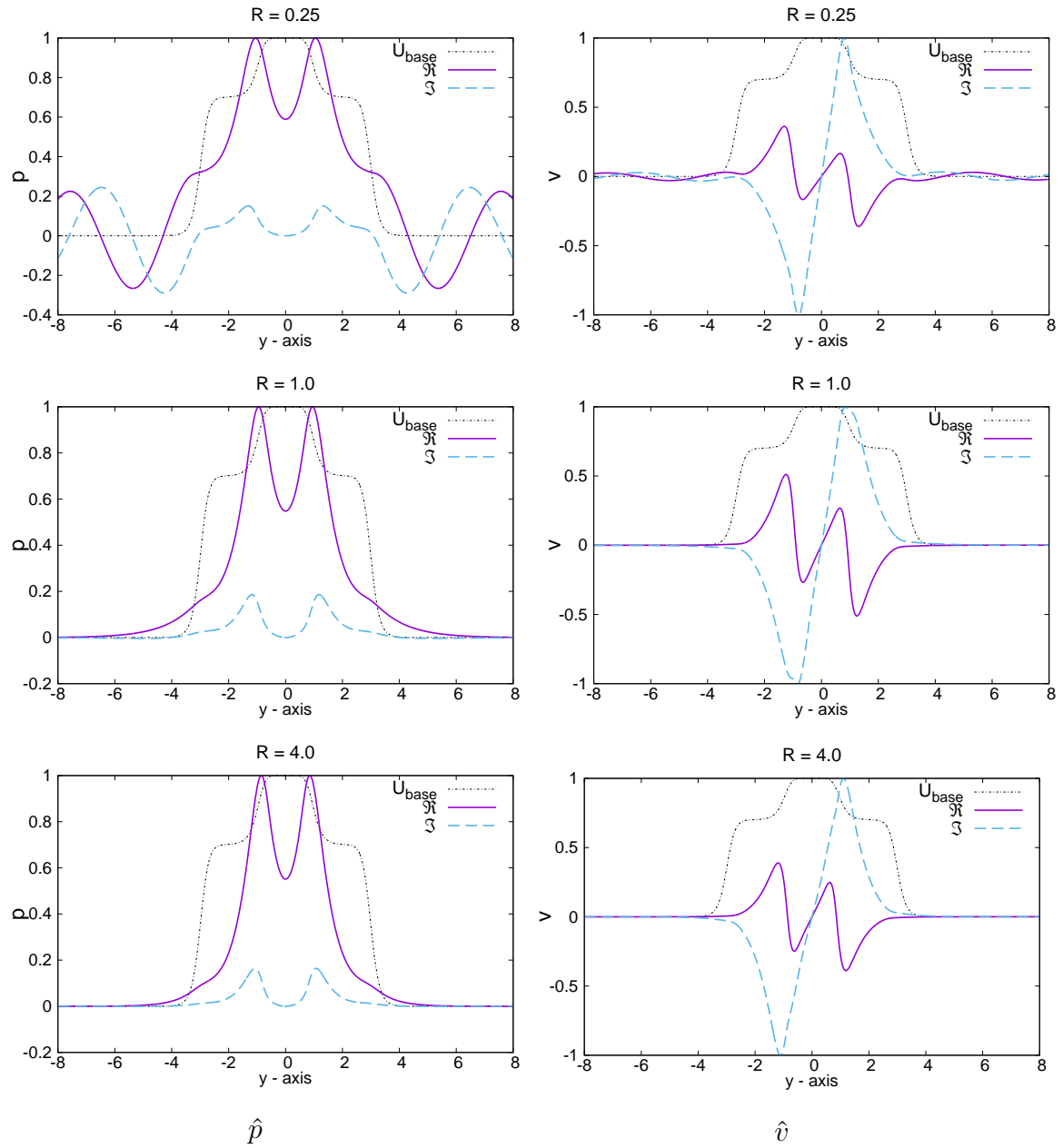
Figure 3.41 - Pressure $\hat{p}(y)$ and normal velocity component $\hat{v}(y)$ for the varicose mode with maximum spatial amplification rate α_i for different gas ratios R_{ratio} and Mach number = 0.9, external mode, co-planar jet configuration.



imum spatial amplification rate α_i considering three different gas ratios $R_{ratio} = 0.25, 1.0$ and 4.0 , for varicose external mode and co-planar jet configuration. External mode is identified by looking at the maximum amplitude of the eigenfunction \hat{u} . This eigenfunction is dependent on gas ratio R_{ratio} variations.

Figure 3.44 is similar to the previous one, shows the streamwise velocity component eigenfunction $\hat{u}(y)$ for maximum spatial amplification rate α_i considering three dif-

Figure 3.42 - Pressure $\hat{p}(y)$ and normal velocity component $\hat{v}(y)$ for the varicose mode with maximum spatial amplification rate α_i for different gas ratios R_{ratio} and Mach number = 0.9, internal mode, co-planar jet configuration.



ferent gas ratios $R_{\text{ratio}} = 0.25, 1.0$ and 4.0 , for varicose internal mode and co-planar jet configuration. Identification of internal mode is made by analyzing the position of at maximum amplitude of the eigenfunction \hat{u} .

3.1.2.2 Sinuous and varicose mode mixing

When both internal and external modes are simultaneously present in the co-planar jet, the flow topology may be analysed through the vorticity field as presented in the previous section for sinuous/sinuous and varicose/varicose combinations. Considering that the internal and external modes may be of different nature, internal sinuous and external varicose or internal varicose and external sinuous. These combinations of instability modes may result in different flow characteristics, that when introducing nonlinear mechanisms, may alter the interaction among shear layers and path to turbulence, however it would require further investigations and our code account for linear stability only.

In Figure 3.45, lines of constant vorticity for maximum spatial amplification rate α_i are shown, considering both internal and external modes, gas ratio $R_{\text{ratio}} = 0.25$ and Mach number $Ma = 0.90$. Positive values are displayed in continuous black lines and negative values are displayed in dashed lines. The range of vorticity levels vary from -3.0 to 3.0. In Figure 3.45, the top graphic shows the vorticity isolines for sinuous external mode and the bottom Figure shows the vorticity isolines for the varicose internal mode.

In Figure 3.46, lines of constant vorticity for maximum spatial amplification rate α_i are shown, considering both internal and external modes, gas ratio $R_{\text{ratio}} = 4.0$ and Mach number $Ma = 0.90$. In Figure 3.46, the top graphic shows the vorticity isolines for sinuous external mode and the bottom Figure shows the vorticity isolines for the varicose internal mode.

3.2 PSE

To investigate the spatial stability using parabolized stability equations configurations, solutions for the dispersion relation $D(R_{\text{ratio}}, Ma, \alpha, \omega) = 0$ are sought. Due to complications in the numerical code, not much could be done to extract a significant range of results, due to the fact the code is not finished, initially the variable $R_{\text{ratio}} = 1.0$ were fixed, that is, only one gas is considered. The real part of the eigenvalue α_r is the streamwise wave number and α_i is the streamwise spatial growth rate. Only sinuous mode were calculated $\hat{p}(0) = 0$.

Differently from LST results, here solution for the problem are presented punctually and do not vary as a function of angular frequency ω_r . Once angular frequency ω_r is fixed, its respective wavenumber α_r , growth rate α_i and phase speed cp are

calculated. Flow structure is given by the vorticity fields and eigenfunctions \hat{p} , \hat{v} and \hat{u} .

The vorticity field, like in the LST results, is given by

$$\eta = \frac{\partial u'}{\partial y} - \frac{\partial v'}{\partial x}.$$

3.2.1 Simple jet

In this section, analysis will demonstrate PSE results of spatial stability of a simple jet. Plane jet flow is the same as previously calculated in LST section and demonstrated in Figure 2.1.

Table 3.4 - Spatial growth rate α_i and corresponding angular frequency ω , wavenumber α_r and phase speed cp for the simple jet.

	R_{ratio}	ω	α_r	α_i	cp
Sinuous	1.000	0.4000	0.65654	0.50322	0.60925

In order to initiate the PSE calculations, initial eigenfunctions \hat{p} , \hat{v} and \hat{u} are needed. These initial conditions are provided by using Linear Stability Theory (LST) numerical code assuming sinuous mode with gas ratio $R_{ratio} = 1.0$, simple jet configuration with maximum velocity of Mach number = 0.9. These initial conditions are displayed in Figure 3.47. \hat{u} , \hat{v} and \hat{p} obtained from the LST. These results are applied to the first step in PSE calculation. As a complex amplitude, the eigenfunctions are shown in its respective real \Re and imaginary parts \Im .

After running the PSE code, utilizing LST initial conditions, the eigenfunctions \hat{u} , \hat{v} and \hat{p} for the sinuous mode with gas ratio $R_{ratio} = 1.0$ and Mach number = 0.9 for simple jet configuration is obtained. These results are displayed in Figure 3.48

The evolution of the wavenumber α_r and growth rate α_i from initial conditions marched downstream via PSE are demonstrated in Figure 3.49. It is important to highlight that the initial condition from LST is used, however LST formulation is developed for a compressible gas, while PSE formulation at its current state considers an incompressible gas. This fact can, partially, justify the difference between the initial conditions and calculated results downstream, α at $x = 0$ and $x = 60$. Figure 3.49 is coherent with the theory, which predicts bigger growth rates in the

incompressible case.

Figure 3.50 shows the vorticity isolines of sinuous mode, for $R_{ratio} = 1.0$ and $Ma = 0.9$. Positive values are shown in continuous black lines and negative values are shown in dashed lines, the vorticity range are from -3.0 to 3.0

Figure 3.43 - Streamwise velocity component $\hat{u}(y)$ for the varicose mode with maximum spatial amplification rate α_i for different gas ratios R_{ratio} and Mach number = 0.9, external mode, co-planar jet configuration.

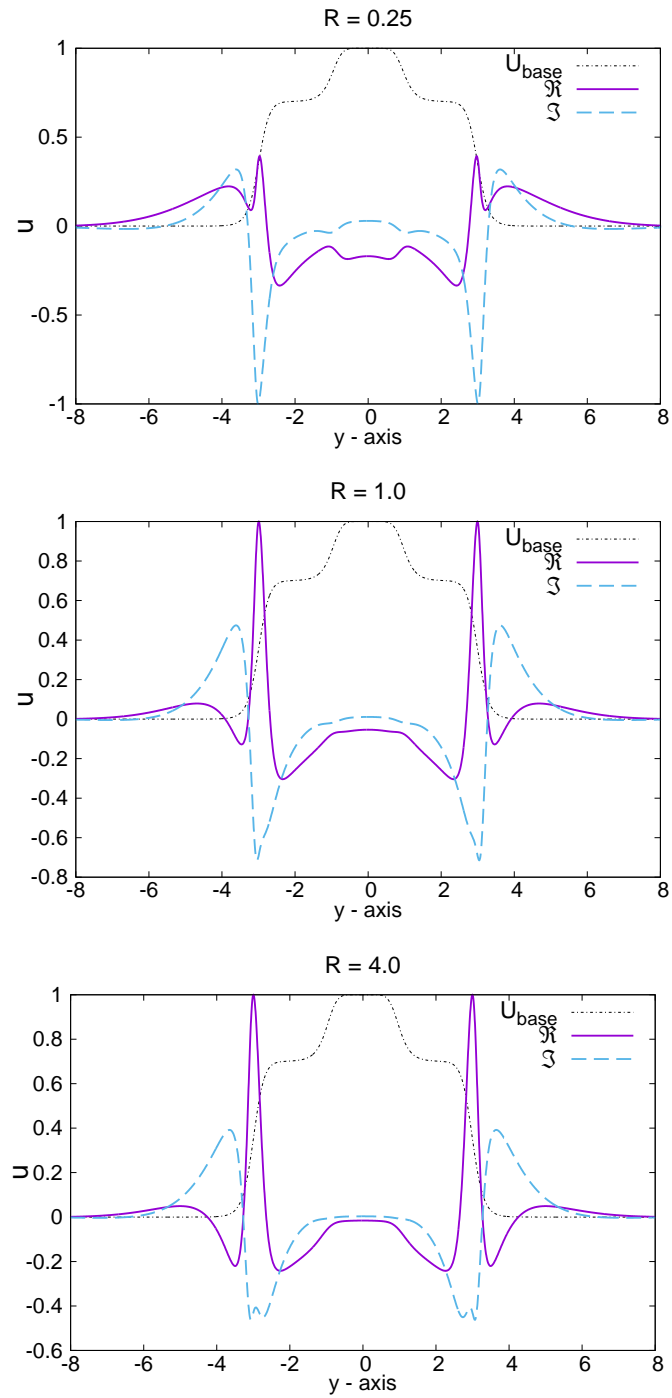


Figure 3.44 - Streamwise velocity component $\hat{u}(y)$ for the varicose mode with maximum spatial amplification rate α_i for different gas ratios R_{ratio} and Mach number = 0.9, internal mode, co-planar jet configuration.

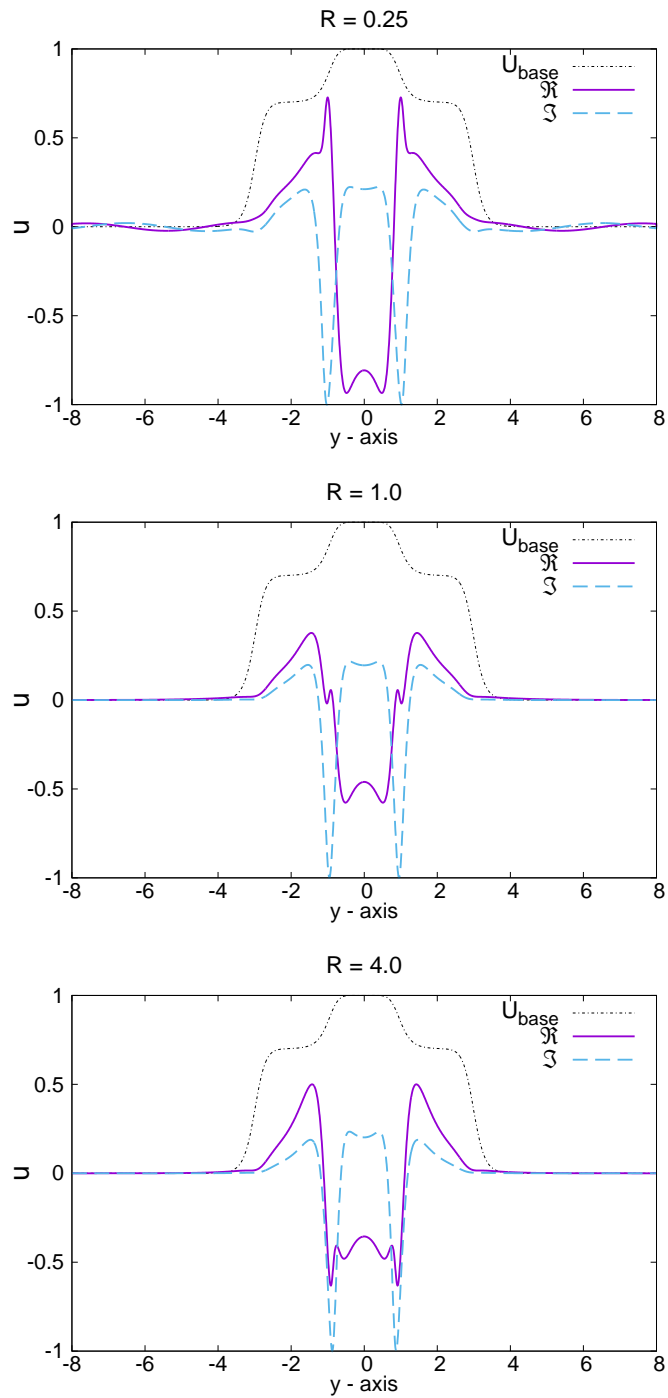
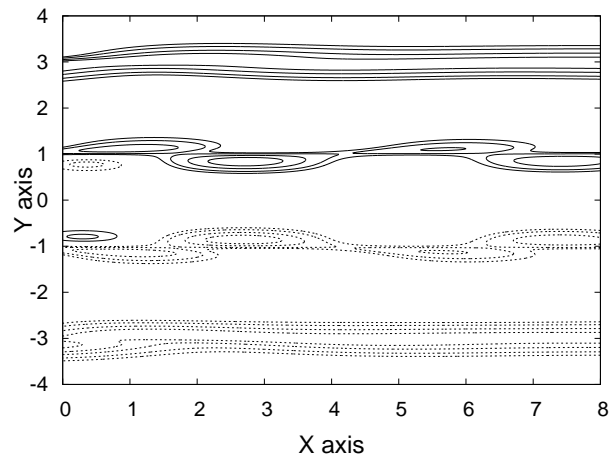
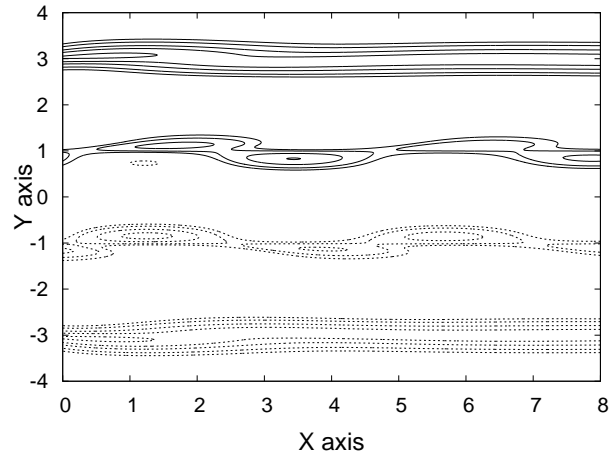


Figure 3.45 - Lines of constant vorticity disturbances. Maximum spatial amplification rate α_i is considered for both internal and external modes, $R_{\text{ratio}} = 0.25$ and $Ma = 0.90$. Positive values in continuous black lines, negative values in dashed lines. Range of vorticity levels from -3.0 to 3.0.

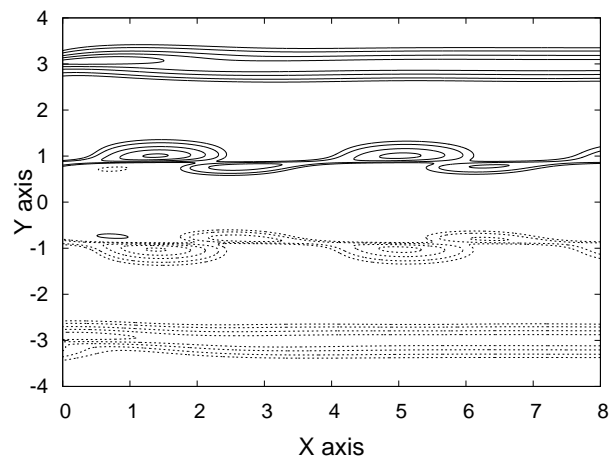


Sinusous external and varicose internal mode.

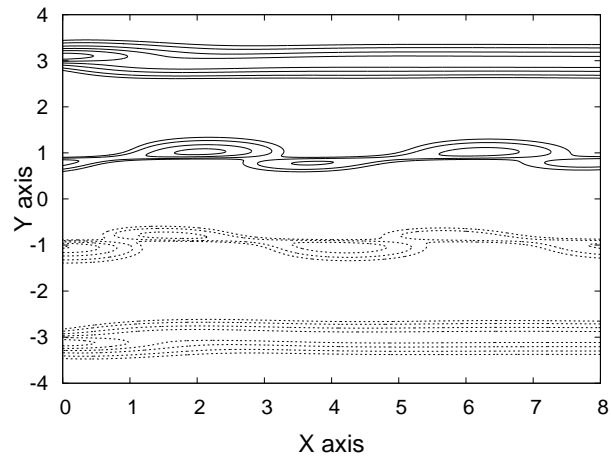


Varicose external and sinusous internal mode.

Figure 3.46 - Lines of constant vorticity disturbances. Maximum spatial amplification rate α_i is considered for both internal and external modes, $R_{\text{ratio}} = 4.0$ and $Ma = 0.90$. Positive values in continuous black lines, negative values in dashed lines. Range of vorticity levels from -3.0 to 3.0.



Sinusous external and varicose internal mode.



Varicose external and sinuous internal mode.

Figure 3.47 - LST Eigenfunctions \hat{u} , \hat{v} and \hat{p} for the sinuous mode with gas ratio $R_{ratio} = 1.0$ and Mach number = 0.9, simple jet configuration.

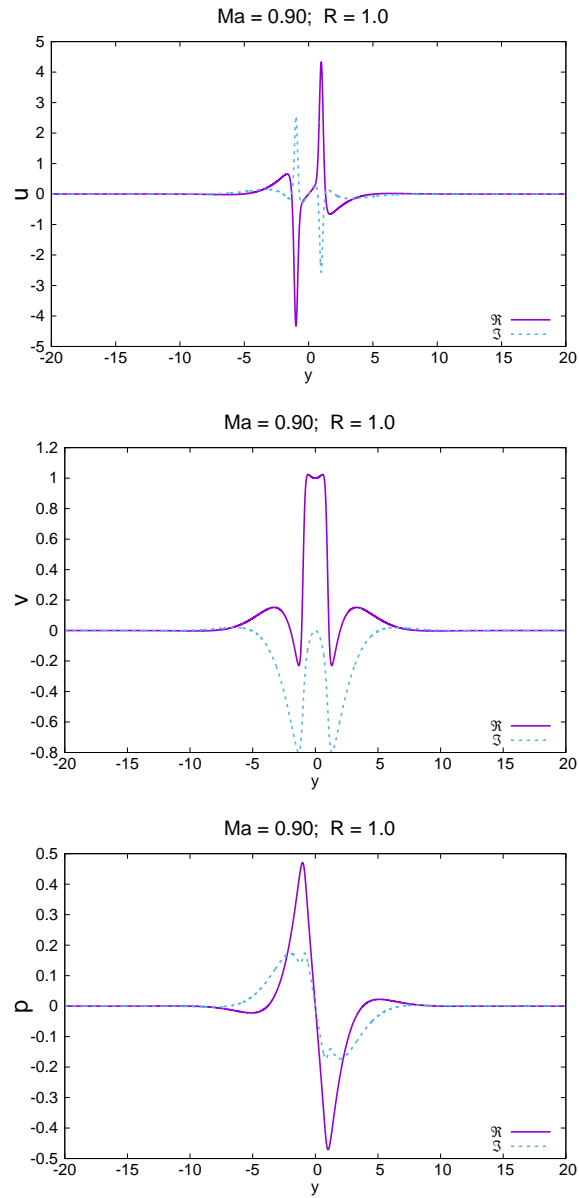


Figure 3.48 - PSE Eigenfunctions \hat{u} , \hat{v} and \hat{p} for the sinuous mode with gas ratio $R_{ratio} = 1.0$ and Mach number = 0.9, simple jet configuration.

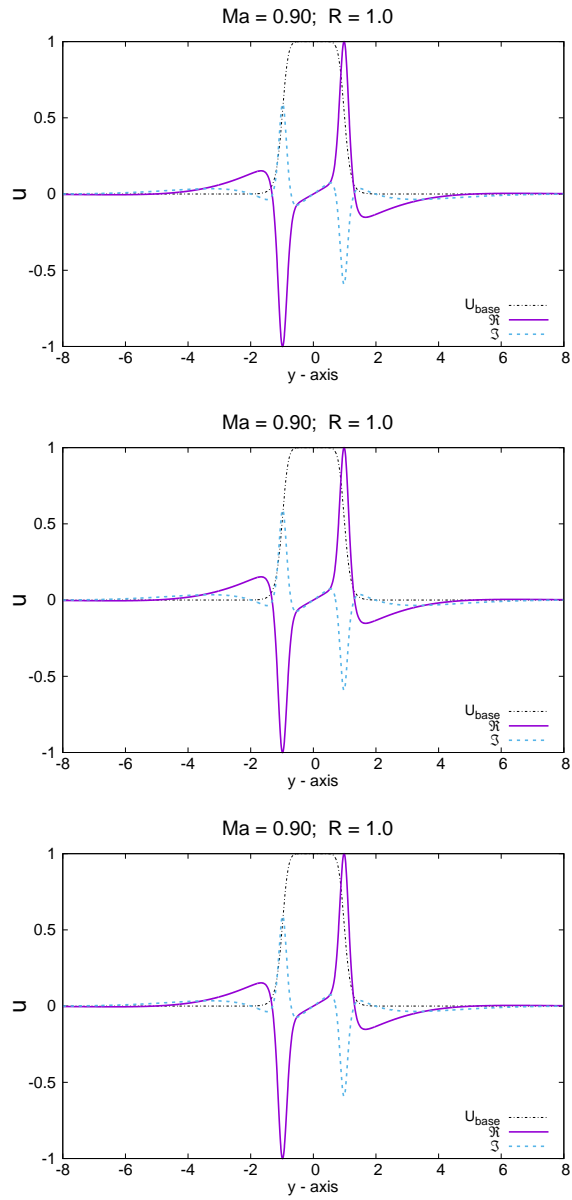


Figure 3.49 - Wavenumber α_r and growth rate α_i evolution for the sinuous mode with gas ratios $R_{ratio} = 1.0$ and Mach number = 0.9, simple jet configuration.

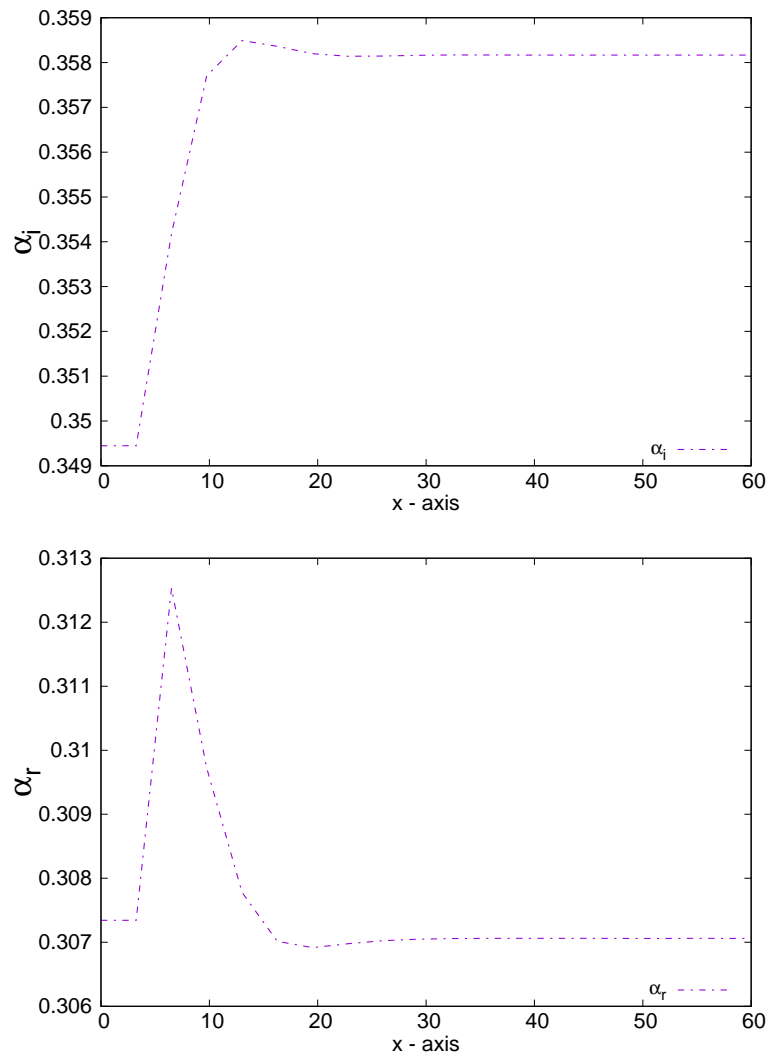
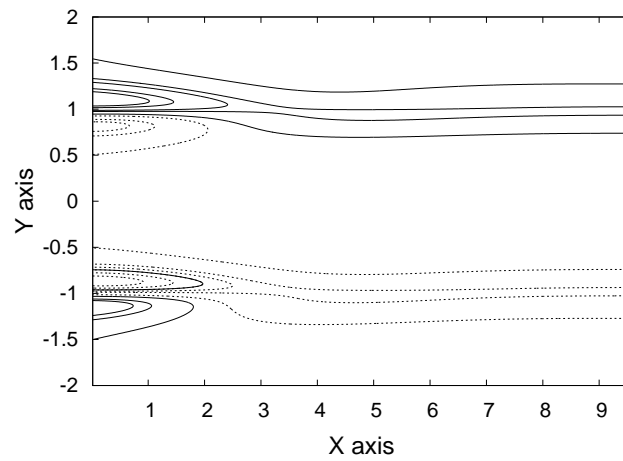


Figure 3.50 - Sinuous mode lines of constant vorticity for $R_{ratio} = 1.0$ and $Ma = 0.9$. Positive values in continuous black lines and negative values in dashed lines, vorticity range from -3.0 to 3.0



4 CONCLUSION

The first part of the present investigation addressed the issue of free shear layers composed of simple and co-flowing jets with different chemical species in the different streams. Different density ratios were considered and the effect of density ratio on the growth rate, range of unstable frequencies and disturbances phase speeds were studied. The resulting flow structures were also considered through the pressure disturbances. For the simple jet, density stratification has a stabilizing effect, but the varicose mode is more dispersive when the jet density is higher than the quiescent ambient. For the co-flowing jet configuration, four different instability modes were found, a sinuous and a varicose mode for the internal and external modes. The density stratification also has a stabilizing effect, except for the external mode, for which the growth rate increases monotonically with decreasing density ratio. The external mode, both for the varicose and sinuous modes, is more dispersive than the internal mode. The results for the co-flowing jet also show that the varicose and sinuous modes support radiating modes away from the jet. The range of density ratios considered and the results for co-flowing jets extend the information regarding the stability of binary free shear layers available in the literature. Considering the development of both inner and outer modes and the difference in phase speeds of each mode, the results indicate that in a nonlinear regime the interaction between the inner and outer modes may hasten transition to turbulence.

The second part addresses the PSE development for incompressible fluid flow with display of few results. Results obtained in this part are not enough to conduct any comparative stability analysis, focusing only in the sinuous mode of a simple planar jet, serving as basis for future works.

4.1 Future works

Future works, at the beginning, should focus on the development of the PSE numerical code, which is actually not fully developed. This development must prepare the code in order to include compressible flow, variable properties and non-stationary base flow. The extension of the present work should also consider non-parallel, non-linear model based on the parabolized stability equations (PSE) in order to access nonlinear effects. Further investigation on the characteristics of the radiating modes should be conducted. Another possible extension is the study on instability acoustic modes including the combustion process, for that the code should be modified in order to include chemical reaction, then analysis of flame stability could be conducted.

REFERENCES

BERTOLOTTI, F. **Linear and nonlinear stability of boundary layers with streamwise varying properties**. Tese (Doutorado) — Ohio State University, 1991. 3

BERTOLOTTI, F. P.; HERBERT, T. Analysis of the linear stability of compressible boundary layers using PSE. **Theoretical and Computational Fluid Dynamics**, v.3, p. 117–124, 1991. 11

BERTOLOTTI, F. P.; HERBERT, T.; SPALART, P. R. Linear and nonlinear stability of the Blasius boundary layers. **Journal of Fluid Mechanics**, v.242, p. 441–474, 1992. 12

CLAPEYRON, E. Mémoire sur la puissance motrice de la chaleur. **Journal de l'École Polytechnique**, v.14, 1834. 31

DATTA, A.; SINHAMAHAPATRA, K. P. Investigation of the influence of co-flow velocity ratio on a compressible plane jet exhausting into a parallel streams. **Aerospace Science and Technology**, v.45, p. 186–195, 2015. 8

_____. Investigation of the influence of convective mach number on compressible plane jet exhausting into parallel streams. **Journal of the Institution of Engineers (India): Series C**, v.99, p. 401–412, 2016. 8

DEO, R. C.; MI, J.; NATHAN, G. J. The influence of reynolds number on a plane jet. **Physics of Fluids**, v.20, p. 075108, 2008. 7

DEO, R. C.; NATHAN, G. J.; MI, J. Similarity analysis of the momentum field of a subsonic plane air jet with varying jet exit and local reynolds numbers. **Physics of Fluids**, v.25, p. 015115, 2013. 7

FEDIOUN, I.; LARDJANE, N. Temporal linear stability analysis of three-dimensional compressible binary shear layers. **AIAA Journal**, v.43, n. 1, p. 111–123, 2005. 9, 31

FREITAS, R. B.; FERNANDES, L. M.; MENDONÇA, M. T. Three-dimensional disturbances on binary mixing layers modified by jets and wakes. In: ABCM. **IUTAM SYMPOSIUM ON LAMINAR-TURBULENT TRANSITION**. Rio de Janeiro, Brazil, 2014. Accepted for presentation. 10

GASTER, M. On the generation of spatially growing waves in boundary layer. **Journal of Fluid Mechanics**, v. 22, p. 433–441, 1965. 3

GLOOR, M.; OBRIST, D.; KLEISER, L. Linear stability and acoustic characteristics of compressible, viscous, subsonic coaxial jet flow. **Physics of Fluids**, v. 25, n. 8, p. 084102, 2013. 12, 13

GROPENGIESSER, H. **Study on the stability of boundary layers and compressible fluids**. [S.l.: s.n.], 1970. 19

GROSCH, C. E.; SEINER, J. M.; HUSSAINI, M. Y.; JACKSON, T. L. Numerical simulation of mixing enhancement in a hot supersonic jet. **Physics of Fluids**, v.9, n. 4, p. 1125–1143, 1997. 6

GUTMARK, E.; C., K.; SCHADOW; WILSON, K. J. Effect of convective mach number on mixing of coaxial circular and rectangular jets. **Physics of Fluids A**, v.3, n. 1, p. 29–36, 1991. 5

HAAR, D. T. On the problem of turbulence. In: **Collected papers of L.D. Landau**. Pergamon, 1965. p. 387 – 391. ISBN 978-0-08-010586-4. Disponível em: <<http://www.sciencedirect.com/science/article/pii/B9780080105864500572>>. 3

HABLI, S.; SAID, N. M.; PALEC, G. L.; BOURNOT, H. Numerical study of a turbulent plane jet in a coflow environment. **Computers & Fluids**, v. 89, n. 5-6, p. 20–28, 2014. 7

HELMHOLTZ, H. On discontinuous movements of fluids. **Philosophical Magazine**, v. 36, p. 337–346, 1868. 1

HERBERT, T.; BERTOLOTTI, F. P. Stability analysis of nonparallel boundary-layers. **Bulletin of the American Physical Society**, v.32, p. 2079, 1987. 11

HIRSCHFELDER, J. O.; CURTISS, C. F.; BIRD., R. B. Molecular theory of gases and liquids. **Journal of Polymer Science**, v. 17, n. 83, p. 116–116, 1955. ISSN 1542-6238. 33

HSU, A. K.; PU, J. Y.; HU, S. S.; LIN, T. H. Flow field of an unconfined low-reynolds-number binary-mixture slot jet. **International Journal of Heat and Mass Transfer**, v.47, p. 1613–1625, 2004. 9

- JACKSON, T. L.; GROSCH, C. E. Inviscid spatial stability of a compressible mixing layers. **Journal of Fluid Mechanics.**, v.208, p. 609–637, 1989. 4
- _____. Absolute/convective instabilities and the convective mach number in a compressible mixing layer. **Physics of Fluids A**, v.2, n. 6, p. 949–954, 1990. 4
- KELVIN, W. The influence of wind on waves in water supposed frictionless. **Philosophical Magazine**, v. 42, p. 368–374, 1871. 1
- KENNEDY, C. A.; CHEN, M. Y. H. J. H.; JACKSON, T. L. Mean flow effects on the linear stability of compressible planar jets. **Physics of Fluids**, v.10, n. 3, p. 615–626, 1998. 6
- KENNEDY, C. A.; GATSKI, T. B. Selfsimilar supersonic variable density shear layers in binary systems. **Physics of Fluids A**, v.6, n. 2, p. 662–673, 1994. 8
- KOZUSKO, F.; GROSCH, C. E.; JACKSON, T. L.; KENNEDY, C. A.; GATSKI, T. B. The structure of a variable property, compressible mixing layer in binary gas mixtures. **Physics of Fluids**, v.8, n. 7, p. 1945–1953, 1996. 8, 31
- KOZUSKO, F.; LASSEIGNE, D. G.; GROSCH, C. E.; JACKSON, T. L. The stability of compressible mixing layers in binary gases. **Physics of Fluids**, v.8, n. 7, p. 1954–1963, 1996. 8
- LACERDA, J. F.; FRANCO, L. F. de; ROGENSKI, J. K.; MENDONÇA, M. T. Direct numerical simulation code validation for compressible shear flows using linear stability theory. **Journal of Aerospace Technology and Management**, v. 10, n. 184, p. 1–13, Sept. 2018. 11
- LEES, L.; LIN, C. C. Investigation of the stability of the laminar boundary layer in a compressible fluid. In: _____. **Selected papers of C C Lin with commentary**. [S.l.: s.n.], 1946. p. 69–70. 3
- MACK, L. M. Stability of the compressible laminar boundary layer according to a direct numerical solution. **AGARDograph 97**, Part I, p. 329–362, 1965. 3
- _____. Linear stability theory and the problem of supersonic boundary- layer transition. **AIAA Journal**, v. 13, n. 3, p. 278–289, 1975. Disponível em: <<https://arc.aiaa.org/doi/abs/10.2514/3.49693>>. 3
- MANCO, J. A. A.; FREITAS, R. B.; FERNANDES, L. M.; MENDONÇA, M. T. Stability of compressible mixing layers modified by wakes and jets. In: ABCM.

IUTAM SYMPOSIUM ON LAMINAR-TURBULENT TRANSITION.
Rio de Janeiro, Brazil, 2015. p. 129–136. 10, 11

MCBRIDE, B. J.; GORDON, S.; RENO, M. A. **Coefficients for calculating thermodynamic and transport properties of individual species.** [S.l.: s.n.], 1993. 32

MENDONÇA, M. T. **Numerical analysis of görtler vortices/Tollmien-Schlichting waves interaction with a spatial nonparallel model.** Tese (Doutorado) — The Pennsylvania State University, 1997. 38, 39

MENDONÇA, M. T. Linear stability analysis of binary compressible mixing layers modified by a jet or a wake deficit. In: AIAA. **AEROSPACE SCIENCES MEETING.** 2014. Disponível em:
<<https://arc.aiaa.org/doi/abs/10.2514/6.2014-1444>>. 9, 10, 11, 13

MICHALKE, A. Survey on jet instability theory. **Progress in Aerospace Sciences**, v.21, p. 159–199, 1984. 21

MILES, J. H. **Predicting the stability of a compressible periodic parallel jet flow.** [S.l.: s.n.], 1996. 5

NEUFELD, P. D.; JANZEN, A. R.; AZIZ, R. A. Empirical equations to calculate 16 of the transport collision integrals $g(i,8)^*$ for the lennard-jones (12-6) potential. **Journal of Chemical Physics**, v.57, n. 3, p. 1100–1102, 1972. 33

ORR, W. The stability or instability of the steady motions of a perfect liquid and of a viscous fluid. **Proceedings of the Royal Irish Academy**, v.27, p. 9–68, 1907. 2

POLING, B. E.; PRAUSNITZ, J. M.; O'CONNELL, J. P. **Properties of gases and liquids.** 5. ed. [S.l.]: McGraw-Hill Education, 2001. ISBN 9780070116825. 33

QUINTANILHA, H. R. A.; ALVES, L. S. B.; SOUZA, O. M. R.; MENDONÇA, M. T. A linear stability analysis of incompressible coaxial jets using an accurate boundary-layer approximation as base flow. In: ABCM. **INTERNATIONAL CONGRESS OF MECHANICAL ENGINEERING.** Rio de Janeiro, RJ, 2015. 7

RAYLEIGH, J. W. S. **The theory of sound.** 2. ed. New York: Dover, 1945. 1

- REICHERT, R. S.; BIRINGEN, S. Numerical simulation of compressible plane jets. **Mechanics Research Communications**, v.34, p. 249–259, 2007. 6, 7
- REID, R. C.; PRAUSNITZ, J. H.; SHERWOOD, T. K. **The properties of gases and liquids**. 3. ed. [S.l.]: McGraw-Hill Book Company, 1977. McGraw Hill Chemical Engineering Series. 34, 35
- ROGENSKI, J. K.; SOUZA, L. F.; MENDONÇA, M. T. de; MORRIS, P. J. Growth of even and odd instability modes in compressible binary jet flows. In: ABCM. **INTERNATIONAL CONGRESS OF MECHANICAL ENGINEERING**. Curitiba, PR, 2017. 10, 11
- SALEMI, L.; MENDONÇA, M. T. Spatial and temporal linear stability analysis of binary compressible shear layer. In: AIAA. **FLUID DYNAMICS CONFERENCE**. Seattle, USA, 2008. p. 1–23. 9, 11
- SALEMI, L. C. **Análise de estabilidade linear de camada de mistura compressível binária**. Dissertação (Mestrado em Combustão e Propulsão) — Instituto Nacional de Pesquisas Espaciais, São José dos Campos, 2006. 33, 34
- SANDHAM, N. D. **Investigation of the compressible mixing layer**. Tese (Doutorado) — Stanford University, USA, 1990. 20
- SCHLICHTING, H. **Zur entstehung der turbulenz bei der plattenströmung**. [S.l.]: Weidmann, 1933. (Sonderdrucke aus den Nachrichten von der Gesellschaft der Wissenschaften zu Göttingen : Mathematisch-physikalische Klasse). 2
- SCHUBAUER, G. B.; SKRAMSTAD, H. K. **Laminar boundary layer oscillations and transition on a flat plate**. [S.l.: s.n.], 1948. 2
- SCHUMAKER, S. A.; DRISCOLL, J. F. Mixing properties of coaxial jets with large velocity ratios and large inverse density ratios. **Physics of Fluids**, v.24, p. 055101, 2012. 10
- SHIH, C.; KROTHAPALLI, A.; GOGINENI, S. Experimental observation of instability modes in a rectangular jet. **AIAA Journal**, v.30, n. 10, p. 2388–2394, 1992. 5
- SHIN, D. S.; FREZIGER, J. H. Linear stability of the reacting mixing layer. **AIAA Journal**, v.29, n. 10, p. 1634–1642, 1991. 31

- SOMMERFELD, A. **Ein beitrag zur hydrodynamischen erklärung der turbulent fluessigkeitsbewegungen**. Rome: Accademia dei Lincei, 1908. 2
- STANLEY, S.; SARKAR, S. Simulation of spatially developing two-dimensional shear layers and jets. **Theoretical and Computational Fluid Dynamics**, v.9, p. 121–147, 1997. 6
- STUART, J. T. On the nonlinear-mechanics of wave disturbances in stable and unstable parallel flows. **Journal Fluid Mechanics**, v.9, n. 3, p. 353–370, 1960. 3
- SURESH, P. R.; SRINIVASAN, K.; SUNDARARAJAN, T.; DAS, S. K. Reynolds number dependence of plane jet development in the transitional regime. **Physics of Fluids**, v.20, p. 044105, 2008. 7
- SVEHLA, R. A. **Transport coefficients for the NASA Lewis chemical equilibrium program**. [S.l.: s.n.], 1995. 34
- TAM, C. K. W.; THIES, A. T. Instability of rectangular jets. **Journal of Fluid Mechanics**, v.248, p. 425–448, 1993. 5
- TEJA, A. S. Simple method for the calculation of heat capacities of liquid mixtures. **Journal of Chemical & Engineering Data**, v. 28, n. 1, p. 83–85, 1983. 33
- TOLLMIEN, W. Über die entstehung der turbulenz. 1. mitteilung. **Mathematisch Physikalischen Klasse**, p. S. 21–44, 1929. 2
- WATANABE, D.; MAEKAWA, H. Transition of supersonic plane jet due to symmetric/antisymmetric unstable modes. **Journal of Turbulence**, v.3, 2002. 6
- WATSON, J. On the nonlinear-mechanics of wave disturbances in stable and unstable parallel flows. **Journal of Fluid Mechanics**, v.9, n. 3, p. 353–370, 1960. 3
- WEDER, M. **Linear stability and acoustics of a subsonic plane jet flow**. Dissertação (Mestrado) — Institute of Fluid Dynamics, ETH Zurich, 2012. 7, 12, 21, 22, 41, 43, 47
- ZHUANG, M.; KUBOTA, T.; DIMOTAKIS, P. E. Instability of inviscid compressible free shear layers. **AIAA Journal**, v.28, n. 10, p. 1728–1733, 1990. 4

APPENDIX A - COMPLEMENTARY TERMS AND EQUATIONS

A.1 Non-dimensional equation of state

$$p^* = \rho^* R^* T^*. \quad (\text{A.1})$$

Non-dimensional parameters

$$p = \frac{p^*}{\rho_0^* u_0^{*2}}, \quad \rho = \frac{\rho^*}{\rho_0^*}, \quad R = \frac{R^*}{R_0^*}, \quad T = \frac{T^*}{T_0^*}. \quad (\text{A.2})$$

Substituting the parameters (A.2) into Equation (A.1)

$$\frac{p}{\rho_0^* u_0^{*2}} = \frac{\rho R T}{\rho_0^* R_0^* T_0^*}. \quad (\text{A.3})$$

Multiplying Equation (A.3) by γ/γ

$$p = \rho R T \frac{u_0^{*2}}{R_0^* T_0^*} \frac{\gamma}{\gamma}. \quad (\text{A.4})$$

The Mach number is defined as $Ma = u^*/\sqrt{\gamma R^* T^*}$, then $Ma^2 = u_0^{*2}/(\gamma R_0^* T_0^*)$. So Equation (A.4) become

$$p = \rho R T Ma^2 \gamma. \quad (\text{A.5})$$

A.2 Equations: linear stability analysis

Continuity equation

$$\frac{\partial \rho}{\partial t} + \frac{\partial \rho u}{\partial x} + \frac{\partial \rho v}{\partial y} + \frac{\partial \rho w}{\partial z} = 0. \quad (\text{A.6})$$

Streamwise momentum equation

$$\rho \frac{\partial u}{\partial t} + \rho u \frac{\partial u}{\partial x} + \rho v \frac{\partial u}{\partial y} + \rho w \frac{\partial u}{\partial z} = -\frac{1}{\gamma_1 Ma^2} \frac{\partial p}{\partial x}. \quad (\text{A.7})$$

Normal momentum equation

$$\rho \frac{\partial v}{\partial t} + \rho u \frac{\partial v}{\partial x} + \rho v \frac{\partial v}{\partial y} + \rho w \frac{\partial v}{\partial z} = -\frac{1}{\gamma_1 Ma^2} \frac{\partial p}{\partial y}. \quad (\text{A.8})$$

Spanwise momentum equation

$$\rho \frac{\partial w}{\partial t} + \rho u \frac{\partial w}{\partial x} + \rho v \frac{\partial w}{\partial y} + \rho w \frac{\partial w}{\partial z} = -\frac{1}{\gamma_1 Ma^2} \frac{\partial p}{\partial z}. \quad (\text{A.9})$$

Internal Energy equation, in terms of temperature

$$\rho \frac{\partial T}{\partial t} + \rho u \frac{\partial T}{\partial x} + \rho v \frac{\partial T}{\partial y} + \rho w \frac{\partial T}{\partial z} = -\frac{p(\gamma - 1)}{R} \left(\frac{\partial u}{\partial x} + \frac{\partial v}{\partial y} + \frac{\partial w}{\partial z} \right). \quad (\text{A.10})$$

Mass fraction equation

$$\rho \frac{\partial S_1}{\partial t} + \rho u \frac{\partial S_1}{\partial x} + \rho v \frac{\partial S_1}{\partial y} + \rho w \frac{\partial S_1}{\partial z} = 0. \quad (\text{A.11})$$

Equation of state for a perfect gas

$$p = \rho RT. \quad (\text{A.12})$$

Then the variables of Equations (A.6), (A.7), (A.8), (A.9), (A.10), (A.11) and (A.12) are divided in a mean value plus a perturbation, like Equation (A.13)

$$\phi(x, y, z, t) = \bar{\phi}(y) + \phi'(x, y, z, t), \quad (\text{A.13})$$

where

$$\bar{\phi}(y) = [\bar{\rho}(y), (\bar{U}(y), 0, 0), \bar{P} = 1, \bar{T}(y), \bar{S}_1(y), \bar{R}(y)]^T. \quad (\text{A.14})$$

$$\phi'(x, y, z, t) = [\rho', u', v', w', p', T', S'_1, R']^T. \quad (\text{A.15})$$

Then

Continuity equation

$$\begin{aligned} \frac{\partial}{\partial t}(\bar{\rho} + \rho') + \frac{\partial(\bar{u} + u')}{\partial x}(\bar{\rho} + \rho')(\bar{u} + u') + \frac{\partial(\bar{v} + v')}{\partial y}(\bar{\rho} + \rho')(\bar{v} + v') + \quad (\text{A.16}) \\ \frac{\partial(\bar{w} + w')}{\partial z}(\bar{\rho} + \rho')(\bar{w} + w') = 0. \end{aligned}$$

$$\begin{aligned} \frac{\partial(\bar{u} + u')}{\partial t}(\bar{\rho} + \rho') + \frac{\partial(\bar{u} + u')}{\partial x}(\bar{\rho} + \rho')(\bar{u} + u') + \quad (\text{A.17}) \\ \frac{\partial(\bar{u} + u')}{\partial y}(\bar{\rho} + \rho')(\bar{v} + v') + \frac{\partial(\bar{u} + u')}{\partial z}(\bar{\rho} + \rho')(\bar{w} + w') = -\frac{1}{\gamma_1 Ma^2} \frac{\partial(\bar{p} + p')}{\partial x}. \end{aligned}$$

$$\begin{aligned} \frac{\partial(\bar{v} + v')}{\partial t}(\bar{\rho} + \rho') + \frac{\partial(\bar{v} + v')}{\partial x}(\bar{\rho} + \rho')(\bar{u} + u') + \quad (\text{A.18}) \\ \frac{\partial(\bar{v} + v')}{\partial y}(\bar{\rho} + \rho')(\bar{v} + v') + \frac{\partial(\bar{v} + v')}{\partial z}(\bar{\rho} + \rho')(\bar{w} + w') = -\frac{1}{\gamma_1 Ma^2} \frac{\partial(\bar{p} + p')}{\partial y}. \end{aligned}$$

$$\begin{aligned} \frac{\partial(\bar{w} + w')}{\partial t}(\bar{\rho} + \rho') + \frac{\partial(\bar{w} + w')}{\partial x}(\bar{\rho} + \rho')(\bar{u} + u') + \quad (\text{A.19}) \\ \frac{\partial(\bar{w} + w')}{\partial y}(\bar{\rho} + \rho')(\bar{v} + v') + \frac{\partial(\bar{w} + w')}{\partial z}(\bar{\rho} + \rho')(\bar{w} + w') = -\frac{1}{\gamma_1 Ma^2} \frac{\partial(\bar{p} + p')}{\partial z}. \end{aligned}$$

$$\begin{aligned} (\bar{\rho} + \rho') \frac{\partial(\bar{T} + T')}{\partial t} + (\bar{\rho} + \rho')(\bar{u} + u') \frac{\partial(\bar{T} + T')}{\partial x} + \quad (\text{A.20}) \\ (\bar{\rho} + \rho')(\bar{v} + v') \frac{\partial(\bar{T} + T')}{\partial y} + (\bar{\rho} + \rho')(\bar{w} + w') \frac{\partial(\bar{T} + T')}{\partial z} = - \\ \frac{(\bar{p} + p')(\gamma - 1)}{R} \left(\frac{\partial(\bar{u} + u')}{\partial x} + \frac{\partial(\bar{v} + v')}{\partial y} + \frac{\partial(\bar{w} + w')}{\partial z} \right). \end{aligned}$$

$$\begin{aligned} (\bar{\rho} + \rho') \frac{\partial(\bar{S}_1 + S'_1)}{\partial t} + (\bar{\rho} + \rho')(\bar{u} + u') \frac{\partial(\bar{S}_1 + S'_1)}{\partial x} + \quad (\text{A.21}) \\ (\bar{\rho} + \rho')(\bar{v} + v') \frac{\partial(\bar{S}_1 + S'_1)}{\partial y} + (\bar{\rho} + \rho')(\bar{w} + w') \frac{\partial(\bar{S}_1 + S'_1)}{\partial z} = 0. \end{aligned}$$

$$\bar{p} + p' = \bar{\rho}R'T' + \rho'\bar{R}T' + \rho'R'\bar{T}. \quad (\text{A.22})$$

Subtracting the base equations from Equations (A.17), (A.18), (A.19), (A.20), (A.21), (A.22) and (A.22), then neglecting the non-linear terms:

Continuity equation

$$\frac{\partial \rho'}{\partial t} + \bar{U} \frac{\partial \rho'}{\partial x} + \bar{\rho} \frac{\partial u'}{\partial x} + \bar{\rho} \frac{\partial v'}{\partial y} + \bar{\rho} \frac{\partial w'}{\partial z} + v' \frac{\partial \bar{\rho}}{\partial y} = 0. \quad (\text{A.23})$$

Streamwise momentum equation

$$\bar{\rho} \frac{\partial u'}{\partial t} + \bar{\rho} \bar{U} \frac{\partial u'}{\partial x} + \bar{\rho} v' \frac{\partial \bar{U}}{\partial y} = -\frac{1}{\gamma_1 Ma^2} \frac{\partial p'}{\partial x}. \quad (\text{A.24})$$

Normal momentum equation

$$\bar{\rho} \frac{\partial v'}{\partial t} + \bar{\rho} \bar{U} \frac{\partial v'}{\partial x} = -\frac{1}{\gamma_1 Ma^2} \frac{\partial p'}{\partial y} + \rho' g. \quad (\text{A.25})$$

Spanwise momentum equation

$$\bar{\rho} \frac{\partial w'}{\partial t} + \bar{\rho} \bar{U} \frac{\partial w'}{\partial x} = -\frac{1}{\gamma_1 Ma^2} \frac{\partial p'}{\partial z}. \quad (\text{A.26})$$

Energy equation

$$\bar{\rho} \frac{\partial T'}{\partial t} + \bar{\rho} \bar{U} \frac{\partial T'}{\partial x} + \bar{\rho} v' \frac{\partial \bar{T}}{\partial y} = -\frac{(\gamma-1)}{R} \frac{\partial u'}{\partial x} - \frac{(\gamma-1)}{R} \frac{\partial v'}{\partial y} - \frac{(\gamma-1)}{R} \frac{\partial w'}{\partial z}. \quad (\text{A.27})$$

The energy equation may be further simplified multiplying the equation by R , assuming $R = \bar{R} + R'$ and keeping only the linear and parallel terms,

$$\bar{\rho} \frac{\partial T'}{\partial t} + \bar{\rho} \bar{U} \frac{\partial T'}{\partial x} + \bar{\rho} v' \frac{\partial \bar{T}}{\partial y} = -\frac{(\gamma-1)}{\bar{R}} \frac{\partial u'}{\partial x} - \frac{(\gamma-1)}{\bar{R}} \frac{\partial v'}{\partial y} - \frac{(\gamma-1)}{\bar{R}} \frac{\partial w'}{\partial z}. \quad (\text{A.28})$$

Mass fraction equation

$$\bar{\rho} \frac{\partial S'_1}{\partial t} + \bar{\rho} \bar{U} \frac{\partial S'_1}{\partial x} + \bar{\rho} v' \frac{\partial \bar{S}_1}{\partial y} = 0. \quad (\text{A.29})$$

Equation of state

$$p' = \bar{\rho} \bar{R} T' + \bar{\rho} R' \bar{T} + \rho' \bar{R} \bar{T}. \quad (\text{A.30})$$

Normal modes are applied

$$\phi'(x, y, z, t) = \mathcal{R} \left\{ \hat{\phi}(y) \exp[i(\alpha x + \beta z - \omega t)] \right\}, \quad (\text{A.31})$$

then

$$\frac{\partial \phi'}{\partial t} = -\hat{\phi} i \omega \exp[i(\alpha x + \beta z - \omega t)]. \quad (\text{A.32})$$

$$\frac{\partial \phi'}{\partial x} = \hat{\phi} i \alpha \exp[i(\alpha x + \beta z - \omega t)]. \quad (\text{A.33})$$

$$\frac{\partial \phi'}{\partial y} = \frac{\partial \hat{\phi}}{\partial y} \exp[i(\alpha x + \beta z - \omega t)]. \quad (\text{A.34})$$

$$\frac{\partial \phi'}{\partial z} = \hat{w} i \beta \exp[i(\alpha x + \beta z - \omega t)]. \quad (\text{A.35})$$

$$\phi' \frac{\partial \bar{\phi}}{\partial y} = \hat{\phi} \frac{\partial \bar{\phi}}{\partial y} \exp[i(\alpha x + \beta z - \omega t)]. \quad (\text{A.36})$$

Applying Equations (A.32), (A.33), (A.34), (A.35) and (A.36) into Equations (A.23), (A.24), (A.25), (A.26), (A.27), (A.28) and (A.29), after some manipulation, it is possible to rewrite the equations

Continuity equation

$$\hat{\rho} i (\alpha \bar{U} - \omega) + \hat{v} \frac{d\bar{\rho}}{dy} + \bar{\rho} \left[i (\alpha \hat{u} + \beta \hat{w}) + \frac{d\hat{v}}{dy} \right] = 0. \quad (\text{A.37})$$

Streamwise momentum equation

$$\hat{u}i(\alpha\bar{U} - \omega) + \hat{v}\frac{d\bar{U}}{dy} + \frac{i\alpha\hat{p}}{\bar{\rho}\gamma_1 Ma^2} = 0. \quad (\text{A.38})$$

Normal momentum equation

$$\hat{v}i(\alpha\bar{U} - \omega) + \frac{1}{\bar{\rho}\gamma_1 Ma^2} \frac{d\hat{p}}{dy} = 0. \quad (\text{A.39})$$

Spanwise momentum equation

$$\hat{w}i(\alpha\bar{U} - \omega) + \frac{i\beta\hat{p}}{\bar{\rho}\gamma_1 Ma^2} = 0. \quad (\text{A.40})$$

Energy equation

$$\hat{T}i(\alpha\bar{U} - \omega) + \hat{v}\frac{d\bar{T}}{dy} + \frac{(\gamma - 1)}{\bar{\rho}\bar{R}} \left[i(\alpha\hat{u} + \beta\hat{w}) + \frac{d\hat{v}}{dy} \right] = 0. \quad (\text{A.41})$$

Mass fraction

$$\hat{S}_1 i(\alpha\bar{U} - \omega) + \hat{v}\frac{d\bar{S}_1}{dy} = 0. \quad (\text{A.42})$$

A.3 Taylor's expansion of dependent variables

$$\phi'(T) = \frac{d\phi(\bar{T})}{dT} T' + O(T'^2). \quad (\text{A.43})$$

$$\phi'(T, S_n) = \frac{\partial\phi(\bar{T})}{\partial T} T' + \frac{\partial\phi(\bar{S}_n)}{\partial S_n} S'_n + O(T'^2) + O(S_n'^2). \quad (\text{A.44})$$

The derivative of the transport coefficients are given by the chain rule:

$$\frac{d\bar{\phi}}{dx} = \frac{d\bar{\phi}}{dT} \frac{dT}{dx}. \quad (\text{A.45})$$

$$\frac{\partial\bar{\phi}}{\partial x} = \frac{\partial\bar{\phi}}{\partial T} \frac{\partial T}{\partial x} + \frac{\partial\bar{\phi}}{\partial S_n} \frac{\partial S_n}{\partial x}. \quad (\text{A.46})$$

$$\frac{\partial \phi'}{\partial x} = \frac{\partial}{\partial x} \left[\frac{d\phi(\bar{T})}{dT} T' \right] = \frac{\partial^2 \bar{\phi}}{\partial T^2} T' \frac{\partial \bar{T}}{\partial x} + \frac{\partial \bar{\phi}}{\partial T} \frac{\partial T'}{\partial x}. \quad (\text{A.47})$$

$$\begin{aligned} \frac{\partial \phi'}{\partial x} &= \frac{\partial}{\partial x} \left[\frac{d\phi(\bar{T})}{dT} T' + \frac{d\phi(\bar{S}_n)}{dS_n} S'_n \right] = \\ &= \frac{\partial^2 \bar{\phi}}{\partial T^2} T' \frac{\partial \bar{T}}{\partial x} + \frac{\partial \bar{\phi}}{\partial T} \frac{\partial T'}{\partial x} + \frac{\partial^2 \bar{\phi}}{\partial S_n^2} S'_n \frac{\partial \bar{S}_n}{\partial x} + \frac{\partial \bar{\phi}}{\partial S_n} \frac{\partial S'_n}{\partial x}. \end{aligned} \quad (\text{A.48})$$

A.4 Partial derivatives of perturbations

Compressible Euler equations are presented

$$\frac{\partial \phi'}{\partial t} = -\hat{\phi} i \omega \chi. \quad (\text{A.49})$$

$$\frac{\partial \phi'}{\partial x} = \frac{\partial \hat{\phi}}{\partial x} \chi + \hat{\phi} a \chi. \quad (\text{A.50})$$

$$\frac{\partial \phi'}{\partial y} = \frac{\partial \hat{\phi}}{\partial y} \chi. \quad (\text{A.51})$$

$$\frac{\partial^2 \phi'}{\partial x^2} = 2a \frac{\partial \hat{\phi}}{\partial x} \chi + \hat{\phi} \frac{da}{dx} \chi + \hat{\phi} a^2 \chi. \quad (\text{A.52})$$

$$\frac{\partial^2 \phi'}{\partial y^2} = \frac{\partial^2 \hat{\phi}}{\partial x^2} \chi. \quad (\text{A.53})$$

$$\frac{\partial \phi'}{\partial xy} = \frac{\partial}{\partial x} \left(\frac{\partial \hat{\phi}}{\partial y} \right) \chi = \frac{\partial^2 \hat{\phi}}{\partial xy} \chi + a \frac{\partial \hat{\phi}}{\partial y} \chi. \quad (\text{A.54})$$

$$\frac{\partial \phi'}{\partial yx} = \frac{\partial}{\partial x} \left(\frac{\partial \hat{\phi}}{\partial x} \chi + \hat{\phi} a \chi \right) = \frac{\partial^2 \hat{\phi}}{\partial yx} \chi + \frac{\partial \hat{\phi}}{\partial y} a \chi + \underbrace{\hat{\phi} \frac{da}{dy}}_{=0} \chi. \quad (\text{A.55})$$

A.5 PSE equations

Mass balance

$$\frac{\partial \hat{u}}{\partial x} \chi + \hat{u} a \chi + \frac{\partial \hat{v}}{\partial y} \chi = 0. \quad (\text{A.56})$$

Momentum in x coordinate

$$\begin{aligned} & -\bar{\rho} \hat{u} i \omega \chi + \bar{\rho} \bar{u} \left(\frac{\partial \hat{u}}{\partial x} + \hat{u} a \right) \chi + \bar{\rho} \hat{u} \frac{\partial \bar{u}}{\partial x} \chi + \bar{\rho} \bar{v} \frac{\partial \hat{u}}{\partial y} \chi + \bar{\rho} \hat{v} \frac{\partial \bar{u}}{\partial y} \chi = \\ & - \left(\frac{\partial \hat{p}}{\partial x} \chi + \hat{p} a \right) \chi - \frac{2\bar{\mu}}{3Re} \left(2a \frac{\partial \hat{u}}{\partial x} \chi + \hat{u} \frac{da}{dx} \chi + \hat{u} a^2 \chi + \frac{\partial^2 \hat{v}}{\partial xy} \chi + a \frac{\partial \hat{v}}{\partial y} \chi \right) \\ & + \frac{2\bar{\mu}}{Re} \left(2a \frac{\partial \hat{u}}{\partial x} \chi + \hat{u} \frac{da}{dx} \chi + \hat{u} a^2 \chi \right) + \frac{\bar{\mu}}{Re} \left(\frac{\partial^2 \hat{u}}{\partial yx} \chi + \frac{\partial \hat{v}}{\partial y} a \chi + \frac{\partial^2 \hat{u}}{\partial y^2} \chi \right). \end{aligned} \quad (\text{A.57})$$

Equation (A.57) can be simplified to

$$\begin{aligned} & -\bar{\rho} \hat{u} i \omega \chi + \bar{\rho} \bar{u} \left(\frac{\partial \hat{u}}{\partial x} + \hat{u} a \right) \chi + \bar{\rho} \hat{u} \frac{\partial \bar{u}}{\partial x} \chi + \bar{\rho} \bar{v} \frac{\partial \hat{u}}{\partial y} \chi + \bar{\rho} \hat{v} \frac{\partial \bar{u}}{\partial y} \chi = \\ & - \left(\frac{\partial \hat{p}}{\partial x} \chi + \hat{p} a \right) \chi - \frac{2\bar{\mu}}{3Re} \left(\frac{\partial^2 \hat{v}}{\partial xy} \chi \right) + \frac{1}{3} \frac{\bar{\mu}}{Re} \frac{\partial \hat{v}}{\partial y} a \chi \\ & + \frac{4\bar{\mu}}{3Re} \left(2a \frac{\partial \hat{u}}{\partial x} \chi + \hat{u} \frac{da}{dx} \chi + \hat{u} a^2 \chi \right) + \frac{\bar{\mu}}{Re} \left(\frac{\partial^2 \hat{u}}{\partial yx} \chi + \frac{\partial^2 \hat{u}}{\partial y^2} \chi \right). \end{aligned} \quad (\text{A.58})$$

Momentum in y coordinate

$$\begin{aligned} & -\bar{\rho} \hat{v} i \omega \chi + \bar{\rho} \bar{u} \left(\frac{\partial \hat{v}}{\partial x} \chi + \hat{v} a \chi \right) + \bar{\rho} \hat{u} \frac{\partial \bar{v}}{\partial x} + \bar{\rho} \bar{v} \frac{\partial \hat{v}}{\partial y} \chi + \bar{\rho} \hat{v} \frac{\partial \bar{v}}{\partial y} = \\ & - \frac{\partial \hat{p}}{\partial y} \chi - \frac{2\bar{\mu}}{3Re} \left(\frac{\partial^2 \hat{u}}{\partial yx} \chi + \frac{\partial \hat{u}}{\partial y} a \chi + \frac{\partial^2 \hat{v}}{\partial y^2} \chi \right) + \frac{2\bar{\mu}}{Re} \frac{\partial^2 \hat{v}}{\partial y^2} \chi \\ & + \frac{\bar{\mu}}{Re} \left(2a \frac{\partial \hat{v}}{\partial x} \chi + \hat{v} \frac{da}{dx} \chi + \hat{v} a^2 \chi + \frac{\partial^2 \hat{u}}{\partial xy} \chi + a \frac{\partial \hat{u}}{\partial y} \chi \right). \end{aligned} \quad (\text{A.59})$$

Equation (A.59) can be simplified to

$$\begin{aligned}
& -\bar{\rho}\hat{v}i\omega\chi + \bar{\rho}\bar{u}\left(\frac{\partial\hat{v}}{\partial x}\chi + \hat{v}a\chi\right) + \bar{\rho}\hat{u}\frac{\partial\bar{v}}{\partial x} + \bar{\rho}\bar{v}\frac{\partial\hat{v}}{\partial y}\chi + \bar{\rho}\hat{v}\frac{\partial\bar{v}}{\partial y} = \\
& -\frac{\partial\hat{p}}{\partial y}\chi - \frac{2\bar{\mu}}{3Re}\frac{\partial^2\hat{u}}{\partial yx}\chi + \frac{4\bar{\mu}}{3Re}\frac{\partial^2\hat{v}}{\partial y^2}\chi + \frac{1}{3}\frac{\bar{\mu}}{Re}\frac{\partial\hat{u}}{\partial y}a\chi \\
& + \frac{\bar{\mu}}{Re}\left(2a\frac{\partial\hat{v}}{\partial x}\chi + \hat{v}\frac{da}{dx}\chi + \hat{v}a^2\chi + \frac{\partial^2\hat{u}}{\partial xy}\chi\right).
\end{aligned} \tag{A.60}$$

Energy balance

$$\begin{aligned}
& -\bar{\rho}\bar{c}_p\hat{T}i\omega\chi + \hat{p}i\omega\chi + \bar{\rho}\bar{c}_p\hat{u}\frac{\partial\bar{T}}{\partial x}\chi \\
& + \bar{\rho}\bar{c}_p\bar{u}\left(\frac{\partial\hat{T}}{\partial x}\chi + \hat{T}a\chi\right) + \hat{v}\frac{\partial}{\partial y}(\bar{T}\bar{\rho}\bar{c}_p)\chi + \bar{\rho}\bar{c}_p\bar{v}\frac{\partial\hat{T}}{\partial y}\chi = \\
& + Ec\left[\hat{u}\frac{\partial\bar{p}}{\partial x}\chi + \bar{u}\left(\frac{\partial\hat{p}}{\partial x}\chi + \hat{p}a\chi\right) + \hat{v}\frac{\partial\bar{p}}{\partial y}\chi + \bar{v}\frac{\partial\hat{p}}{\partial y}\chi - \hat{p}\left(\frac{\partial\bar{u}}{\partial x} + \frac{\partial\bar{v}}{\partial y}\right)\chi\right. \\
& \quad \left.- \bar{p}\left(\frac{\partial\hat{u}}{\partial x}\chi + \hat{u}a\chi + \frac{\partial\hat{v}}{\partial y}\chi\right)\right] \\
& + \frac{\bar{k}}{PrRe}\left[2a\frac{\partial\hat{T}}{\partial x}\chi + \hat{T}\frac{da}{dx}\chi + \hat{T}a^2\chi + \frac{\partial^2\hat{T}}{\partial y^2}\chi\right] \\
& - \frac{2Ec}{3Re}\left[2\bar{\mu}\left(\frac{\partial\hat{u}}{\partial x}\chi + \hat{u}a\chi\right)\frac{\partial\bar{u}}{\partial x} + 2\bar{\mu}\frac{\partial\hat{v}}{\partial y}\frac{\partial\bar{v}}{\partial y}\chi\right] \\
& - \frac{4Ec}{3Re}\left\{\bar{\mu}\left[\frac{\partial\bar{u}}{\partial x}\frac{\partial\hat{v}}{\partial y}\chi + \frac{\partial\bar{v}}{\partial y}\left(\frac{\partial\hat{u}}{\partial x}\chi + \hat{u}a\chi\right)\right]\right\} \\
& - \frac{Ec}{Re}\left[2\bar{\mu}\frac{\partial\hat{u}}{\partial y}\frac{\partial\bar{u}}{\partial y}\chi + 2\bar{\mu}\left(\frac{\partial\hat{v}}{\partial x}\chi + \hat{v}a\chi\right)\frac{\partial\bar{v}}{\partial x}\right].
\end{aligned} \tag{A.61}$$

Species balance

$$\begin{aligned}
& -\hat{S}_ni\omega\chi + \bar{\rho}\bar{u}\left(\frac{\partial\hat{S}_n}{\partial x}\chi + \hat{S}_na\chi\right) + \bar{\rho}\hat{u}\frac{\partial\bar{S}_n}{\partial x}\chi + \bar{\rho}\bar{v}\frac{\partial\hat{S}_n}{\partial y}\chi + \bar{\rho}\hat{v}\frac{\partial\bar{S}_n}{\partial y}\chi = \\
& \frac{1}{ReSc}\left[\bar{\rho}\bar{D}\left(\frac{\partial\hat{S}_n}{\partial x}\chi + \hat{S}_na\chi\right) + \bar{\rho}\bar{D}\frac{\partial\hat{S}_n}{\partial y}\chi\right].
\end{aligned} \tag{A.62}$$

A.6 Elements of the matrices

Here the matrices of Equation (2.104) are presented

$$A_1 = \frac{1}{12\Delta y}. \quad (\text{A.63})$$

$$B_1 = -\frac{2}{3\Delta y}. \quad (\text{A.64})$$

$$C_1 = 0. \quad (\text{A.65})$$

$$D_1 = \frac{2}{3\Delta y}. \quad (\text{A.66})$$

$$E_1 = -\frac{1}{12\Delta y}. \quad (\text{A.67})$$

$$R_1 = \frac{1}{12\Delta y}. \quad (\text{A.68})$$

$$A_2 = \frac{\bar{\rho}_j^i \bar{v}_j^i}{12\Delta y} + \frac{\bar{\mu}_j^i}{12\text{Re}(\Delta y)^2} - \frac{\bar{\mu}_j^i}{8\text{Re}\Delta x \Delta y}. \quad (\text{A.69})$$

$$B_2 = -\frac{2\bar{\rho}_j^i \bar{v}_j^i}{3\Delta y} - \frac{4\bar{\mu}_j^i}{3\text{Re}(\Delta y)^2} + \frac{\bar{\mu}_j^i}{\text{Re}\Delta x \Delta y}. \quad (\text{A.70})$$

$$C_2 = \bar{\rho}_j^i \omega i + \bar{\rho}_j^i u_j^i \left(\frac{3}{2\Delta x} + a^i \right) + \bar{\rho}_j^i \bar{U}_x \quad (\text{A.71})$$

$$- \frac{4\bar{\mu}_j^i}{3\text{Re}} \left(\frac{3a^i}{2\Delta x} + (a^i)^2 + \frac{a^i - a^{i-1}}{\Delta x} \right) + \frac{\bar{\mu}_j^i}{\text{Re}} \left(\frac{10}{4(\Delta y)^2} \right).$$

$$D_2 = -\frac{2\bar{\rho}_j^i \bar{v}_j^i}{3\Delta y} - \frac{4\bar{\mu}_j^i}{3\text{Re}(\Delta y)^2} - \frac{\bar{\mu}_j^i}{\text{Re}\Delta x \Delta y}. \quad (\text{A.72})$$

$$E_2 = -\frac{\bar{\rho}_j^i v_j^i}{12\Delta y} + \frac{\bar{\mu}_j^i}{12Re(\Delta y)^2} + \frac{\bar{\mu}_j^i}{8Re\Delta x\Delta y}. \quad (\text{A.73})$$

$$\begin{aligned} R_2 - \bar{\rho}_j^i \bar{u}_j^i & \left(\frac{-4i_j^i + u_j^{i-1}}{2\Delta x} \right) - \bar{\rho}_j^i v_j^i \bar{U}_y - \frac{p_j^i - p_j^{i-1}}{\Delta x} - p_j^i a^i \\ & - \frac{2\bar{\mu}_j^i}{3Re} \frac{a^i}{12\Delta y} \left[(v_{j-2}^i - 8v_{j-1}^i + 8v_{j+1}^i - v_{j+2}^i) \right. \\ & \quad \left. - (v_{j-2}^{i-1} - 8v_{j-1}^{i-1} + 8v_{j+1}^{i-1} - v_{j+2}^{i-1}) \right] \\ & + \frac{\bar{\mu}_j^i}{3Re} \frac{a^i}{12\Delta y} (v_{j-2}^i - 8v_{j-1}^i + 8v_{j+1}^i - v_{j+2}^i) + \\ & \frac{\bar{\mu}_j^i}{18Re\Delta x\Delta y} \left[-4u_{j-2}^i + u_{j-2}^i - 8(-4u_{j-2}^i + u_{j-2}^i) + \right. \\ & \quad \left. 8(-4u_{j-2}^i + u_{j-2}^i) + 4u_{j-2}^i - u_{j-2}^i \right]. \end{aligned} \quad (\text{A.74})$$

$$A_3 = \frac{1}{12\Delta y}. \quad (\text{A.75})$$

$$B_3 = -\frac{2}{3\Delta y}. \quad (\text{A.76})$$

$$C_3 = 0. \quad (\text{A.77})$$

$$D_3 = \frac{2}{3\Delta y}. \quad (\text{A.78})$$

$$E_3 = -\frac{1}{12\Delta y}. \quad (\text{A.79})$$

$$\begin{aligned}
R_3 = & \bar{\rho}_j^i v_j^i \omega_i - \bar{\rho} u_j^i \left(\frac{v_j^i - v^{i-1}}{\Delta x} + v_j^i a^i \right) - \bar{\rho}_j^i u_j^i \bar{V}_x \\
& - \frac{\bar{\rho}_j^i \bar{v}_j^i}{12\Delta y} (v_{j-2}^i - 8v_{j-1}^i + 8v_{j+1}^i - v_{j+2}^i) - \bar{\rho}_j^i v_j^i \bar{V}_y \\
& - \frac{\bar{\mu}}{18Re\Delta y\Delta x} \left[u_{j-2}^i - u_{j-2}^{i-1} - 8(u_{j-1}^i - u_{j-1}^{i-1}) + \right. \\
& \quad \left. 8(u_{j+1}^i - u_{j+1}^{i-1}) - u_{j+2}^i + u_{j+2}^{i-1} \right] \\
& + \frac{\bar{\mu}_j^i}{9(\Delta y)^2} (-v_{j-2}^i + 16v_{j-1}^i - 30v_j^i + 16v_{j+1}^i - v_{j+2}^i) \\
& \quad + \frac{\bar{\mu}_j^i a^i}{36\Delta y} (u_{j-2}^i - 8u_{j-1}^i + 8u_{j+1}^i - u_{j+2}^i) \\
& + \frac{\bar{\mu}_j^i}{Re} \left\{ 2a^i \left(\frac{v_j^i - v_j^{i-1}}{\Delta x} \right) + v_j^i \left(\frac{a^i - a^{i-1}}{\Delta x} \right) + v_j^i (a^i)^2 \right. \\
& \quad + \frac{1}{12\Delta x\Delta y} (u_{j-2}^i - 8u_{j-1}^i + 8u_{j+1}^i - u_{j+2}^i) - \\
& \quad \left. (u_{j-2}^{i-1} - 8u_{j-1}^{i-1} + 8u_{j+1}^{i-1} - u_{j+2}^{i-1}) \right\}.
\end{aligned} \tag{A.80}$$

$$A_4 = \frac{\bar{\rho}_j^i \bar{c}_{p_j}^i \bar{v}_j^i}{12\Delta y} + \frac{\bar{k}_j^i}{12PrRe(\Delta y)^2}. \tag{A.81}$$

$$B_4 = -\frac{2\bar{\rho}_j^i \bar{c}_{p_j}^i \bar{v}_j^i}{3\Delta y} - \frac{4\bar{k}_j^i}{3PrRe(\Delta y)^2}. \tag{A.82}$$

$$\begin{aligned}
C_4 = & -\bar{\rho}_j^i \bar{c}_{p_j}^i \omega_i - \bar{\rho}_j^i \bar{c}_{p_j}^i \bar{u}_j^i \left(\frac{3}{2\Delta x} + a^i \right) \\
& - \frac{\bar{k}_j^i}{PrRe} \left[\frac{3a^i}{2\Delta x} + \frac{a^i - a^{i-1}}{\Delta x} + (a^i)^2 - \frac{30}{12\Delta y} \right].
\end{aligned} \tag{A.83}$$

$$D_4 = \frac{2\bar{\rho}_j^i \bar{c}_{p_j}^i \bar{v}_j^i}{3\Delta y} - \frac{4\bar{k}_j^i}{3PrRe(\Delta y)^2}. \tag{A.84}$$

$$E_4 = -\frac{\bar{\rho}_j^i \bar{c}_{p_j}^i \bar{v}_j^i}{12\Delta y} + \frac{\bar{k}_j^i}{12PrRe(\Delta y)^2}. \tag{A.85}$$

$$\begin{aligned}
R_4 = & -p_j^i \omega_i - \bar{\rho}_j^i c_{p_j}^i u_j^i \bar{T}_x - \bar{\rho}_j^i c_{p_j}^i \bar{u}_j^i \left(\frac{-4T_j^i + T_j^{i-1}}{2\Delta x} \right) - \bar{\rho}_j^i c_{p_j}^i v_j^i \bar{T}_y \quad (\text{A.86}) \\
-Ec \left[& u_j^i \bar{p}_x + \bar{u}_j^i \left(\frac{p^i - p^{i-1}}{\Delta x} + p_j^i a^i \right) + \frac{\bar{v}_j^i}{12\Delta y} (p_{j-2}^i - 8p_{j-1}^i + 8p_{j+1}^i - p_{j+2}^i) \right. \\
& \left. - p_j^i (\bar{U}_x + \bar{V}_y) - \bar{p}_j^i \left(\frac{u_j^i - u_j^{i-1}}{\Delta x} + u_j^i a^i + \frac{v_{j-2}^i - 8v_{j-1}^i + 8v_{j+1}^i - v_{j+2}^i}{12\Delta y} \right) \right] \\
& + \frac{\bar{k}_j^i}{PrRe} \left[a^i \left(\frac{-4T_j^i + T_j^{i-1}}{\Delta x} \right) \right] - \frac{4Ec}{3Re} \left[\bar{\mu}_j^i \bar{U}_x \left(\frac{u_j^i - u^{i-1}}{\Delta x} + u_j^i a^i \right) + \right. \\
& \left. \bar{\mu}_j^i \bar{V}_y \frac{v_{j-2}^i - 8v_{j-1}^i + 8v_{j+1}^i - v_{j+2}^i}{12\Delta y} \right] \\
& - \frac{4Ec}{3Re} \left[\bar{\mu}_j^i \bar{U}_x \frac{v_{j-2}^i - 8v_{j-1}^i + 8v_{j+1}^i - v_{j+2}^i}{12\Delta y} + \bar{\mu}_j^i \bar{V}_y \left(\frac{u_j^i - u^{i-1}}{\Delta x} + u_j^i a^i \right) \right] \\
& - \frac{2Ec}{Re} \left[\bar{\mu}_j^i \bar{U}_y \frac{u_{j-2}^i - 8u_{j-1}^i + 8u_{j+1}^i - u_{j+2}^i}{12\Delta y} + \bar{\mu}_j^i \bar{V}_x \left(\frac{v_j^i - v^{i-1}}{\Delta x} + v_j^i a^i \right) \right].
\end{aligned}$$

$$A_5 = \frac{\bar{\rho}_j^i \bar{v}_j^i}{12\Delta y} - \frac{\bar{\rho}_j^i \bar{D}_j^i}{12ReSc\Delta y}. \quad (\text{A.87})$$

$$B_5 = -\frac{8\bar{\rho}_j^i \bar{v}_j^i}{12\Delta y} + \frac{8\bar{\rho}_j^i \bar{D}_j^i}{12ReSc\Delta y}. \quad (\text{A.88})$$

$$C_5 = -\bar{\rho}_j^i \omega_i + \bar{\rho}_j^i \bar{u}_j^i \left(\frac{3}{2\Delta x} + a^i \right) - \frac{\bar{\rho}_j^i \bar{D}_j^i}{ReSc} \left(\frac{3}{2\Delta x} + a^i \right). \quad (\text{A.89})$$

$$D_5 = \frac{8\bar{\rho}_j^i \bar{v}_j^i}{12\Delta y} - \frac{8\bar{\rho}_j^i \bar{D}_j^i}{12ReSc\Delta y}. \quad (\text{A.90})$$

$$E_5 = -\frac{\bar{\rho}_j^i \bar{v}_j^i}{12\Delta y} + \frac{\bar{\rho}_j^i \bar{D}_j^i}{12ReSc\Delta y}. \quad (\text{A.91})$$

$$\begin{aligned}
& \bar{\rho}_j^i \bar{v}_j^i \left(\frac{-4S_{nj}^i + S_{nj}^{i-1}}{2\Delta x} \right) - \bar{\rho}_j^i \bar{u}_j^i \overline{(S_n)_x} - \bar{\rho}_j^i \bar{v}_j^i \overline{(S_n)_y} \\
& + \frac{\bar{\rho}_j^i \bar{D}_j^i}{ReSc} \left(\frac{-4S_{nj}^i + S_{nj}^{i-1}}{2\Delta x} \right).
\end{aligned} \tag{A.92}$$